

Local Aspects of the Bose Glass

Phase transitions of the disordered Bose-Hubbard model

Dissertation

zur Erlangung des Grades
der Doktorin der Naturwissenschaften

der Naturwissenschaftlichen-Technischen Fakultät II
- Physik und Mechatronik -
der Universität des Saarlandes

von

Astrid Elisa Niederle

Saarbrücken
2015

Tag des Kolloquiums: 18.05.2016
Dekan: Univ.-Prof. Dr. Georg Frey
Mitglieder des Prüfungsausschusses: Univ.-Prof. Dr. Karin Jacobs
Univ.-Prof. Dr. Heiko Rieger
Univ.-Prof. Dr. Giovanna Morigi
Dr. Reza Shaebani

Abstract

Bosons in optical lattices can be described by the Bose-Hubbard model. In regular lattices a phase transition from a Mott insulator to the superfluid phase occurs, at which localization is transferred from position to momentum space. In the disordered Bose-Hubbard model, where at least one parameter is a random variable, also the Bose glass phase occurs [1]. Interpreting this phase as a mixture of Mott insulator and superfluid sites leads to an innovative criterion for the phase transitions, called the local mean-field cluster analysis, excellently agreeing with quantum Monte-Carlo results [2].

In experiments disorder can be realized by a quasi-periodic potential, a superposition of a strong lattice and a second one with incommensurate wave length [3]. By introducing this potential in the derivation of the ordered Bose-Hubbard model, the Wannier functions are generalized by allowing them to be asymmetric, showing that not only disorder in the depth of the lattice sites, but also in the tunneling rates contributes crucially to the phase diagram of quasi-periodic potentials [4].

Moreover, the interplay of an optical lattice and a cavity field of photons, leads to a dynamical on-site potential for the bosons, which can be described within the Bose-Hubbard model [5, 6]. In the parameter regime accessible in experiments [7, 8], this system shows the Mott insulator, superfluid and the Bose glass phase as well as the supersolid phase characterized by a checker board pattern in the density profile [9].

Kurzzusammenfassung

Bosonen in optischen Gittern können durch das Bose-Hubbard Modell beschrieben werden. In regulären Gittern findet ein Phasenübergang vom Mott Isolator zur superfluiden Phase statt, bei dem die Lokalisation aus dem Ortsraum in den Impulsraum übergeht. Beim ungeordneten Bose-Hubbard Modell, in dem mindestens einer der Parameter eine Zufallsvariable ist, tritt zusätzlich die Bose Glass Phase auf [1]. Interpretiert man die Bose Glass Phase als Mischung von Mott Isolator and superfluiden Gitterplätzen, erhält man im Rahmen der sog. lokalen mean-field Cluster Analyse ein neues Kriterium für die Phasenübergänge, welches exzellent mit Quanten Monte-Carlo Ergebnissen übereinstimmt [2].

Experimentell kann Unordnung durch ein quasiperiodisches Potential realisiert werden, indem ein Hauptgitter mit einem zweiten mit inkommensurabler Wellenlänge überlagert wird [3]. Verwendet man dieses bei der Herleitung des Bose-Hubbard Modells, ergeben sich unsymmetrische, verallgemeinerte Wannier Funktionen und es zeigt sich, dass nicht nur Unordnung in der Gitterplatztiefe, sondern auch in den Tunnelraten entscheidend zum Phasendiagramm beiträgt [4].

Das Wechselspiel eines optischen Gitters mit dem Feld eines optischen Resonators, führt zu einem dynamischen lokalen Potential, welches innerhalb des Bose-Hubbard Modells beschrieben werden kann [5, 6]. Im experimentell zugänglichen Parameterregime [7, 8], treten hier die Mott Isolator, superfluide, Bose Glass Phase sowie die supersolide Phase auf, die durch ein Schachbrettmuster im Dichteprofil ausgezeichnet ist [9].

Contents

1	Introduction	1
2	Bose-Einstein condensates and optical lattices	7
2.1	Ultracold bosons	7
2.1.1	Bose-Einstein condensate	8
2.1.2	Superfluid	10
2.1.3	Bose-Einstein condensate and Superfluid	12
2.1.4	Bose gas in optical lattices	13
2.1.5	Experimental observation of the phase transitions	15
2.2	The Bose-Hubbard model	19
2.2.1	Wannier Functions	21
2.2.2	Derivation	23
2.2.3	Phase diagrams	24
2.2.3.1	The ordered Bose-Hubbard model	24
2.2.3.2	The disordered Bose-Hubbard model	26
2.2.4	Numerical Methods	27
3	Local and Stochastic mean-field theory	31
3.1	Local mean-field theory	31
3.2	Stochastic mean-field theory	33
3.3	Comparison	35
3.3.1	Superfluid order parameter and compressibility	36
3.3.2	Correlations of the local superfluid parameter	37
3.3.3	Probability distribution of the local superfluid parameter	40
4	Local mean-field cluster analysis	43
4.1	Percolation	43
4.2	Criteria for the phase transitions	46
4.3	Phase diagrams	52
4.3.1	Commensurate filling	52
4.3.2	Fixed disorder strength	54
5	Boxed uncorrelated disorder	59
5.1	Disorder in the on-site energy ϵ	59
5.2	Disorder in the tunneling rate J	60
5.3	Disorder in the inter-particle interaction U	63

6 Quasi-periodic bi-chromatic potentials	67
6.1 Bi-chromatic potentials	67
6.1.1 Generalized Wannier functions	68
6.1.2 Distributions of the Bose-Hubbard Parameters	69
6.2 Phase diagrams	72
6.2.1 Intensity phase diagram	72
6.2.2 Bose Hubbard parameter phase diagram	74
6.2.2.1 Commensurate filling	74
6.2.2.2 Fixed disorder strength	76
6.3 Comparison with alternative approaches	79
6.3.1 Quasi-periodic potential for the Bose-Hubbard parameters	79
6.3.2 Application of symmetric Wannier functions	81
7 Quasi-periodic structures due to cavity backaction	85
7.1 The System	85
7.2 The Bose-Hubbard model with long-range photon-mediated interactions	87
7.3 Commensurate lattices	90
7.3.1 Odd ratios (l odd)	92
7.3.2 Even ratios (l even)	94
7.4 Incommensurate lattices	96
7.4.1 Phase diagram for $\lambda = \lambda_0 + \epsilon_\lambda$	98
7.4.2 Phase diagram for $\lambda = \lambda_0/2 + \epsilon_\lambda$	101
7.4.3 Phase diagram for $\lambda = \lambda_0/3 + \epsilon_\lambda$	103
8 Conclusion	107
Appendix	111
A Mean-field description	111
A.1 Glauber coherent states	111
A.2 Gross-Pitaevskii equation	113
A.3 Superfluid order parameter	115
B Two site Bose-Hubbard system	117
C Monte-Carlo algorithm	119
C.1 Classical Monte-Carlo algorithm	119
C.2 Quantum Monte-Carlo algorithm	121
References	125
Figure Credit	133
Curriculum Vitae	135
Publications	137

Acknowledgment	141
-----------------------	------------

1 Introduction

Bosons confined in an optical lattice at ultracold temperatures serve as an ideal quantum system for the comparison of theoretical and experimental results on various quantum effects. On the one hand bosons in such a setup can be described precisely in theory within the Bose-Hubbard (BH) model [10], on the other hand in experiments the corresponding system parameters can be controlled with a high precision by tuning the intensity and the wave lengths of the lasers forming optical lattices in various dimensions and geometries [11–13]. By varying these laser parameters and the angle between the beams a variety of lattice configurations can be realized [14–18]. The theoretical parameters of the BH model and the experimental relevant parameters are linked uniquely, which allows for the direct and easy comparison of theoretical and experiment results in this field.

Within the so-called ordered BH model ultracold bosons confined in a periodic lattice can be described by three different energy scales: The on-site energy ϵ describing the depth of the lattice sites, the inter-particle interaction U , which represents the cost of energy for two particles occupying the same site, and the tunneling rate J , which is a rate for the hopping of particles between neighboring sites. A main feature of this system is that it shows a phase transition from the Mott insulator (MI) to the superfluid (SF) phase. In the MI phase, which occurs in the regime of small tunneling rates J , the ground state is neither coherent nor compressible. Moreover, there exist an energy gap in the particle excitation spectrum, preventing bosons from tunneling from one site to the other. Therefore, in the MI phase we find the same number of particles at each site, which means that the ground state in this phase is localized in position space. In the limit of large tunneling rates J the ground state is SF, which means that the particles are free to tunnel from site to site. In this situation the energy gap in the particle excitation spectrum is closed, the system is coherent and compressible and the ground state is localized in momentum space. Thus, at the MI-SF phase transition the localization in position space changes to a localization in momentum space.

The ordered BH system can be extended by the introduction of disorder in theory. This is mainly done by choosing the local on-site energies ϵ_i at each site randomly according to a bounded box distribution. In this case the so-called Bose glass (BG) phase occurs between the MI and the SF phase [19, 20]. On the one hand the ground state in the BG phase is compressible, like in the SF phase, but not yet coherent, as in the MI phase [1]. Thus, this phase exhibits features of the MI as well as of the SF phase. A deeper understanding of the characteristics of the BG phase is part of this thesis. The interpretation of the BG phase as a mixture of clusters of so-called MI and SF sites in Chapter 4 will lead to an innovative criterion for the phase transitions, called the local mean-field (LMF) cluster analysis.

The existence of the MI, SF as well as the BG phase has also been shown experimentally,

by making use of diverse features of the three phases in order to distinguish between them. The coherence of the quantum state in the optical lattice can be measured with help of the time-of-flight technique [21]. For this procedure the optical lattice is switched off after the experiment such that the atomic cloud can evolve freely. Under the assumption that the particles do not interact with each other during this process, which can be ensured at very low densities and after sufficiently long time, the density distribution in position space, which is accessible by absorption imaging, is proportional to the density distribution in momentum space of the cloud held in the optical lattice [22]. With the help of the Bragg spectroscopy, where particle tunneling is amplified in a controlled way, the particle excitation spectrum can be measured in the ordered as well as in the disordered case [3, 21, 23, 24]. By measuring the radius of the atomic cloud under a compression, achieved with the help of an additional harmonic trap, the compressibility is directly accessible in experiments [25].

The MI-SF transition occurring in the ordered system has been shown experimentally using ultracold ^{87}Rb atoms confined in a 3D optical lattice [21]. In order to distinguish between both phases they used time-of-flight imaging for the measurement of the appearance or absence of coherence in the quantum state. Moreover, the usage of Bragg spectroscopy confirmed the occurrence of the MI-SF transition by the observation of the disappearance of the gap in the excitation spectrum at the transition.

The existence of the BG phase in a disordered system, however, has been shown experimentally with time-of-flight imaging and Bragg spectroscopy on ultracold ^{87}Rb atoms in a 1D optical lattice [3]. In this experiment the disorder was introduced by a quasi-periodic potential constructed by a strong main periodic optical lattice, on which a second weaker optical lattice, with an incommensurate wave length, is superposed [3]. For a sufficiently small detuning between both wave lengths the periodicity exceeds the system size and the resulting quasi-periodic pattern may serve as an analogon for a disordered system. The theoretical description of such quasi-periodic optical potentials within the BH model and their comparison to the experiments will be discussed in Chapter 6. The second possibility for the realization of disorder is to use a speckle potential, randomly modulating the intensity of the laser and thus leading to local inhomogeneities in the lattice structure [26, 27]. While in a quasi-periodic potential the strength of the disorder and the distribution of the local values can be changed easily by varying the wave lengths and the intensities of both lasers, they are fixed in a speckle potential.

Theoretically, the disordered BH system is usually treated by isolated on-site box disorder, while the other parameters have precise values. Numerical methods like quantum Monte Carlo methods in various dimensions [20, 28–36] and density-matrix renormalization group techniques in one dimension [37–41] have been applied to this system in order to study the phase diagram. Based on the so-called LMF approximation [42] various numerical techniques have already been proposed, such as LMF theory [43–45], stochastic mean-field (SMF) theory [46, 47], which will be discussed thoroughly in Chapter 3. On that basis the LMF cluster analysis [2] will be introduced in Chapter 4 yielding a criterion for the phase transitions. As we will see, the phase diagram of the 2D disordered BH model with random on-site potentials predicted by the LMF cluster analysis [2] is in excellent agreement with the one calculated with quantum Monte Carlo methods [20].

Moreover, analytical perturbative results for the border of the MI region are available for the ordered [48] as well as for the disordered case [49].

The influence of disorder on the other BH parameters like the tunneling rates or the inter-particle interactions has rarely been studied. Disordered tunneling rates are mostly discussed in context with bimodal distributions [32, 47, 50, 51], where two different values of the tunneling rates are distributed randomly over the lattice. Compared to the experimental setups the modeling of tunneling disorder by a bimodal distribution is far from reality. Moreover, it is hardly comparable to a uniform distribution of the tunneling rates, where values are allowed to vary continuously in a certain range [4]. Disorder in the inter-particle interaction can be realized near a Feshbach resonance [52, 53] and a uniform distribution of this parameter has been studied in [4, 52, 54].

Having introduced the most important experimental and theoretical background in **Chapter 2**, the starting point of this thesis presented in **Chapter 3** is the LMF approximation [42]. Within this treatment the whole quantum system consisting of M sites and N particles can be decomposed into M individual quantum systems one for each site, which are coupled via an effective mean-field tunneling rate. By the introduction of the so-called local SF parameter $\psi_i = \langle \Psi | \hat{a}_i | \Psi \rangle$ the determination of the ground state $|\Psi\rangle$ of the whole quantum system is reduced to solving the determination equation for the local SF parameter recursively at each site. In the context of LMF theory this method has been used in order to determine the phase diagram of the disordered BH model on the basis of averaged values, which have been intended to serve as order parameters [43–45]. While this method works well in the ordered case, in the disordered case these averaged values do not show a kink in the vicinity of the expected phase transition. Therefore, in the framework of LMF approximation averaged global order parameters fail to indicate the phase transitions [2].

However, the LMF cluster analysis [2], introduced in **Chapter 4**, is able to determine the phase transitions of the disordered BH model on the basis of local properties of the system. With the help of the local particle numbers, which are calculated in the framework of the LMF approximation, so-called MI sites, with integer particle numbers and SF sites with non-integer particle numbers can be defined. On that basis a new criterion for the determination of the phase transitions can be implemented [2]: The MI phase, which appears for small tunneling rates, is characterized by a system consisting only of MI sites. At each site there is a fixed number of particles and particle fluctuations are suppressed. The quantum state is neither coherent nor compressible. The appearance of SF sites with non-integer particle numbers marks the transition to the BG phase. Here the system consists of a mixture of MI sites and connected SF regions. Since within these SF clusters particle fluctuations are possible, the whole atomic cloud is compressible, but phase coherence is not yet established in the whole system. With increasing tunneling rates the number of SF sites increases and finally at least one SF cluster percolates, which marks the entrance to the SF phase. The appearance of a percolating SF cluster, which dominates the behavior of the system, introduces long range order and global phase coherence. We will see that the phase diagram resulting from this LMF cluster analysis is in excellent agreement with quantum Monte Carlo predictions [2, 35].

With this new criterion for the phase transitions at hand, in **Chapter 5** the disorder

scenarios for each BH parameter are studied individually, while the remaining parameters are treated as sharp values. For each system there are characteristic differences in the phase diagram [4]: In the case of on-site disorder there exists an infinite number of MI regions, which are completely surrounded by the BG and finally, for large tunneling rate, by the SF phase. For disordered tunneling rate the number of MI regions is finite. In contrast to the previous case there exist individual BG regions and regions, where the SF phase reaches down to the limit of vanishing tunneling rates. In the situation with disordered inter-particle interaction there also exists a finite number of MI regions, which correspondingly to the case of disordered on-site energies, are surrounded by one BG and finally by one single SF region. In the limit of vanishing tunneling rates and vanishing chemical potential there exists a tricritical point, where all three phases approach each other tightly [4, 52, 54].

The knowledge of the characteristic influences of the different disorder scenarios, is the basis for the study of authentic disorder realizations as they are applied in experiments. In **Chapter 6** the quasi-periodic optical potential is studied, which is one of the available realizations of disorder in experiment. By introducing this potential in the usual derivation of the ordered BH model, its influence on the BH parameters can be derived fundamentally. This process requires a generalization of Wannier functions by allowing them to be asymmetric due to the asymmetry of the underlying quasi-periodic potential. Since these generalized Wannier functions have to be computed for each site individually, the numerical effort increases by a factor of the number of sites M in comparison to previous works, where the effect of quasi-periodic potential on the BH parameters was treated only approximately [37, 38, 55–57]. In contrast to the common expectation, disorder in the on-site energies as well as in the tunneling rates are important for the description of quasi-periodic potentials [4]. Both parameters reach the regime in which all three phases occur in the phase diagram. Indeed, due to the disordered tunneling rates the phase diagrams of the quasi-periodic potential deviate from those of isolated on-site disorder, which have mostly been studied in theory. Therefore, for a detailed comparison of theoretical and experimental results the influence of disordered tunneling rates has to be taken into account. Moreover, with a quasi-periodic potential as used in experiments real isolated on-site disorder, which mainly is studied in theory, cannot be realized.

The interplay of a periodic optical lattice and the optical field produced by photons, which are scattered coherently into a cavity, leads to a dynamical potential for bosonic atoms, which will be discussed in **Chapter 7**. In dependence of the system parameters there exist regions where the scattering of photons is prohibited and the atoms only feel the periodic optical lattice, while there are also other regions where effective scattering is favored. This system can be described by a BH model with a specific dynamical on-site potential from the cavity photons [5, 6]. In the parameter regime which is accessible in experiments [8], this system shows the MI, SF as well as the BG phase depending on the wave lengths of the optical lattice and the cavity field [9]. If they are commensurate the phase diagram consists of MI as well as SF regions, but also of supersolid (SS) regions, where only every second site is occupied, corresponding to a checker board pattern in the density profile. For incommensurate wave lengths the BG phase occurs in the parameter region of coherent scattering of photons into the cavity. Moreover, there are also regions

of enhanced photon scattering, where the atoms only feel the periodic optical lattice. The interplay of ordered parameter regions, where no photons are scattered into the cavity and disordered parameter regions, where the photonic potential establishes a correlated disorder potential, leads to different interesting phase transitions in the phase diagram, which finally will also be discussed in this thesis.

2 Bose-Einstein condensates and optical lattices

Phase transitions occurring in the ground state properties of both the ordered and the disordered BH model are the main topic of this work. In the ordered system there exists a phase transition from the MI to the SF phase. In the MI phase the system exhibits an energy gap in the particle excitation spectrum preventing particles from tunneling causing the incompressibility of the whole Bose gas. However, in the SF phase this energy gap closes, which means that tunneling between the sites becomes favorable for the particles. The ground state in this phase is coherent. Therefore, the MI-SF phase transition is a transition from localization in position space (MI phase) to localization in momentum space (SF phase). In the disordered system the BG phase occurs in between. Here the Bose gas is compressible, as in the SF phase, but the ground state is not yet coherent as in the MI phase. In this chapter we will discuss the fundamental theory as well as the experimental techniques used in order to proof the existence of the phase transitions. In the second part the derivation of the BH model involving the introduction of Wannier functions and of the BH parameters will be presented. In the end we will give an overview on the phase diagrams of the two situations calculated on the basis of perturbative descriptions will be given.

2.1 Ultracold bosons

The BH model describes bosons confined in an optical lattice. Bosons have an integer spin and thus can occupy the same energy eigenstate. An Bose gas of bosons shows a phase transition from an energy distribution according to the whole range of the Bose-Einstein statistics to a state where a macroscopic part of the particles occupy the ground state forming a so-called Bose-Einstein condensate (BEC). A single boson can be described by a wave packet with its width given by the De-Broglie wave length. As the temperature decreases this wave length increases and as it reaches the mean atomic distance the waves of different particles overlap and the formation of the BEC sets in. Theoretically this phase transformation was predicted by Einstein [58] and Bose [59] in 1924. In order to reach this regime in experiments a high density of bosons in the gas phase at very low temperatures in the μK regime are necessary. The bosons prepared in this way and right before they undergo the transition to a BEC, are called thermal or atomic cloud. The challenging experiments, where a thermal cloud has been prepared and finally formed a BEC, have been realized in 1995 [60–62] and since has inspired physicists to innovative work on both experiments and theory and thus founded a new research field.

With the help of optical traps and lattices, constructed by counter propagating laser beams, in which the BEC is confined and atoms can occupy individual sites, a variety of many-body Hamiltonians can be realized experimentally [11–13]. It was shown theoretically [1] and experimentally [21] that there is a phase transition from a ground state, localized in position space (MI phase) to another one, localized in momentum space (SF phase). Additionally disorder can be introduced to the regular lattice, which leads to the appearance of the Bose glass (BG) phase in-between [1, 3]. These lattice models are described by the Bose-Hubbard model [10]. The advantage of such optical setups is the precise control of all system parameters. This is of interest especially in the field of quantum optics and quantum computing, where high controllability is indispensable, as well as for the experimental modeling of other Hamiltonians [14–18].

In this chapter we will theoretically discuss the BEC and its connection to a SF as well as the basic experimental techniques for the production of a BEC and for the detection of the MI-BG-SF transitions. Afterwards the BH model is derived, connecting the relevant experimental parameters to the model parameters, followed by a discussion of the phase transitions in ordered and disordered lattices.

2.1.1 Bose-Einstein condensate

For the theoretical description of the BEC we start with an ideal Bose gas, which is described by the Bose-Einstein statistics of the occupation number

$$n_{\vec{p}}(\vec{r}) = \frac{1}{e^{\beta(\epsilon(\vec{p})-\mu)} - 1} \quad (2.1)$$

of the energy levels $\epsilon(\vec{p}) = p^2/(2m) = \epsilon_p$ of bosons, where $\beta = 1/(k_B T)$ is the inverse temperature [22]. In order to get positive occupations number the chemical potential μ is restricted to $\mu \leq \epsilon_p$. For the lowest energy level $\epsilon_0 = 0$ the Bose-Einstein statistic diverges for $\mu = 0$. Therefore, it is useful to separate the total number of particles

$$N = \sum_{p=0}^{\infty} n_{\vec{p}} = N_0 + N_T \quad (2.2)$$

into the occupation number of the ground state

$$N_0 = \frac{1}{e^{-\beta\mu} - 1} \quad (2.3)$$

and the thermal cloud

$$N_T = \sum_{p=1}^{\infty} \frac{1}{e^{\beta(\epsilon_p-\mu)} - 1}. \quad (2.4)$$

Replacing the sum by an integral, the thermal part can be rewritten as

$$N_T = \frac{V}{(2\pi\hbar)^3} \int d^3p \frac{1}{e^{\beta(\epsilon_p-\mu)} - 1} = \frac{V}{\lambda_T^3} g_{3/2}(e^{\beta\mu}), \quad (2.5)$$

where V is the volume of the Bose gas and

$$\lambda_T = \sqrt{\frac{2\pi\hbar^2}{mk_B T}} = \sqrt[3]{\frac{g_{3/2}(e^{\beta\mu})}{n}} \quad (2.6)$$

is the thermal wavelength. The Bose function [22]

$$g_p(z) = \frac{1}{(p-1)!} \int_0^\infty dx x^{p-1} \frac{1}{z^{-1}e^x - 1} \quad (2.7)$$

satisfies the recursive relation

$$g_p(z) = z \frac{dg_{p+1}(z)}{dz}. \quad (2.8)$$

For $p = 3/2$ this function increases as a function of $z = e^{\beta\mu}$ until at $z = 1$ it assumes its maximal value $g_{3/2}(1) \approx 2.612$. In this limit ($\mu = 0$, $z = 1$) and on the basis of Equation (2.6) the characteristic temperature

$$T_c = \frac{2\pi\hbar^2}{mk_B} \left(\frac{n}{g_{3/2}(1)} \right)^{\frac{2}{3}} \quad (2.9)$$

can be defined and Equation (2.5) can be written in the form

$$N_T = N \left(\frac{T}{T_c} \right)^{\frac{3}{2}} \frac{g_{3/2}(e^{\beta\mu})}{g_{3/2}(1)}. \quad (2.10)$$

From equations (2.3) and (2.10) we see that the total particle number behaves differently above ($T > T_c$) and below ($T < T_c$) the characteristic temperature T_c . If the temperature is higher than the characteristic temperature T_c the occupation of the ground state N_0 is finite and can be neglected in comparison to the thermal part N_T . The atoms occupy excited states and form a thermal cloud. With decreasing temperature the particle number N_T of the thermal cloud shrinks according to Equation (2.10), while the occupation number of the ground state follows

$$N_0 = N \left(1 - \left(\frac{T}{T_c} \right)^{\frac{3}{2}} \right). \quad (2.11)$$

For decreasing temperature more and more bosons populate the ground state, which below the characteristic temperature T_c is macroscopically occupied. Only for an ideal Bose gas, as discussed here, finally all particles occupy the ground state. In general, for an interacting Bose gas, only a certain fraction of the particles condenses while the rest remains as a thermal cloud. The macroscopic population of the ground state is called BEC [58, 59, 63].

In the case of a BEC the many body wave function of the system is given then by

$$\Psi(\vec{x}_1, \dots, \vec{x}_N, t) = \prod_{i=1}^N \chi_0(\vec{x}_i, t), \quad (2.12)$$

where $\chi_0(\vec{r}, t)$ is the single particle ground state wave function. This equations is valid for a dilute gas, where, in the framework of the Hartree-Fock approximation, correlations among particles can be neglected in first approximation [22]. In a mean-field description the condensate wave function $\Psi_0(\vec{r}, t) = \Psi_0(\vec{r}) e^{-i\mu t/\hbar}$ can therefore be written according to

$$\Psi_0(\vec{r}, t) = \sqrt{N_0} \chi_0(\vec{r}, t), \quad (2.13)$$

which is described by the Gross-Pitaevskii equation; further details are discussed in Section A.2 and the textbooks [22, 64, 65]. In the case of an interacting Bose gas the total macroscopic wave function can then be written according to

$$\Psi(\vec{r}, t) = \Psi_0(\vec{r}, t) + \delta\Psi(\vec{r}, t) \quad (2.14)$$

as the sum of the condensate wave function $\Psi_0(\vec{r}, t)$, and the so-called depletion wave function $\delta\Psi(\vec{r})$, describing the non-condensed particles [22].

A BEC exists below the characteristic temperature $T_c(n)$, which is given by Equation (2.9) and depends on the density $n = N/V$ of the Bose gas. For fixed temperature T the Equation (2.9) defines a characteristic density n_c below which the BEC occurs. Therefore, the experimental challenge is to form a dilute Bose gas and to cool it below the characteristic temperature T_c .

This experiment has first been realized in 1995 with Rubidium [60], Lithium [61] and Sodium [62] atoms by three groups simultaneously. The first step of cooling of the Bose gas, confined in a magneto-optical trap, is achieved by laser cooling [66–68]. The laser is blue detuned with respect to an atomic transition. Because of the Doppler effect an atom moving towards the laser absorbs a laser photon and gains the energy $\hbar\omega$. By fluorescence the atom emits a photon in a random direction. Since the direction of the emission is distributed isotropically in space, a row of these processes leads to a slowing of the atom in direction of the laser. The simultaneous laser cooling in all three spacial dimensions reduces the average velocity and thus also the temperature. The cooling with this technique is limited from below at around $140\mu\text{K}$ for Rubidium atoms. Afterwards the slow atoms with a velocity of some cm/s are loaded into a magnetic or optical trap. The second cooling process is called evaporative cooling [69, 70]. For this process the trapping barrier is lowered such that the fastest particles can leave the trap. The remaining particles thermalize in the trap and reach a density and temperature, with which they finally undergo the transition to a BEC. In typical experiments temperatures of between $500n\text{K}$ and $2\mu\text{K}$ with densities of $10^{14} - 10^{15} \text{ cm}^{-3}$ are reached [71].

2.1.2 Superfluid

The formation of a BEC below the critical temperature is not the only feature of an interacting Bose gas. Moreover, it can also show all properties of a SF. Therefore, the occurrence of a SF in context with a BEC is widely discussed. A SF shows zero viscosity, which means that it flows without inner friction. In turn an obstacle moving in a SF cannot set the fluid in motion or excite the fluid.

In order to describe this phenomenon, suppose there is a heavy obstacle moving with

velocity \vec{v} in a viscous fluid of mass M . In the coordinate system K , where the obstacle is at rest, the energy is given by E and the momentum by \vec{p} . In the coordinate system K' moving with the same velocity \vec{v} as the fluid, the ground state is given by E_0 and has zero momentum $|\vec{p}| = 0$ [64].

Due to the Galilean transformation, the ground state energy in the system K moving with the obstacle is given by

$$E = E_0 + \frac{1}{2}M\vec{v}^2. \quad (2.15)$$

If there is one single excitation in the fluid, in the system K' the ground state energy

$$E = E_0 + \varepsilon(\vec{p}) \quad (2.16)$$

is then given as the sum of the ground state energy E_0 in the system K' and the excitation $\varepsilon(\vec{p})$. Therefore, the energy in the system K , where the obstacle is fixed, is given by

$$E = E_0 + \varepsilon(\vec{p}) - \vec{p}\vec{v} + \frac{1}{2}M\vec{v}^2. \quad (2.17)$$

By comparing Equation (2.15) to (2.17), we may conclude that one excitation costs the energy $\varepsilon(\vec{p}) - \vec{p}\vec{v}$. Therefore, the spontaneous creation of excitations only occurs in the regime, where the energy necessary for one excitation is negative

$$\varepsilon(\vec{p}) - \vec{p}\vec{v} < 0. \quad (2.18)$$

Therefore, there exists a critical velocity

$$v_c = \min_{\vec{p}} \frac{\varepsilon(\vec{p})}{|\vec{p}|} \quad (2.19)$$

above which excitations are possible [64]. Below this threshold it is impossible to create excitations, which means that there is no mechanism for degrading the motion of the fluid. In this situation the fluid moves without inner friction and forms a SF. Therefore, the so-called Landau criterion states that only for small velocities v less than the critical velocity v_c a fluid can be a SF [64].

As the excitation spectrum for an ideal Bose gas is given by $\varepsilon(\vec{p}) = \vec{p}^2/(2m)$, according to Equation (2.19) the critical velocity v_c is zero. Thus, an ideal Bose gas cannot be SF. However, an interacting Bose gas indeed can be SF. To see this, we have a look on the excitation spectra for a weakly and strongly interacting Bose gas as shown in Figure 2.1. For a weakly interacting Bose gas the Bogoliubov excitation spectrum is given by

$$\varepsilon(\vec{p}) = \sqrt{\frac{\vec{p}^2}{2m} \left(\frac{\vec{p}^2}{2m} + 2n_0U_0 \right)}, \quad (2.20)$$

where n_0 is the density of particles in the limit of zero momentum and U_0 is the inter-particle interaction [64]. For large momenta $|\vec{p}|$ it approaches the dispersion relation of a free particle,

$$\varepsilon(\vec{p}) \approx \frac{\vec{p}^2}{2m} + n_0U_0 \quad \text{for} \quad |\vec{p}| \rightarrow \infty. \quad (2.21)$$

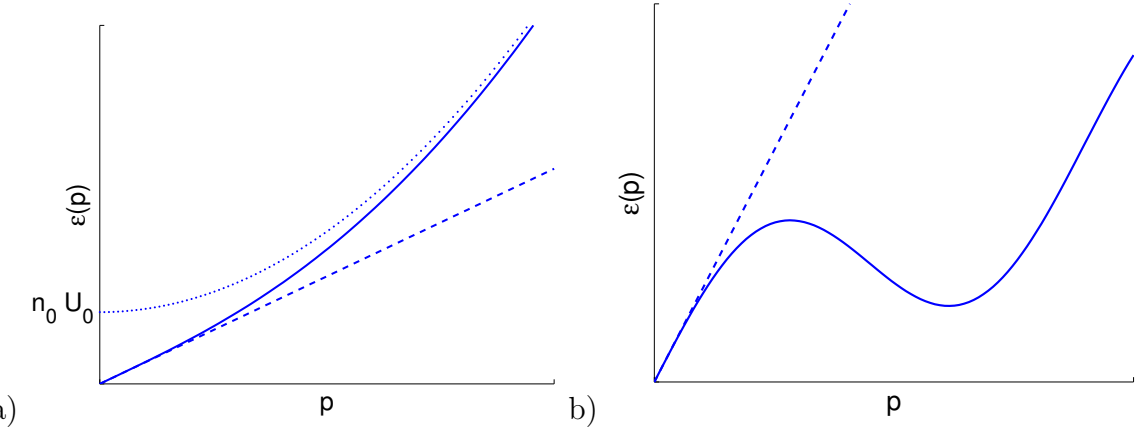


Figure 2.1: Dispersion relation for a Bose gas with weakly interacting (a), as given in equation (2.20), and strongly interacting particles (b). The dashed line describes the linear behavior for small momentum $|\vec{p}|$ and the dotted the limit for large momentum $|\vec{p}|$.

In the limit of small momenta $|\vec{p}|$ the Bogoliubov excitation spectrum (2.20) becomes linear in the momentum $|\vec{p}|$ according to

$$\varepsilon(\vec{p}) \approx |\vec{p}| \sqrt{\frac{n_0 U_0}{m}} \quad \text{for} \quad |\vec{p}| \rightarrow 0, \quad (2.22)$$

describing phonon excitations. According to the Landau criterion (2.19), the critical velocity v_c is given by the speed of sound $c = \sqrt{n_0 U_0 / m}$. Therefore, a weakly interacting Bose gas indeed fulfills the Landau criterion and can behave as a SF.

The excitation spectrum for a strongly interacting Bose gas is shown in Figure 2.1 b). In the limit of small momenta also we find here a linear dependency on the momentum $|\vec{p}|$. The critical velocity, however, is smaller than the one in the weakly interacting case. Thus, we conclude that an interacting Bose gas show a SF phase in the weakly as well as strongly interacting limit.

2.1.3 Bose-Einstein condensate and Superfluid

The BEC represents the macroscopic occupation of the ground state below the characteristic temperature T_c , as described in Section 2.1.1. However, SF fluids according to the Landau criterion occur, if there exists a critical velocity (2.19), below which a moving obstacle cannot create excitations. In general, these criteria describe different features of a Bose gas and do not hint to the idea that BECs and SF might be identical. And indeed there are differences, as for example, a non-interacting BEC cannot be SF, as discussed in the last section. Therefore, we will analyze the relationship of BECs and SFs in more detail in this section.

The Galilean transformation of some wave function $\Psi(\vec{r}, t)$ to a frame moving with velocity \vec{v} is in general given by

$$\Psi'(\vec{r}, t) = \Psi(\vec{r} - \vec{v}t, t) \exp\left(\frac{i}{\hbar} \left(M\vec{v}\vec{r} - \frac{1}{2}M\vec{v}^2t\right)\right) \quad (2.23)$$

and thus leads to an additional phase factor. This implies that the absolute value of the wave function $|\Psi(\vec{r}, t)|^2$ is invariant under this transformation.

Assume there is a condensate wave function Ψ_0 , describing the particles in the macroscopically occupied ground state, which can be written as

$$\Psi_0(\vec{r}, t) = \Psi_0(\vec{r}) e^{-i\mu t/\hbar} \quad (2.24)$$

with the chemical potential μ [22]. Under the Galilean transformation this condensate wave function takes the form

$$\Psi_0(\vec{r}, t) = \Psi_0(\vec{r}) e^{i\phi} \quad (2.25)$$

where the phase is given by

$$\phi = \frac{1}{\hbar} \left(M\vec{v}\vec{r} - \left(\frac{1}{2}M\vec{v}^2 + \mu \right) t \right) \quad (2.26)$$

and $\Psi_0(\vec{r})$ remains unchanged. With equation (2.26) at hand, we can directly conclude that the velocity \vec{v} is proportional to the gradient of the phase ϕ :

$$\vec{v}_{SF} = \frac{\hbar}{M} \vec{\nabla} \phi. \quad (2.27)$$

This equation states that the phase plays the role of a velocity potential [22, 64, 65]. Notice, that for the derivation of Equation (2.27), we have only assumed to have a BEC, without any further constraints for example on the temperature or the density. As the phase ϕ is a scalar, according to Equation (2.27) a BEC is irrotational ($\vec{\nabla} \times \vec{v}_{SF} = 0$). Therefore, a BEC shows one main feature of a SF.

Notice that the condensed density $M|\Psi_0|$ and the SF density ρ_{SF} , however, are not identical. In an interacting Bose gas even at zero temperature there also exist particles, which do not occupy the ground state such that the condensed density $M|\Psi_0|$ is smaller than the total density ρ , while in the same situation all particles of the Bose gas are SF and the SF density ρ_{SF} equals the total density ρ . As a result the condensed density $M|\Psi_0|$ is smaller than the SF density ρ_{SF} , which means that also non-condensed particles belong to the SF.

2.1.4 Bose gas in optical lattices

Optical traps are a widespread technique to experimentally confine a BEC. Let us therefore discuss the interaction between light and matter in more detail. When an atom interacts with coherent laser light, the electric field $\vec{E}(\vec{r}, t)$ of this laser light induces an atomic dipole moment $\vec{d}(\vec{r}, t)$, which oscillates at the some frequency ω . The resulting potential is given by [72]

$$V_{\text{dip}} = -\frac{1}{2} \langle \vec{d} \cdot \vec{E} \rangle_t = -\frac{1}{2\epsilon_0 c} \text{Re}(\alpha) V(\vec{r}), \quad (2.28)$$

where the brackets denote the time average, $\alpha(\omega)$ is the polarization and the intensity $V(\vec{r})$ can be calculated according to

$$V(\vec{r}) = 2\epsilon_0 c |\vec{E}(\vec{r})|^2. \quad (2.29)$$

Thus, the resulting trapping force acting on the atoms may be written as

$$\vec{F}_{\text{dip}} = -\nabla V_{\text{dip}} = \frac{1}{2\epsilon_0 c} \text{Re}(\alpha) \nabla V(\vec{r}) . \quad (2.30)$$

It can be shown, that the potential

$$V_{\text{dip}} \sim \frac{V(\vec{r})}{\Gamma} \quad (2.31)$$

is proportional to the quotient of the laser intensity $V(\vec{r})$ and the detuning $\Gamma = \omega - \omega_0$ of the laser frequency ω and the atomic transition ω_0 [72].

This trapping force (2.30) can be used to produce an optical lattice. In one dimension a laser with the field

$$\vec{E}(\vec{r}, t) = E_0 \left(e^{i\vec{k}\vec{r}} + e^{-i\vec{k}\vec{r}} \right) \quad (2.32)$$

and the wave vector \vec{k} is reflected into itself, which leads to an interference pattern, where the intensity changes according to

$$V(x) = V_0 \cos^2(kx) \quad (2.33)$$

and the factor V_0 is proportional to the intensity of the laser. The recoil energy is given by $E_R = \hbar^2 k^2 / (2m)$. The atoms in this potential either rest at the maxima or at the minima of this potential, depending on the sign of the force \vec{F}_{dip} (2.30): Below the resonance ("red" detuning) where Γ is negative, the force \vec{F}_{dip} is attractive and the atoms move into the direction of higher field intensity. Thus, for the atoms the potential minima are at the positions with maximal intensity. On the other side of the resonance ("blue" detuning) Γ is positive, the force \vec{F}_{dip} is repulsive and the atoms move out of regions with high intensity. Therefore, the potential minima for the atoms coincide with the intensity minima in this case. By increasing the number of laser beams, periodic optical potentials can analogously be produced in 2D and 3D. By varying the frequencies, the intensities and the angles between the lasers a huge variety of different lattice configurations can be produced [13].

Ultracold bosons in a regular, square optical lattice show a transition from the MI, for high laser intensities where the optical lattice is deep, to the SF phase, for lower laser intensities where the lattice is shallow. In the MI phase the particles are localized in position space, since there exists an energy gap in the particle excitation spectrum, which means that adding a particle at some site costs energy. Moreover, this energy gap prevents the particles from tunneling, such that the Bose gas cannot be compressed by a small external potential. In the SF phase the energy gap in the particle excitation spectrum is closed and the particles can move freely without any energy cost. This situation resembles the frictionless movement of a SF showing zero viscosity as discussed in Section 2.1.3. This means that the particles are delocalized in positions space, leading to a sharp localization in the phases. The ground state can be described by a Glauber coherent state, which are introduced in Appendix A.1. Due to the closed energy gap, the Bose gas can be compressed by an external potential, which means that it is compressible.

If the optical lattice is disordered, which can experimentally be realized for example by a bi-chromatic potential, discussed in Chapter 6, the BG phase occurs between the MI and SF phase in the phase diagram [19, 20]. In the BG phase the energy gap of the particle excitation spectrum is closed, which enables particle to move from one site to the other. That is why the Bose gas is compressible, just as the SF phase. But still the ground state is not coherent, which is similar to the MI phase. Thus, the BG phase exhibits features of both the MI as well as the SF phase. The BG phase is called glass, as the density does not show a crystalline structure, as in the MI phase, but rather an amorphous, non-crystalline shape. A detailed discussion of the nature of this phase is a main topic of this thesis and will be given in Chapter 4.

2.1.5 Experimental observation of the phase transitions

The MI-SF transition in an ordered optical lattice has been experimentally shown in [21]. In this experiment ultracold ^{87}Rb atoms are confined in a 3D optical lattice. In order to detect the phase of the system in the trap, one makes use of the coherence of the macroscopic wave function of the BEC. The coherence of BECs was impressively shown in [73], where the interference pattern of two interfering BECs in a double well potential was observed. In a lattice system the coherence of the condensed fraction of the Bose gas in the trap can, therefore, be detected by using the technique of time-of-flight imaging. In this framework the trap is switched off after the experiment such that the Bose gas can evolve freely in space. An absorption image of the resulting cloud then shows regular interference peaks if there exists a condensed fraction of particles macroscopically occupying the same state and a diffuse density profile if not.

In order to understand this, we take a closer look on the density in the trap in momentum space $n(\vec{p})$ and position space $n(\vec{r})$ after the time-of-flight. The initial density

$$n(\vec{p}) = n_0(\vec{p}) + n_T(\vec{p}) \quad (2.34)$$

consists of a condensed $n_0(\vec{p})$ and a thermal component $n_T(\vec{p})$ with a total number of $N = \int d\vec{p} n(\vec{p})$ particles. The density of the condensate is given by the mean square of the condensate wave function and can be represented by [22]

$$n_0(\vec{p}) = N_0 |\Psi_0(\vec{p})|^2 = N_0 \left(\frac{1}{\hbar \pi m \omega_{\text{ho}}} \right)^{\frac{3}{2}} \exp \left(-\frac{m}{\hbar t^2} \sum_{k=x,y,z} \frac{r_k^2}{\omega_k} \right), \quad (2.35)$$

where the momentum is given by $\vec{p} = m\vec{r}/t$, the number of condensed particles by N_0 and the geometric average $\omega_{\text{ho}} = (\omega_x \omega_y \omega_z)^{1/3}$ of the three oscillator frequencies. The thermal fraction is given by [22]

$$\begin{aligned} n_T(\vec{p}) &= \frac{1}{(2\pi\hbar)^3} \int d\vec{r} n_{\vec{p}}(\vec{r}) \\ &= \frac{1}{(\lambda_T m \omega_{\text{ho}})^3} g_{\frac{3}{2}} \left[\exp \left(-\frac{\beta m r^2}{2t^2} \right) \right], \end{aligned} \quad (2.36)$$

where the thermal wavelength λ_T is given by Equation (2.6) and $n_{\vec{p}}(\vec{r})$ by the Bose-Einstein statistic (2.1). We assume that the particles do not interact during the time of flight and thus perform a ballistic expansion. Let us take a look at the densities after the free expansion. The condensate density in position space is then given by [22]

$$n_0(\vec{r}, t) = N_0 \left(\frac{m\omega_{ho}}{\hbar\pi} \right)^{\frac{3}{2}} \exp \left(-\frac{m}{\hbar} \sum_{k=x,y,z} \frac{\omega_k}{1 + \omega_k^2 t^2} r_k^2 \right) \prod_{k=x,y,z} \frac{1}{\sqrt{1 + \omega_k^2 t^2}}. \quad (2.37)$$

For sufficient long times ($\omega_k t \gg 1$) this reduces to

$$n_0(\vec{r}, t) \rightarrow N_0 \left(\frac{m}{\hbar\pi t^2 \omega_{ho}} \right)^{\frac{3}{2}} \exp \left(-\frac{m}{\hbar t^2} \sum_{k=x,y,z} \frac{r_k^2}{\omega_k} \right). \quad (2.38)$$

The thermal part may be written according to [22]

$$n_T(\vec{r}, t) = \frac{1}{\lambda_T^3} g_{\frac{3}{2}} \left[\exp \left(-\frac{\beta m}{2} \sum_{k=x,y,z} \frac{\omega_k^2}{1 + \omega_k^2 t^2} r_k^2 \right) \right] \prod_{k=x,y,z} \frac{1}{\sqrt{1 + \omega_k^2 t^2}}, \quad (2.39)$$

which in the limit $\omega_k t \gg 1$ reduces to

$$n_T(\vec{r}, t) \rightarrow \frac{1}{(\lambda_T t \omega_{ho})^3} g_{\frac{3}{2}} \left[\exp \left(-\frac{\beta m r^2}{2t^2} \right) \right]. \quad (2.40)$$

A comparison of Equation (2.38) and (2.40), describing the densities after a free expansion of sufficiently long time ($\omega_k t \gg 1$), with the initial densities in momentum space (2.35) and (2.36) shows that they are proportional and fulfill the equality

$$n(\vec{r}, t) = \left(\frac{m}{t} \right)^3 n(\vec{p}). \quad (2.41)$$

This means that after the free expansion the density in position space is proportional to the momentum distribution of the trapped system, if the interaction of the atoms during the process of free expansion is negligible and the time of free expansion is sufficiently long.

In Figure 2.2 absorption images after the time-of-flight are shown for increasing values of the potential depth V_0 [21]. In a shallow lattice there exists a main maximum, which is accompanied by a regular pattern of lower maxima, showing that the original state in the trap was coherent. In deep lattices this interference pattern vanishes and is replaced by a diffuse Bose gas. In this regime the state in the trap exhibits no phase coherence, corresponding to a MI state. In order to show that the loss of phase coherence is due to this transition and to exclude other processes, it was shown that starting from a MI configuration phase coherence can be restored by lowering the lattice depth again.

Alternatively the different phases can be detected by Bragg spectroscopy, where the particle excitation spectrum of the system is measured [3, 21, 23, 24, 74]. If a particle moves from one site to another, it has to pay the energy U if the other site is already occupied.

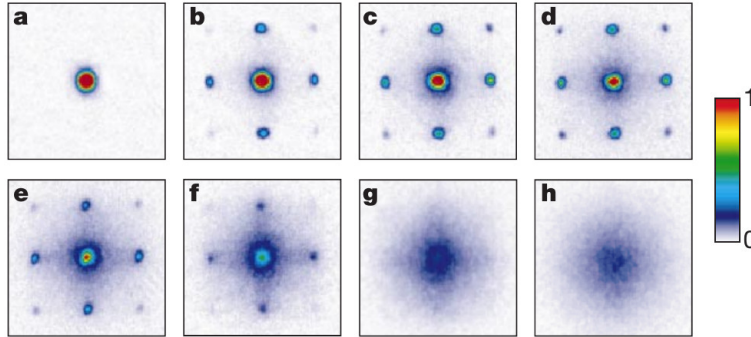


Figure 2.2: Absorption images of the 2D Bose gas after a time-of-flight of 15 ms for different values of the potential depth $V_0/E_R = 0, 3, 7, 10, 13, 14, 16, 20$. The figure is taken from [21].

In a MI configuration, where tunneling is suppressed, the particle does not possess enough energy to overcome this energy gap. Since in the SF regime the energy gap is closed, tunneling is favorable and particles are free to tunnel to other sites. In order to study this excitation spectrum in experiment a perturbative potential is applied in addition to the optical lattice. This can be realized by a potential gradient with an energy difference ΔE between neighboring sites [21] or a sinusoidal modulation with the amplitude being approximately 30% of the main lattice height s_1 and some frequency ν [3]. In the SF regime the particle-hole excitation can be stimulated easily for all values of the parameters ΔE or ν . In the MI phase the excitation is only possible for specific energies, which are multiples of the energy U . The width of the interference peak of the time-of-flight images versus the energy difference ΔE is shown in Figure 2.3. In the SF regime particle-hole excitations are possible for every value of ΔE as can be seen in Figure 2.3 c). For the other parameters, representing MI configurations, two peaks at multiples of the energy U are visible. Therefore, the existence of a energy gap in the particle-hole excitations spectrum can be measured by Bragg spectroscopy.

With the help of both, the measurement of coherence with time-of-flight images and the probing of the excitation spectrum by Bragg spectroscopy, the authors [21] conclude that the MI-SF transition occurs between $V_0/E_R = 10(1)$ and $V_0/E_R = 13(1)$, which corresponds to $U/J \approx 36$ for the second value.

Moreover, with the help of trap squeezing spectroscopy [25, 75], the compressibility of the Bose gas can also be measured directly. Suppose in addition to the optical lattice there exists a harmonic confinement, which can be tuned independently. By varying the amplitude of this potential the Bose gas can be compressed. An accompanying measurement of the radius of the Bose gas via absorption imaging, shows if the Bose cloud is compressible or not. This method, however, is bounded by the resolution of the absorption imaging. Such a system with regular optical lattices can be extended by introducing disorder to the system. Experimentally there are in general two possibilities: The first one is the introduction of a diffuser, which randomly modulates the intensities of an additional laser and in superposition with the optical lattice leads to local inhomogeneities in the lattice potential, in which the atoms move [27]. The distribution of local inhomogeneities, and especially the disorder strength, however, is unique for the diffuser used in the experi-

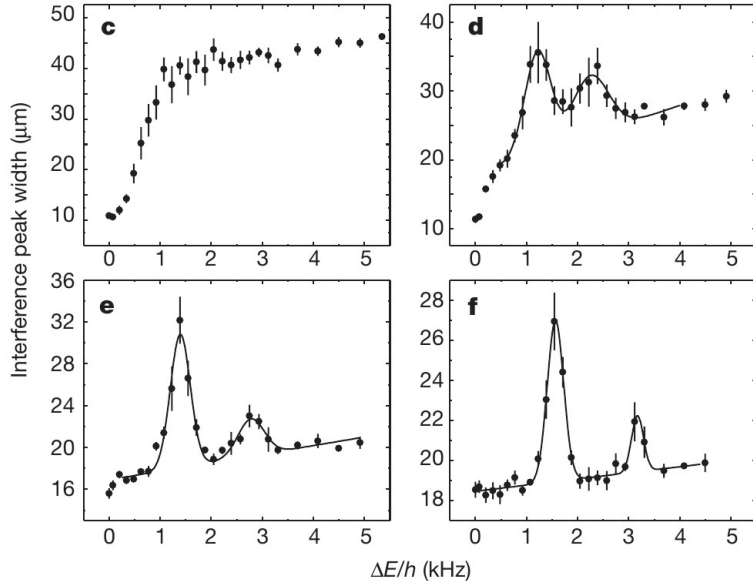


Figure 2.3: Excitation spectrum of the Bose gas resulting from Bragg spectroscopy for different values of the potential depth $V_0/E_R = 10, 13, 16, 20$ as a function of the energy difference ΔE between neighboring sites. The figure is taken from [21].

ment and cannot be adjusted to different values. The second opportunity is to use of a bi-chromatic optical potential [3, 26]. Here the main optical lattice is overlapped by a second optical lattice, whose frequency is slightly shifted from and whose amplitude is smaller than that of the main lattice. By varying the amplitude of the second lattice the strength of disorder can be adjusted freely. The period of such pattern increases as the difference between the wave lengths shrinks. If the difference is chosen to be so small, that the period exceeds the system size, this quasi-periodic pattern serves as a model for uncorrelated disorder, which will be discussed in Chapter 6 in detail.

In this disordered configurations the so-called BG phase occurs between the MI and the SF phase. This phase exhibits properties of both, the MI and the SF phase. In the BG phase the ground state is not coherent, which means that the time-of-flight images show no regular interference peaks than rather a diffuse density cloud like in the MI phase. But yet, the energy gap in particle-hole excitation spectrum is closed like in the SF regime, which can be shown with Bragg spectroscopy. Therefore, with both experimental methods the parameter regime of the BG phase can be separated from the MI as well as from the SF regime. This has been realized in a 1D bi-chromatic optical lattice [3]. In dependence of the amplitudes of the lattices they found configurations, in which the time-of-flight images as well as the excitation spectrum show no precise peaks, which indicates that the system is in a non-coherent state, where the excitation gap is already closed, corresponding to the BG phase.

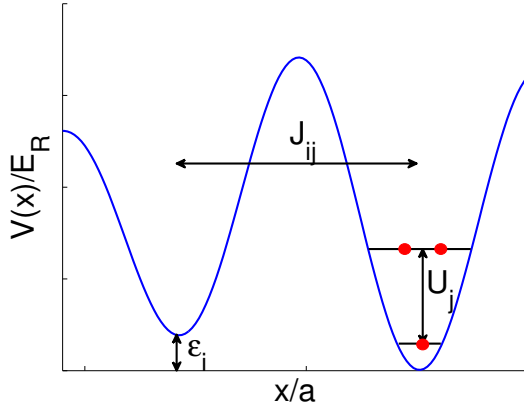


Figure 2.4: The BH Parameters and some 1D potential. The on-site energy ϵ_i describes the relative difference in the potential depth. The tunneling rate J_{ij} is the energy gain, that a particle gets by tunneling from one site to the neighboring. The inter-particle interaction U_i is the amount of energy that a second particle must pay, if it reaches an occupied site.

2.2 The Bose-Hubbard model

A laser reflected into itself forms a regular lattice potential for the atoms according to Equation (2.33). For a 2D system, which is under consideration in this work, the potential is given by

$$V(\vec{r}) = V_0 (\cos^2(kx) + \cos^2(kz)), \quad \vec{r} = (x, y), \quad (2.42)$$

where the wave vector $k = 2\pi/\lambda$, the lattice constant $a = \pi/k$ and the intensities $V_0 = sE_R$ are given in units of the recoil energy $E_R = \hbar^2 k^2 / (2m)$. In experiments ^{87}Rb atoms, which have an atomic transition at the wavelength of $\lambda = 830$ nm and a mass of $m_{\text{Rb}} = 1.45 \cdot 10^{-25}$ kg are widely used [3, 21]. The BH Hamiltonian

$$\hat{H} = \sum_i (\epsilon_i - \mu) \hat{n}_i + \sum_i \frac{U_i}{2} \hat{n}_i (\hat{n}_i - 1) - \sum_{\langle i,j \rangle} J_{ij} \hat{a}_i^\dagger \hat{a}_j \quad (2.43)$$

describes the behavior of bosons in such optical lattices [10]. The operator $\hat{n}_i = \hat{a}_i^\dagger \hat{a}_i$ is the particle number operator of bosons at site i , which can be annihilated and created by the operators \hat{a}_i and \hat{a}_i^\dagger respectively. The site index $i = 1, \dots, M$, where $M = L^2$ is the number of sites in a 2D lattice, represents a tuple of spatial coordinates (i_x, i_z) with $i_{x,z} = 1, \dots, L$, where L is lateral size of the square lattice. The last sum runs over all four ($Z = 4$) nearest neighbor pairs $\langle i, j \rangle$ of the lattice. In Figure 2.4 a 1D potential is shown. The BH parameter ϵ_i is the on-site energy, describing the relative differences in the potential depth. The tunneling rate J_{ij} is the energy, which a particle gets by tunneling, while the inter-particle interaction U_i is the amount of energy that a second particle must pay, if it reaches an occupied site. Therefore, the tunneling rate J_{ij} and the inter-particle interaction U_i are competing energy scales. All these parameters can be site dependent for the disordered or site independent for the ordered BH model. In this

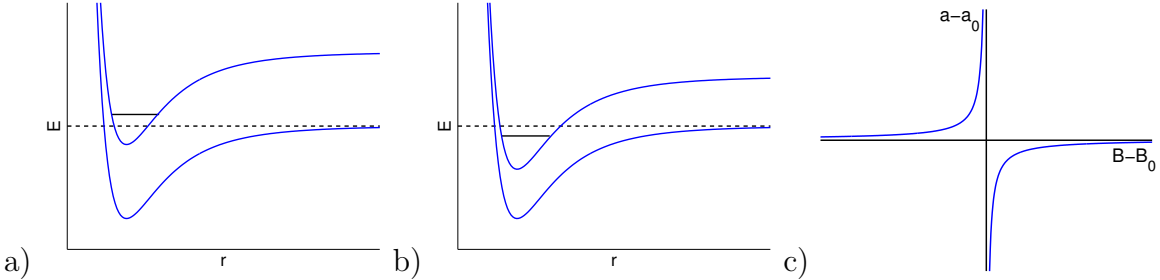


Figure 2.5: Scattering potential of two different spin states for a situation before (a) and after (b) the Feshbach resonance. Scattering length a as a function of the magnetic field B (c) in the vicinity of the Feshbach resonance at B_0 according to equation (2.44). Below the resonance the scattering length a is positive, while it becomes negative above.

system the chemical potential μ is a Lagrange multiplier determining the total particle number.

Especially remarkable is the high level of controllability of these systems in the experimental setup, where all parameters can be adjusted in a wide range. The ratio J_{ij}/ϵ_i is inverse proportional to the laser intensity. According to Equation (2.31) the potential for the atoms is small for low laser intensities resulting in a high tunneling rate J_{ij}/ϵ_i . On the other hand for large laser intensities the atoms are tightly confined to their lattice sites and the tunneling rate J_{ij}/ϵ_i is small. The explicit dependency of the BH parameter and the experimental parameters will be discuss in Section 6.1.2. For the adjustment of the inter-particle interaction U_i an additional magnetic field is necessary. In the vicinity of a Feshbach resonance the scattering length a and with it the inter-particle interaction U_i can be changed. Figure 2.5 a) and b) shows the scattering potential for two atoms as a function of their separation r for two different spin states. If the two considered spin states have opposite magnetic moment, their relative position can be shifted continuously by changing an externally applied magnetic field B . Therefore, it is possible to shift a bound state of the upper potential relatively to the dissociation energy of the lower potential. If the two levels are in resonance at some value B_0 of the magnetic field, the scattering length a diverges. In the vicinity of the Feshbach resonance the scattering length a can be described by the relation

$$a = a_0 \left(1 - \frac{\Delta_B}{B - B_0} \right), \quad (2.44)$$

where Δ_B describes the width of the resonance and a_0 the scattering length far from resonance as shown in Figure 2.5 c). Below the resonance the scattering length a is positive, while it becomes negative above the resonance. Since the inter-particle interaction U_i is proportional to the scattering length a , as we will see in Section 2.2.2, both regimes, i.e. attractive and repulsive inter-particle interaction U_i , can be realized in the vicinity of a Feshbach resonance.

2.2.1 Wannier Functions

To derive the BH Hamiltonian, we first introduce the so-called Wannier functions $W_n^l(\vec{r})$. According to the Bloch theorem [76] the Bloch functions

$$\psi_n^{\vec{q}}(\vec{r}) = u_{\vec{q}} e^{i\vec{q}\cdot\vec{r}}, \quad u_{\vec{q}}(\vec{r}) = \sum_{\vec{G}} c_n^{\vec{q}-\vec{G}} e^{-i\vec{G}\cdot\vec{r}} \quad (2.45)$$

are solutions of the stationary Schrödinger equation. In order to show this, we start with a periodic potential $V(\vec{r})$ like given in Equation (2.42), with lattice constant a and the Hamiltonian $\hat{H} = \hat{p}^2/(2m) + V(\vec{r})$. The Fourier-representation of such a potential is given by

$$V(\vec{r}) = \sum_{\vec{G}'} V_{\vec{G}'} e^{i\vec{G}'\cdot\vec{r}}, \quad (2.46)$$

where $\vec{G}' = 2\pi\vec{j}'/a$ is the reciprocal lattice vector and \vec{j}' is a vector of integer numbers. The ansatz

$$\psi_n(\vec{r}) = \sum_{\vec{k}'} c_n^{\vec{k}'} e^{i\vec{k}'\cdot\vec{r}} \quad (2.47)$$

and the transformation $\vec{k}' + \vec{G}' = \vec{k}$ lead to a stationary Schrödinger equation of the form

$$\sum_{\vec{k}} \left(\left(\frac{\hbar^2 \vec{k}^2}{2m} - E_n \right) c_n^{\vec{k}} + \sum_{\vec{G}'} V_{\vec{G}'} c_n^{\vec{k}-\vec{G}'} \right) e^{i\vec{k}\cdot\vec{r}} = 0. \quad (2.48)$$

Since $e^{i\vec{k}\cdot\vec{r}}$ are orthogonal functions, this equation must hold for every value of \vec{k} . Moreover, for every wave vector \vec{k} there exists a unique decomposition $\vec{k} = \vec{q} - \vec{G}''$, where the reciprocal lattice vector $\vec{G}'' = 2\pi\vec{j}''/a$ is chosen in a way that \vec{q} is a parameter defined in the first Brillouin zone (1.BZ). The additional transformation $\vec{G}' = \vec{G} - \vec{G}''$ leads to the equation

$$\left(\frac{\hbar^2 (\vec{q} - \vec{G}'')^2}{2m} - E_n \right) c_n^{\vec{q}-\vec{G}''} + \sum_{\vec{G}} V_{\vec{G}-\vec{G}''} c_n^{\vec{q}-\vec{G}} = 0. \quad (2.49)$$

This equation represents an eigenvalue problem for the coefficients $c_n^{\vec{q}-\vec{G}}$ of Equation (2.45). For a given energy level n the dimension of this eigenvalue problem is given by the dimension of the vector \vec{G}'' , which runs over the whole reciprocal lattice. In a numerical treatment the reciprocal lattice vector has to be truncated at a suitable value.

For the regular 1D potential, $V(x) = V_0 \cos^2(kx)$ the Fourier-transform of the potential reads

$$V_{G_x-G_x''} = \frac{1}{a} \int dx e^{iG_x x} = \frac{V_0}{4} [\delta(1-j+j'') + \delta(1+j-j'') + 2\delta(j-j'')] . \quad (2.50)$$

In this case the matrix representation of the operator of the eigenvalue problem (2.49) is a tridiagonal matrix. Exemplary some ground state Bloch functions $\psi_0^q(\vec{r})$ for the 1D

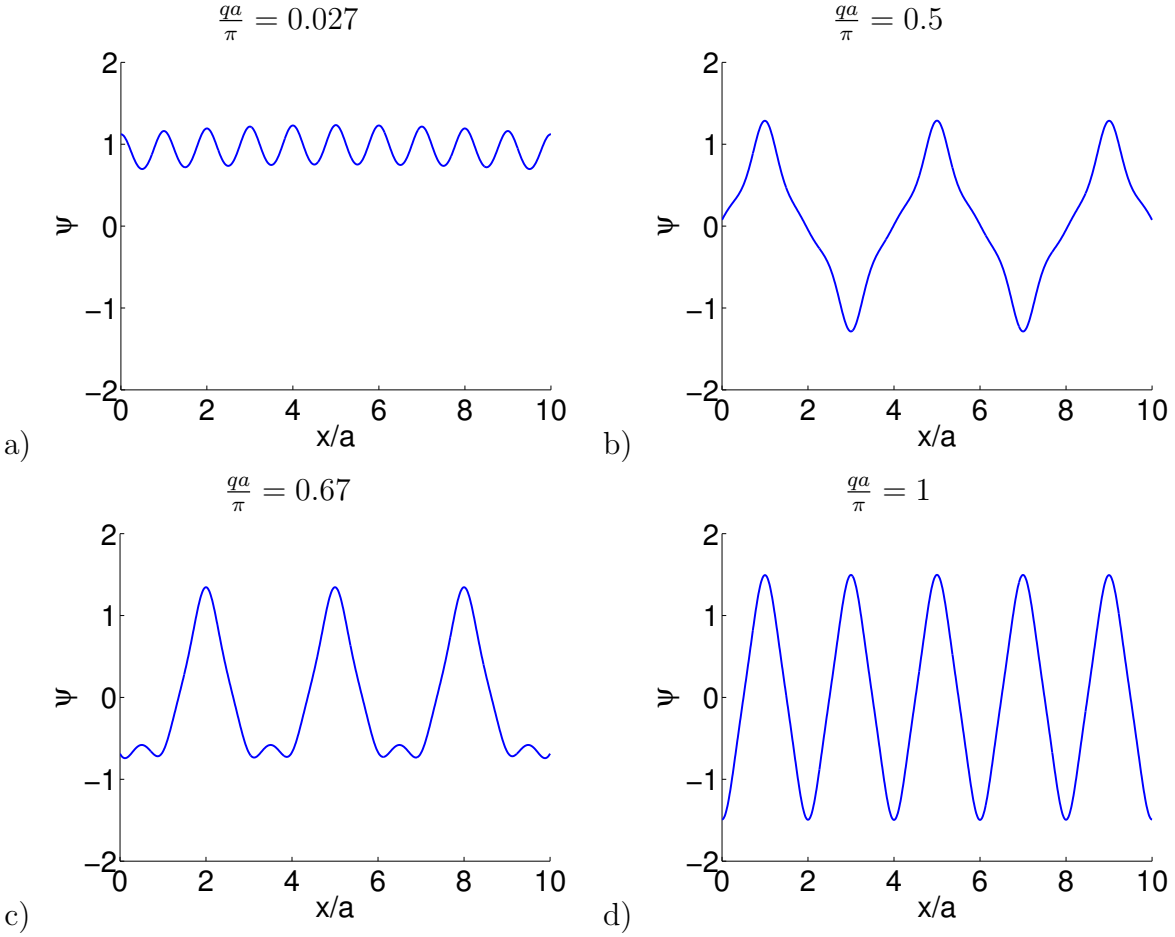


Figure 2.6: Bloch functions for a 1D ordered symmetric lattice with $s_1 = 2$, $s_2 = 0$ for $\frac{qa}{\pi} = 0.027, 0.5, 0.67, 1$.

potential are shown in Figure 2.6. They are periodic and spread over the whole lattice. Please note that the Bloch coefficients $u_{\vec{q}}(\vec{r})$ are also periodic functions.

Since the Bloch functions form an orthonormal basis, the Wannier functions can be construed by

$$W_n^l(\vec{r}) = \sqrt{\frac{2\pi}{a}} \frac{1}{M} \sum_{\vec{q} \in 1.BZ} \psi_n^{\vec{q}}(\vec{r}) e^{i\vec{q}\vec{x}_l} \quad \text{with} \quad \vec{x}_l = \vec{l}a, \quad (2.51)$$

and are localized at site $\vec{l} = (l_x, l_z)$. The set of Wannier functions are the Fourier transform of the set of Bloch functions. They are real functions, which fulfill $\int_V dV W_n^l(\vec{r})^2 = 1$. Moreover, they are symmetric due to the symmetry of the underlying lattice. Figure 2.7 shows a Wannier function for a regular 1D lattice. This wave function has a dominant occupation probability at one single site and significantly smaller probability at the neighboring sites.

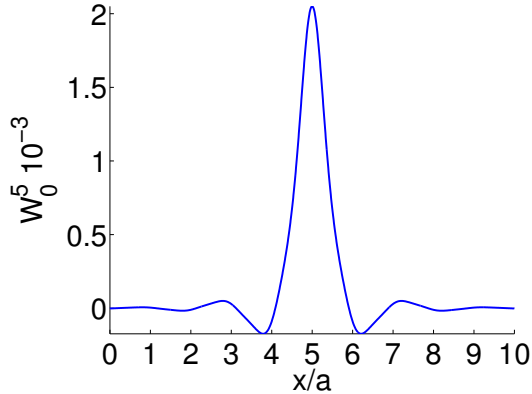


Figure 2.7: Wannier functions for a 1D symmetric lattice with $s_1 = 2$ and $s_2 = 0$ for $l = 5$ and $n = 0$. The function shows a dominant occupation probability at one single site and small probability at the neighboring sites.

2.2.2 Derivation

In order to derive the BH model we start with the quantum field theory Hamiltonian

$$\begin{aligned} \hat{H} = & \int d\vec{r} \vec{\Psi}^\dagger(\vec{r}) \left(-\frac{\hbar^2 \nabla^2}{2m} + V(\vec{r}) \right) \vec{\Psi}(\vec{r}) \\ & + \frac{1}{2} \int d\vec{r} d\vec{r}' \vec{\Psi}^\dagger(\vec{r}) \vec{\Psi}^\dagger(\vec{r}') U(\vec{r}, \vec{r}') \vec{\Psi}(\vec{r}') \vec{\Psi}(\vec{r}), \end{aligned} \quad (2.52)$$

describing bosons in some potential $V(\vec{r})$ in the quasi-ideal regime, where $U(\vec{r}, \vec{r}')$ describes the two particle interaction [22]. The field operator for a specific mode n

$$\vec{\Psi}(\vec{r}) = \sum_l W_n^l(\vec{r}) \hat{a}_l \quad (2.53)$$

can be composed into Wannier functions $W_n^l(\vec{r})$ and the creation operator \hat{a}_l creating a particle at site $\vec{l} = (l_x, l_z)$. In the tight-binding approximation the inter-particle interaction reduces to a contact interaction $U(\vec{r}, \vec{r}') = U_0 \delta(\vec{r} - \vec{r}')$ [64]. The effective inter-particle interaction in 2D is then given by

$$U_0 = \frac{\hbar^2 a_s}{m} \sqrt{\frac{8m\pi\omega_z}{\hbar}} = 5.56 \cdot 10^{-11} \hbar, \quad (2.54)$$

where $a_s = 5.2$ nm is the scattering length, $m_{\text{Rb}} = 1.45 \cdot 10^{-25}$ kg is the mass of the ^{87}Rb atoms and $\omega_z = 6\pi$ kHz is the frequency of the vertical confinement [6, 77–79]. Inserting the representation (2.53) into the quantum field Hamiltonian (2.52) the BH Hamiltonian in tight-binding approximation reads

$$\hat{H} = \sum_i (\epsilon_i - \mu) \hat{n}_i + \sum_i \frac{U_i}{2} \hat{n}_i (\hat{n}_i - 1) - \sum_{\langle i,j \rangle} J_{ij} \hat{a}_i^\dagger \hat{a}_j, \quad (2.55)$$

where the BH parameters ϵ_i , J_{ij} and U_i are given by

$$\begin{aligned}\epsilon_i &= \int d\vec{r} W_i(\vec{r}) \left(-\frac{\hbar^2 \nabla^2}{2m} + V(\vec{r}) \right) W_i(\vec{r}), \\ U_i &= U_0 \int d\vec{r} W_i^4(\vec{r}), \\ J_{ij} &= - \int d\vec{r} W_j(\vec{r}) \left(-\frac{\hbar^2 \nabla^2}{2m} + V(\vec{r}) \right) W_i(\vec{r}).\end{aligned}\quad (2.56)$$

Thus, the BH parameters can be determined using the Wannier function $W_i(\vec{r}) = W_0^i(\vec{r})$ of the ground state and the actual potential $V(\vec{r})$. The chemical potential μ is a Lagrange multiplier used to fix the total particle number $N = \sum_i \langle \hat{n}_i \rangle$.

For a symmetric optical potential (2.42) the local potentials at each lattice site is identical and thus the Wannier functions at all sites are the same. In this case the BH parameter are site independent, i.e., $\epsilon = \epsilon_i$, $U = U_i$, $J = J_i$ for all i . Then, the summand $\sum_i \epsilon_i \hat{n}_i = \epsilon \hat{N}$ in the Hamiltonian is proportional to the total number of particles and leads to a global shift of the spectrum, which does not influence the behavior of the system. Therefore, the BH Hamiltonian for a symmetric potential may finally be cast into the from

$$\hat{H} = -\mu \hat{N} + \frac{U}{2} \sum_i \hat{n}_i (\hat{n}_i - 1) - J \sum_{\langle i,j \rangle} \hat{a}_i^\dagger \hat{a}_j. \quad (2.57)$$

2.2.3 Phase diagrams

In the following the phase diagram for the ordered BH model are presented. The so-called Mott-lobes, which are the transition lines from the MI to the SF phase, can be described analytically in the framework of perturbation theory [48]. In the case of on-site disorder there also exists a perturbative description of the border of the MI region [49]. The MI regions, which still have the form of lobes, are surrounded by the BG phase for intermediate tunneling rates and finally by the SF phase for strong tunneling rates [1].

2.2.3.1 The ordered Bose-Hubbard model

The ground state of the BH model bears different characteristics in dependence of the system parameters. As discussed in Section 2.1.4, in the ordered system there occurs a phase transition from a MI to a SF phase. On the one hand in the MI phase there exists an energy gap in the particle excitation spectrum, which prevents the particles from tunneling and the ground state is localized in position space. On the other hand in the SF phase the energy gap is closed and the particles can tunnel without any energy cost, which makes the Bose gas compressible.

This phase transition in the parameter space of the ordered BH model can be described analytically [48]. For the ordered system the BH parameters for each site are identical, which means that the Hamiltonian is the same for each site. Within the so-called LMF approximation, which we will introduced and discuss in detail in Chapter 3, the

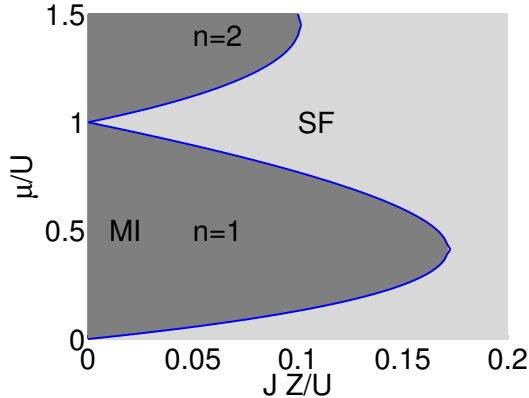


Figure 2.8: The phase diagram of the ordered BH model as predicted by perturbation theory [48] and given by Equation (2.61). Within the Mott-lobes the number of particles per site is fixed, while in the SF phase tunneling is favorable for the particles and the ground state is a coherent state.

BH Hamiltonian decomposes into a sum of local Hamiltonians, which are coupled in a mean-field way. The Hamiltonian for a single site in LMF approximation reads

$$\hat{H} = \mu \hat{n} + \frac{U}{2} \hat{n} (\hat{n} - 1) - J\eta (\hat{a} + \hat{a}^\dagger - \psi) , \quad (2.58)$$

with $\psi = \langle \text{gs} | \hat{a}^\dagger | \text{gs} \rangle$ being the local SF parameter and $\eta = Z\psi$, where Z is the number of neighboring sites. For small tunneling rates J the ground state energy for a state with n particles can be calculated in perturbation theory [48] yielding

$$E_n = \mu n + \frac{U}{2} n (n - 1) + JZ\psi^2 \left(\frac{JZn}{U(n - 1) + \mu} - \frac{JZ(n + 1)}{Un + \mu} + 1 \right) . \quad (2.59)$$

Following the Ritz method, we minimize the energy with respect to ψ and find an upper bound for the ground state energy. The first step yields the necessary condition

$$\frac{\partial E_n}{\partial \psi} = 2JZ\psi \left(\frac{JZn}{U(n - 1) + \mu} - \frac{JZ(n + 1)}{Un + \mu} + 1 \right) = 0 , \quad (2.60)$$

which leads to the transition line at

$$\begin{aligned} \mu_{\pm}(J, Z, U, n) &= -\frac{1}{2} (JZ - U(2n - 1)) \\ &\pm \sqrt{\frac{1}{4} (JZ - U)^2 - JZUn} . \end{aligned} \quad (2.61)$$

The chemical potential μ_{\pm} as a function of JZ/U for different values of n is shown in Figure 2.8. In this parameter plane the function (2.61) forms the so called Mott-lobes, which are numbered by integer values $n = 1, 2, \dots$. The function encloses individual MI

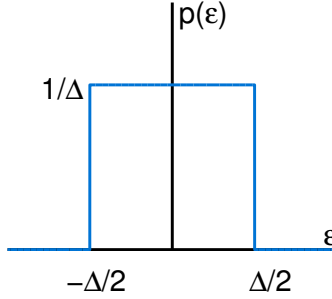


Figure 2.9: Probability density function $p(\epsilon)$ of the local on-site energies ϵ_i according to Equation (2.63). This distribution is symmetric around zero, has a width of Δ and a variance of $\sigma^2 = \Delta^2/12$.

regions in which the particle number per site equals the integer number n . Their tips are located at

$$\frac{\mu}{U} = -1 + \sqrt{n(n+1)} \quad \text{and} \quad \frac{JZ}{U} = 1 + 2n - 2\sqrt{n(n+1)}. \quad (2.62)$$

The Mott-lobes are aligned along the μ -axis and the particle number increases from lobe to lobe with growing μ . The upper and the lower part of the Mott-lobe is not symmetric with respect to the line $\mu/U = 3n/2 - 1$ and its tip is slightly below this line. While their extends along the μ/U -axis is always one, their width in JZ/U -direction shrinks with increasing n , but does not vanish in the limit $n \rightarrow \infty$. Therefore, there exists an infinite number of Mott-lobes.

2.2.3.2 The disordered Bose-Hubbard model

The main focus of this work is on the phase diagram of site dependent, inhomogeneous BH parameters. In this case the BH Hamiltonian is given by Equation (2.43), where all BH parameters are site dependent. The system, which is studied most, is the BH model with disordered on-site energies ϵ_i , while the other BH parameters J and U are treated as sharp values. The local on-site energy ϵ_i is then a random number drawn from a box distribution

$$p(\epsilon) = \frac{1}{\Delta} \Theta\left(\frac{\Delta}{2} - |\epsilon|\right), \quad (2.63)$$

where Δ is the strength of the disorder. This distribution, as shown in Figure 2.9, is symmetric around zero and its variance is given by $\sigma^2 = \Delta^2/12$. As discussed in Section 2.1.4, in the disordered scenario the so-called Bose glass phase occurs in between the MI and SF phase in the phase diagram [19, 20]. Similar to the SF phase also in the BG phase the energy gap in the particle excitation spectrum is closed, which means that the Bose gas is compressible, but still the ground state is not coherent just as in the MI phase.

A sketch of the phase diagram of the disordered BH model with on-site disorder is shown in Figure 2.10 for different values of the disorder strength Δ . This disorder scenario is a substantial part of this work and will be discussed in Chapters 3 and 4. An overview of the relevant phase diagrams is given in Section 5.1. Here, the MI-BG transition is

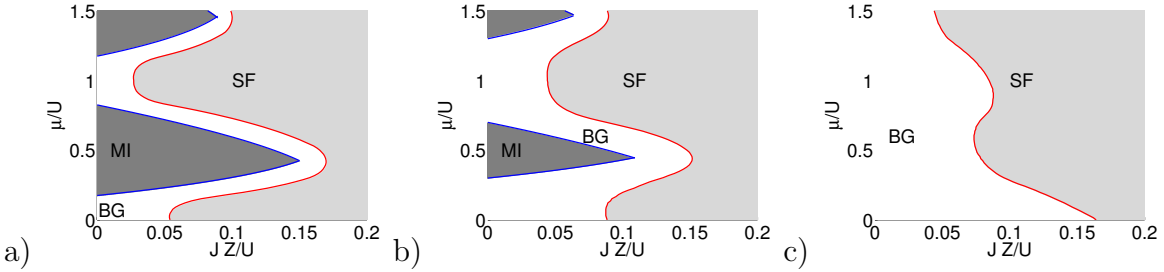


Figure 2.10: Sketch of the phase diagram of the BH model for box distributed disordered on-site energies ϵ_i according to distribution (2.63) for the disorder strengths $\Delta/U = 0.35, 0.6, 1.5$. The MI-BG transition shown in blue is given by the analytical perturbative result from [49]. The BG-SF transition is determined with LMF cluster analysis, which will be introduced in Chapter 4 and discussed in Section 5.1. The Mott-lobes along the μ/U -axis have a distance of Δ/U from each other and are completely surrounded by the BG phase [20]. For larger tunneling rates JZ/U the SF phase dominates the phase diagram.

given by the analytical perturbative result from [49]. In this paper the authors showed that, just as in the ordered case, the tip of the Mott-lobe lies slightly below the line $\mu/U = 3n/2 - 1$. Moreover, they found that in comparison to the ordered case, in the disordered case the upper (lower) part of the Mott-lobes is shifted downwards (upwards) by $\Delta/2U$, while their slope remains unchanged. Since for the BG-SF transition there exists no analytic result, the transition lines shown here have been determined via the LMF cluster analysis, which will be introduced in Chapter 4 and discussed in Section 5.1. Analogously to the ordered case we find Mott-lobes along the μ/U -axis, which now have a distance of Δ/U from each other. With increasing disorder strength Δ/U they shrink and vanish all simultaneously for $\Delta = U$. The Mott-lobes are completely surrounded by the so called BG phase [20]. The ground state in this phase is not coherent $\psi = 0$ like in the MI phase, but yet compressible, $\kappa > 0$, like in the SF phase. The Bose glass phase shows characteristics of both the MI and the SF phase, on which we will have a detailed look in Chapter 4. Finally, for large tunneling rates JZ/U the SF phase survives in the parameter region.

2.2.4 Numerical Methods

There exists a variety of sophisticated numerical methods in order to diagonalize the BH Hamiltonian (2.43), as its dimension

$$D = \frac{(N + M - 1)!}{N! (M - 1)!} \quad (2.64)$$

of the Hilbert space increases drastically with the number of particles N and sites M . Even though there are effective algorithms for the exact diagonalization of the BH Hamiltonian [80], the BH model can only be solved for small systems with a low number of particles and modes. That is why, there exists a whole bunch of numerical techniques or approximations in order to overcome this bound.

Quantum Monte-Carlo techniques, of which a short introduction is given in Appendix C, has been applied to the BH model in two [28–30, 32–36] as well as in three dimensions [20, 81, 82]. This algorithm includes all quantum effects and can be applied in the whole parameter regime of the model. The basis of this algorithm is the Trotter-Suzuki decomposition (C.14), which allows for a systematic decomposition of the partition function in so-called Trotter slices $\Delta\tau = it$ in imaginary time, where contributions on the order of $\Delta\tau^2$ are neglected. Advanced quantum Monte-Carlo methods, which operate in continuous imaginary time overcome this limit and hence eliminate this discretization error of $\Delta\tau^2$ [83–87]. Moreover, finite size effects occurring in every numerical simulation, can be treated with finite size techniques, which allows for a systematic and accurate description of the transition from a finite to the limit of an infinite system. Therefore, the combination of advanced quantum Monte Carlo algorithms with the systematic description of finite size effects improve the accuracy of quantum Monte-Carlo results up to a very high level and make the algorithm the most powerful technique for a huge class of quantum many-body systems.

In one dimension density-matrix renormalization group techniques [88] have been applied to BH models containing either quasi-periodic potentials [37–39] or a uniform distribution of disorder strength [40, 41]. Within this treatment the many-body quantum state of a system at low energies - and especially the ground state - can be determined with high accuracy in low dimensions. The technique corresponds to an iterative, variational algorithm, where in each step the whole chain of sites is decomposed into two blocks, which are separated by two sites. On the basis of this decomposition, which is called a superblock, a possible candidate for the ground state is determined. Within a row of systematically changed decompositions, the determined candidate approaches the actual ground state. Since this algorithm has been introduced by White [88] in 1992, the density-matrix renormalization group technique has been established as a highly reliable and precise method, which found applications in the Heisenberg model, the Hubbard model for fermions as well as for bosons and quantum chemistry [89].

A frequently used alternative approach is the LMF approximation [42], which replaces the nearest neighbor hopping on the lattice by isolated bosonic degrees of freedom interacting via an effective mean-field coupling with the neighbors. Within this approximation the quantum wave function is described by a direct product of local wave functions, one for each site, which is equivalent to the Gutzwiller variational technique [90–92]. Based on the LMF approximation several numerical techniques, such as SMF theory [46, 47] and LMF theory [43–45], were proposed, which will be discussed in detail in Section 3. The LMF cluster analysis [2], as an advanced mean-field technique, will be introduced in Section 4. The phase diagram of the 2d disordered BH model with random on-site potentials predicted by the LMF cluster analysis, which interprets the BG-SF transition as a percolation of SF regions, agrees precisely with the one obtained from quantum Monte Carlo methods [35]. Moreover, in Reference [93] the percolation criterion has already been applied to their studies on the BH model with random impurities.

Conclusion

We have seen that for decreasing temperature an Bose gas of bosons undergoes a phase transition to a BEC, where the ground state is occupied macroscopically. Such a system confined in a regular optical lattice undergoes a phase transition from a MI to a SF phase. In the disordered system additionally the BG phase occurs in between. In order to detect the three different phases experimentally the phase coherence, the energy gap of particle excitations as well as the compressibility measured with the help of time-of-flight techniques, Bragg spectroscopy [3, 21] and trap squeezing spectroscopy [25, 75], respectively. The BH Hamiltonian describes the behavior of ultracold bosons in optical lattices. It can be derived expanding the field operators in terms of Wannier functions, which have a maximal occupation probability at one specific site and only small overlap with neighboring sites. The BH model has three free parameters, namely on-site energy, tunneling rate and inter-particle interaction. The chemical potential determines the total number of particles. These energy scales compete with each other, leading to phase transitions in the ordered as well as in the disordered BH model. In this chapter we have already given an overview on the phase diagrams of both BH models on the basis of perturbative descriptions.

3 Local and Stochastic mean-field theory

The dimension of the BH model increases dramatically with the system size $M = L^2$ and the number of atoms N . This is why a complete solution of a large system, comparable to experimental setups, is not feasible, due to the demanded resources as memory and computer time. The LMF approximation [42] reduces the full Hilbert space into M Hilbert spaces of a smaller dimension one for each lattice site. Within this approximation the Hamiltonian of the whole quantum systems is decomposed into a sum of quantum Hamiltonians describing individual sites, which couple to each other in a mean-field way. Within this treatment the phase diagram has been determined on the basis of global order parameters [44, 45]. These, however, do not serve a sharp criterion for the detection of the phase transition, as we will see in this chapter. These global order parameters vary smoothly in the vicinity of the phase transition without showing a precise kink. One advanced method is the SMF technique [46, 47], which introduces an innovative approach for the determination of the ground state properties. This method is also based on the LMF approximation, but requires an additional approximation, whose validity will be discussed in this chapter. Within this treatment the global order parameters show a kink at the phase transition and allow to determine a phase diagram of the disordered system, which will also be discussed in this chapter.

3.1 Local mean-field theory

This theory founds on the LMF approximation, where the tunneling part of the Hamiltonian is approximated via

$$\hat{a}_i \hat{a}_j^\dagger \approx \hat{a}_i \langle \hat{a}_j^\dagger \rangle + \hat{a}_j^\dagger \langle \hat{a}_i \rangle - \langle \hat{a}_i \rangle \langle \hat{a}_j^\dagger \rangle, \quad (3.1)$$

where terms of the form $(\hat{a}_i - \langle \hat{a}_i \rangle)(\hat{a}_j^\dagger - \langle \hat{a}_j^\dagger \rangle)$ are neglected [42]. The central quantities are the local SF parameters ψ_i , which are defined as the expectation values of the annihilation operator at the individual site i in the ground state $|\Psi\rangle$ of the system:

$$\psi_i = \langle \Psi | \hat{a}_i | \Psi \rangle. \quad (3.2)$$

Because of the $U(1)$ -symmetry of the Hamiltonian, they can be chosen to be positive and real, which leads to the LMF approximation

$$\hat{a}_i \hat{a}_j^\dagger \approx \psi_j \hat{a}_i + \psi_i \hat{a}_j^\dagger - \psi_i \psi_j. \quad (3.3)$$

In these terms, the Hamiltonian can be decomposed into a sum of diagonal operators,

$$\begin{aligned}\hat{H} &= \sum_i \hat{H}_i, \text{ where} \\ \hat{H}_i &= (\epsilon_i - \mu) \hat{n}_i + \frac{U_i}{2} \hat{n}_i (\hat{n}_i - 1) - J_{ij} \eta_i (\hat{a}_i + \hat{a}_i^\dagger - \psi_i),\end{aligned}\quad (3.4)$$

whose tunneling rate is replaced by an effective local rate $J_{ij} \eta_i$, which depends on the local SF parameter of the neighboring sites $\eta_i := \sum_j A_{ij} \psi_j$, with $A_{ij} = 1$ for i and j being nearest neighbors on a square lattice with periodic boundary conditions and zero otherwise. This approximation reduces the full quantum problem to M quantum sites, which are coupled in a mean-field way with a spatially varying coupling rate $J_{ij} \eta_i$.

As a direct consequence of the decomposition (3.4) of the Hamiltonian, the full quantum states reduces to a direct product of individual single-site wave functions $|\phi_i\rangle$:

$$|\Psi\rangle = \prod_{i=1}^M |\phi_i\rangle. \quad (3.5)$$

This LMF approximations neglects spatial correlations between the sites as well as quantum fluctuations, which is equivalent to other mean-field as for example the Gutzwiller variational method [90–92]. This LMF approximation is less severe in high space dimensions and is exact for infinite dimensions. Already above the upper critical dimension the LMF description reproduces the exact critical behavior of the full quantum system. Even though the critical dimension is unknown for the considered system, it is certainly larger than 4. Consequently, we expect the approximation to be critically inaccurate for 1D systems, but applicable for 2D systems.

In order to compute the phase diagram in LMF theory the coupled set of the self-consistency equations

$$\psi_i = \langle \Psi | \hat{a}_i | \Psi \rangle, \quad i = 1, \dots, M, \quad M = L^2 \quad (3.6)$$

is solved on an $L \times L$ lattice, where the expectation value is evaluated in the ground state of \hat{H}_i , which itself depends on the local SF parameter ψ_i . For the numerical implementation the set (3.6) of equations is solved recursively, starting from a random initial configuration for the local SF parameters ψ_i on the 2D lattice. This involves solving the eigenvalue problem on each site and computing the expectation value of the annihilator in the numerically determined ground state. This is repeated until the SF order parameter

$$\bar{\psi} = \frac{1}{M} \left[\sum_{i=1}^M \psi_i \right]_{\text{av}}, \quad (3.7)$$

which is given by the mean value of the local SF parameters, is determined with an accuracy of 10^{-4} . In the disordered case the results are averaged over 200 different realizations of disorder, indicated by the brackets $[\cdot]_{\text{av}}$. Since we are working in a regime in which the maximum mean particle number per site is less than three, it is sufficient to truncate the basis of the local Hilbert space for each site at $n = 10$. This has been checked

numerically. If we finally solve for the local SF parameters ψ_i , the ground state of the Hamiltonian (3.4) is determined numerically. Now all desired expectation values, like the local particle number $n_i = \langle \hat{a}_i^\dagger \hat{a}_i \rangle$, and finally the compressibility

$$\kappa = \left[\langle \hat{N}^2 \rangle - \langle \hat{N} \rangle^2 \right]_{\text{av}}, \quad (3.8)$$

with $\hat{N} = \sum_i \hat{n}_i$, can be computed directly. Also the probability distribution (PD) of the occurring local SF parameters

$$P(\psi) = \left[\frac{1}{M} \sum_{i=1}^M \delta(\psi - \psi_i) \right]_{\text{av}} \quad (3.9)$$

can be determined. Here again an average over different disorder realizations has to be performed.

In general the different phases in parameter space can be identified on the basis of the SF order parameter $\bar{\psi}$ and the compressibility κ . The MI phase is neither coherent ($\bar{\psi} = 0$) nor compressible ($\kappa = 0$). The SF phase is coherent ($\bar{\psi} > 0$) and compressible ($\kappa > 0$). The BG phase contains features of both, it is not coherent ($\bar{\psi} = 0$), but yet compressible ($\kappa > 0$). Determining the phase diagram in LMF theory on that basis [44, 45], we face the problem that the exact location of the phase transition cannot be determined. This problem and the resulting consequences will be described in Section 3.3.1. They are the starting point for the research presented in this work and the introduction of a different criterion for the phase transitions in Chapter 4.

In LMF theory, as discussed here, the mean value of local SF parameters $\psi_i = \langle \Psi | \hat{a}_i | \Psi \rangle$ is used to identify the transition to the SF phase. On the one hand, if $|\Psi\rangle$ is a Fock state this local expectation value is zero, as these states form an orthonormal basis. On the other hand, if $|\Psi\rangle$ is a coherent state, this expectation value is positive. In this sense the expectation value ψ_i and thus also its mean value $\bar{\psi}$, can be interpreted as a number indicating if the system state $|\Psi\rangle$ shows a significant overlap with coherent states. The meaning of the local SF order parameter in the context of mean-field descriptions and its connection to the Glauber coherent states is discussed in Appendix A in more detail.

3.2 Stochastic mean-field theory

The central idea of SMF theory [46, 47] is to solve a self-consistency equation for the probability distribution $P(\psi)$ directly instead of the set of self-consistency equations (3.6) for each local SF parameter ψ_i . This technique follows the LMF approximation (3.3), but includes an additional approximation. The ground state of the single-site Hamiltonian (3.4) is determined in dependence of two stochastic variables, ϵ and η . The parameter ϵ is drawn from the disorder distribution $p(\epsilon)$ and as a result $\psi = \langle \Psi | \hat{a} | \Psi \rangle$ is a stochastic variable, drawn from the PD $P(\psi)$, which must be determined self-consistently. Since η is the sum of the SF parameters of the neighboring sites, it also is a stochastic variable drawn from a distribution $Q(\eta)$. The problem of computing the ground state of the full quantum

system for all lattice sites simultaneously is thereby replaced by analyzing the ground state $|\Psi(\epsilon, \eta)\rangle$ of the site independent Hamiltonian

$$\hat{H} = (\epsilon - \mu) \hat{n} + \frac{U}{2} \hat{n} (\hat{n} - 1) - J\eta (\hat{a} + \hat{a}^\dagger - \psi) \quad (3.10)$$

as a function of ϵ and η . The PD

$$P(\psi) = \int d\eta Q(\eta) \tilde{P}_\eta(\psi) \quad (3.11)$$

of the local SF parameters depends on the distribution $Q(\eta)$ of the occurring values of η and the distribution $\tilde{P}_\eta(\psi)$ of the local SF parameters for given η . A direct analysis of $\langle \Psi(\epsilon, \eta) | \hat{a} | \Psi(\epsilon, \eta) \rangle$ as a function of ϵ and η yields

$$\tilde{P}_\eta(\psi) = \frac{d}{d\psi} \int d\epsilon p(\epsilon) \Theta(\psi - \langle \Psi(\epsilon, \eta) | \hat{a} | \Psi(\epsilon, \eta) \rangle). \quad (3.12)$$

Since η is the sum of the local SF parameters ψ of the neighboring sites, its distribution is given by

$$Q(\eta) = \int_0^\infty \prod_{i=1}^Z d\psi_i \mathcal{P}_Z(\psi_1, \dots, \psi_Z) \delta\left(\eta - \sum_{i=1}^Z \psi_i\right), \quad (3.13)$$

where $\mathcal{P}_Z(\psi_1, \dots, \psi_Z)$ is the connected PD function of the local SF parameters ψ_1, \dots, ψ_Z of the Z neighboring sites. Assuming that these Z local SF parameters are statistically independent,

$$\mathcal{P}_Z(\psi_1, \dots, \psi_Z) = \prod_{i=1}^Z P(\psi_i), \quad (3.14)$$

equation (3.13) transforms into a convolution

$$Q(\eta) = \int_0^\infty \left(\prod_{i=1}^Z d\psi_i P(\psi_i) \right) \delta\left(\eta - \sum_{i=1}^Z \psi_i\right). \quad (3.15)$$

The Equations (3.11), (3.12) and (3.15) form a set of equations for the determination of the PD $P(\psi)$, which is self-consistent and must be solved recursively. With the PD $P(\psi)$ at hand, the SF order parameter

$$\bar{\psi} = \int d\psi P(\psi) \psi, \quad (3.16)$$

as the mean value of the distribution, as well as the compressibility

$$\kappa = [\langle \hat{N}^2 \rangle - \langle \hat{N} \rangle^2]_{av}, \quad (3.17)$$

with $\hat{N} = \sum_i \hat{n}_i$, can be computed.

The SMF theory follows the LMF approximation (3.3) and demands the additional assumption (3.14), which implies the absence of correlations of the local SF parameters.

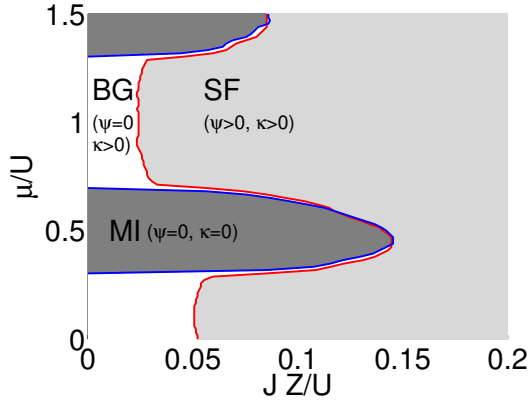


Figure 3.1: SMF phase diagram for fixed disorder strength $\Delta/U = 0.6$ determined by using the SF order parameter $\bar{\psi}$ and the compressibility κ [46, 47]. The red line indicates the critical tunneling rate where the SF order parameter $\bar{\psi}$ becomes non-zero, the blue line the critical tunneling rate JZ/U , where the compressibility κ becomes non-zero.

One expects that this is not justified close to the phase boundaries, where the correlation length even diverges, when the transition is of 2nd order. The validity of this approximation in dependence of the system parameters JZ/U and μ/U will be discussed in Section 3.3.2.

The phase diagram results from the analysis of the SF order parameter $\bar{\psi}$ and the compressibility κ [46, 47]. The MI phase is neither coherent ($\bar{\psi} = 0$) nor compressible ($\kappa = 0$). The SF phase is both coherent ($\bar{\psi} > 0$) and compressible ($\kappa > 0$). The BG phase contains features of both, it is not coherent ($\bar{\psi} = 0$) but yet compressible ($\kappa > 0$). The phase diagram shows Mott-lobes along the μ/U -axis with a round tip and a direct MI-BG transition at its tip. In between there is a BG-SF transition, which in the region of integer chemical potential μ/U is almost independent of the tunneling rate JZ/U . In Section 4.3.2 this phase diagram will be discussed thoroughly and compared with the LMF cluster analysis, which will be introduced in Chapter 4.

3.3 Comparison

In the following we will compare the behavior of global order parameters like the SF order parameter $\bar{\psi}$ and the compressibility κ in the vicinity of the phase transition for the LMF with the corresponding quantities of the SMF technique. We will see that, while the order parameters of the LMF theory do not show a kink, the parameters of the SMF theory do. On this basis it is possible to determine a phase diagram in SMF theory. Since both theories use the LMF approximation (3.3), the difference arise from the additional approximation (3.14) made in SMF theory. We will focus on this approximation and check its validity in dependence of the system parameters. We also find differences in the shape of the PD of the local SF parameter.

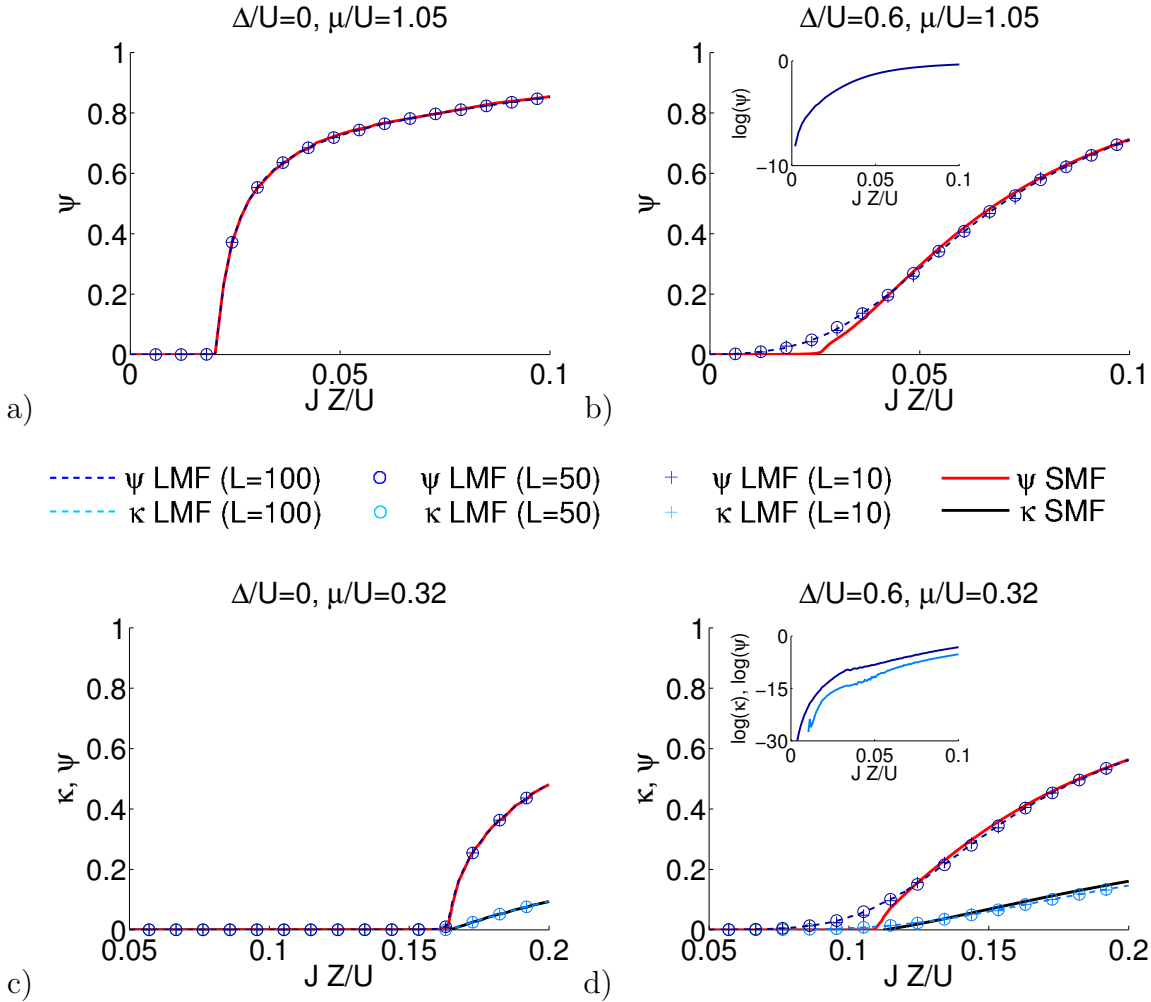


Figure 3.2: Comparison of the LMF and SMF predictions for the average SF order parameter $\bar{\psi}$ and the compressibility κ for fixed chemical potential μ/U as a function of the tunneling rate JZ/U . Homogeneous case ($\Delta/U = 0$) (a, c), disordered case with $\Delta/U = 0.6$ (b, d). Top row is for $\mu/U = 1.05$, where the ordered system displays a MI-SF transition and the disordered system a BG-SF transition ($\kappa > 0$ for all values of JZ/U). Bottom row is for $\mu/U = 0.32$, where the ordered system again displays a MI-SF transition and the disordered system is expected to display the MI, BG and SF phase. For LMF theory the results for a 2D lattice with $L = 100$ (line), $L = 50$ (\circ), $L = 10$ (+) are depicted, which shows that finite-size effects can be neglected.

3.3.1 Superfluid order parameter and compressibility

Since the phase diagram of both, the LMF and the SMF theory, base on the SF order parameter $\bar{\psi}$ and the compressibility κ , we will take a closer look on these important quantities. The behavior of the SF order parameter and the compressibility are shown in Figure 3.2 for the LMF and the SMF theory for comparison.

In the ordered case, shown on the left, the lattice is homogeneous. The SF order parameter $\bar{\psi}$ is zero below and positive above the MI-SF transition. Directly at the phase

transition the SF order parameter shows a plain kink and thus clearly marks the location of the MI-SF phase transition. The compressibility κ shows the same behavior at the phase transition. Moreover, analyzing different lattice sizes L the LMF results show no visible finite-size effects. In this way the phase transition in the ordered case can be determined very precisely. The resulting phase transition agrees perfectly with the perturbative predictions of Equation (2.61).

The situation for the disordered case is shown in Figure 3.2 on the right. The SF order parameter is shown for $\mu/U = 1.05$ and 0.32 as a function of the tunneling rate JZ/U for a disorder strength of $\Delta/U = 0.6$. Here, the behavior of $\bar{\psi}$ as predicted by LMF theory does not indicate a transition at all. It varies smoothly as a function of the tunneling rate JZ/U . This is not a finite-size effect as visible from the graphs for different different system sizes L . The compressibility κ , which indicates the MI-BG transition, also displays the absence of a kink independent of the system size L . While in the ordered case both the SF order parameter $\bar{\psi}$ and the compressibility κ show a kink at the phase transition, in the disordered case they vary smoothly in the region of the phase transitions. Therefore, a precise determination of the phase transition is not possible.

It turns out that the reason for the failure of the average SF order parameter to predict the location of the BG-SF boundary is the following: In the disordered case the value of the local SF parameter varies substantially from site to site due to the variation of the local potential of on-site energies ϵ_i . Close to the phase transition there are sites with zero local SF parameter and others, where the local SF parameter is still positive. This has been interpreted as an overestimation of the phase coherence in LMF description [46]. Our interpretation, however, is different: It is only the average SF order parameter $\bar{\psi}$ that overestimates the phase coherence. In Chapter 4 the LMF cluster analysis is introduced. It will be shown, how a deeper understanding of the mechanisms driving the phase transitions and their location in the phase diagram can be obtained by studying the geometric characteristics of the spatial inhomogeneities of the local particle number \hat{n}_i .

The results of the SMF theory, also shown in Figure 3.2, seem to overcome this problem. The SF order parameter $\bar{\psi}$ (red line) as well as the compressibility κ (black line) show an obvious kink at the phase transition. The SMF theory includes the LMF approximation (3.3) just as the LMF theory and adds the assumption (3.14), that the local SF parameters are uncorrelated. Due to this additional assumption it is doubtful, whether the kink represents the real phase transitions of the BH model or rather is introduced by the restriction (3.14). Therefore, it will be necessary to test this assumption in the next section and finally discuss differences of LMF and SMF theory in Section 3.3.3.

3.3.2 Correlations of the local superfluid parameter

In this section we analyze the assumption (3.14) of statistical independence, which is introduced in SMF theory. Additional to the LMF approximation (3.3) in the tunneling part of the Hamiltonian, SMF theory assumes that the local SF parameters ψ_1, \dots, ψ_Z of the Z neighbors of a chosen site i are uncorrelated and distributed identically, which is introduced by the approximation (3.14). On the basis of LMF calculations we want to test this approximation by comparing $P(\psi_i)P(\psi_j)$, which is the product of the PD

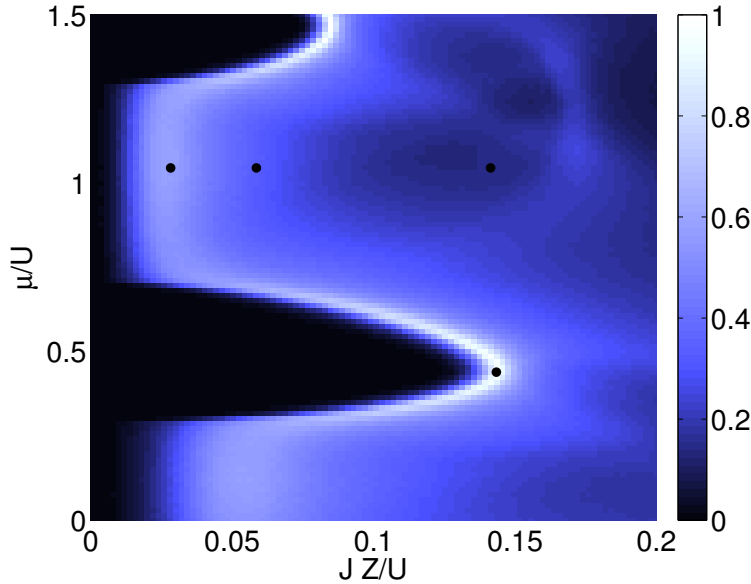


Figure 3.3: The deviation Δ_P between $P(\psi_i)P(\psi_j)$ and $P_Z(\psi_i, \psi_j)$ in dependence of the system parameters JZ/U and μ/U . In the MI regime and for very small tunneling rates the deviations are small, whereas they grow at the phase transitions and in the SF regime. The black dots mark the parameters used in Figure 3.4 along a line at $\mu/U = 1.0455$ and at the tip of the Mott-lobe, where the deviation is maximal.

describing the distribution of the local SF parameter as given in Equation (3.9) with $P_Z(\psi_i, \psi_j)$, which is the PD of pairs (ψ_i, ψ_j) , where i and j are neighboring sites. It represents the probability of having a specific value for the pair (ψ_i, ψ_j) . The distributions $P(\psi_j)$ and $P_Z(\psi_i, \psi_j)$ are computed for every realization of disorder and finally averaged. Both distributions should coincide if the assumption (3.14) is valid.

In Figure 3.3 the integral difference

$$\Delta_P = \int d\psi_i \int d\psi_j |P(\psi_i)P(\psi_j) - P_Z(\psi_i, \psi_j)| \quad (3.18)$$

of both distributions is shown in parameter space. In the MI region, where the $P(\psi)$ has the shape of a delta function at $\psi = 0$ and for very small tunneling rates JZ/U the deviations are small, whereas they are significant in the region of the phase transition and in the SF regime. For illustration both PDs are shown in Figure 3.4 along a line of $\mu/U = 1.0455$ and at the tip of a Mott-lobe, where the deviation Δ_P reaches its maximal value (corresponding to the black dots in Figure 3.3). Additional to the fact that all distributions are symmetric by construction, $P(\psi_i)P(\psi_j)$ shows a rectangular symmetry, which intrinsically follows from the fact that it is a product of the same PD $P(\psi)$. However, the PD $P_Z(\psi_i, \psi_j)$ contains further information of the occurring pairs and shows systematic deviations. Whereas the values on the diagonal are reproduced quite well, the off-diagonal contributions are squeezed to the diagonal. This is especially pronounced in Figure 3.4 j), k), l), which corresponds to the tip of the Mott-lobe. These main differences can be observed for all parameters shown in Figure 3.4 and mainly occur in the regime of

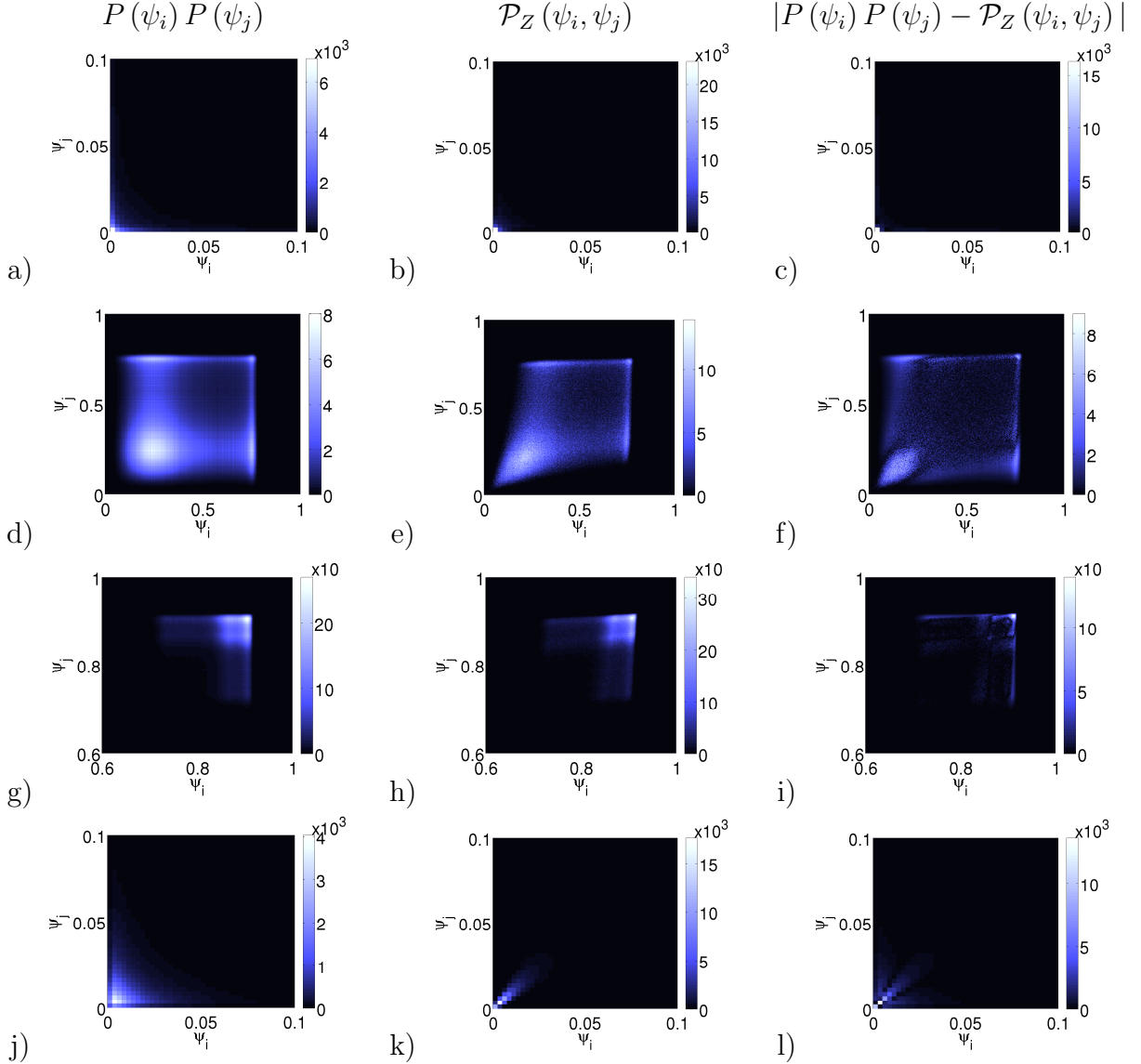


Figure 3.4: The first column shows $P(\psi_i)P(\psi_j)$, the second $\mathcal{P}_Z(\psi_i, \psi_j)$ and the third the deviation $|P(\psi_i)P(\psi_j) - \mathcal{P}_Z(\psi_i, \psi_j)|$ in the disorder case ($\Delta/U = 0.6$). In the first row the parameters are given by $JZ/U = 0.0283$, $\mu/U = 1.0455$ followed by $JZ/U = 0.0586$, $\mu/U = 1.0455$ and $JZ/U = 0.1414$, $\mu/U = 1.0455$ and $JZ/U = 0.1434$, $\mu/U = 0.4394$ in the last row, corresponding the black dots in Figure 3.3. All distributions are symmetric by construction and $P(\psi_i)P(\psi_j)$ shows a rectangular symmetry. The off-diagonal contributions of $\mathcal{P}_Z(\psi_i\psi_j)$ are squeezed to the diagonal leading to pronounced systematic deviations here.

small local SF parameters.

Figure 3.3 illustrates that the assumption (3.14) made in SMF theory, is fulfilled well in the MI regime but does not hold in the region of the phase transition. It is therefore to question, whether this theory reliably predicts the phase transition in this regime.

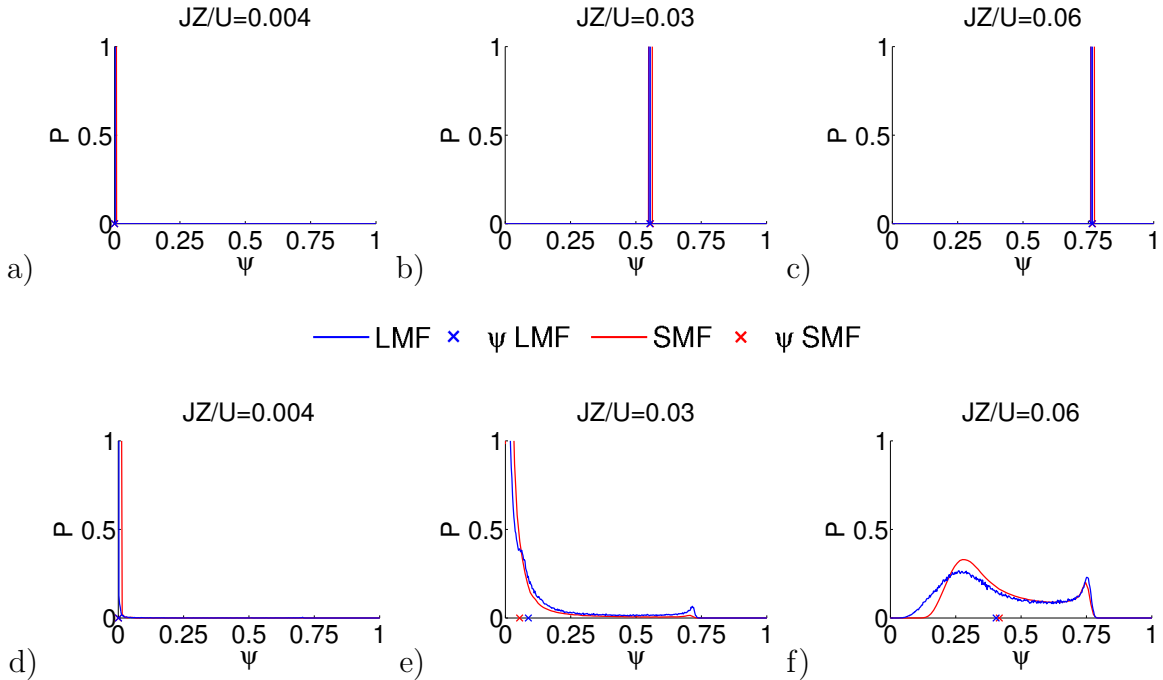


Figure 3.5: PD $P(\psi)$ of the local SF parameter at fixed chemical potential $\mu/U = 1.05$ for different tunneling rates JZ/U as predicted by the LMF (blue) and SMF (red) theory. The ordered case ($\Delta/U = 0$) is shown in the first, the disordered case ($\Delta/U = 0.6$) in the second row. The crosses (\times) at the ψ -axis represent the mean of the PD, which is the SF order parameter $\bar{\psi}$. In the ordered case the PD is a delta function. In the disordered case all local SF parameters are zero in the MI phase. The PD in the BG phase is a superposition of a delta function at $\psi = 0$ and a SF tail. The SF phase is characterized by a broad distribution of positive non-zero local SF parameters.

3.3.3 Probability distribution of the local superfluid parameter

In this section we take a closer look on the PD of the local SF parameter and discuss the occurring deviations of the PD in LMF and SMF theory. Moreover, we will see that it assumes three different characteristics shapes.

In LMF theory for a given realization of disorder at first the self-consistent solution of Equation (3.6) has to be determined. The PDs of each realization are then averaged over 200 different samples of disorder. In SMF theory the PD is the self-consistent result of the set of Equations (3.11), (3.12) and (3.15). Some of the PDs for LMF (blue) and SMF (red) theory are shown in Figure 3.5 for fixed chemical potential $\mu/U = 1.05$ and two different disorder strengths $\Delta/U = 0$ and 0.6.

In the ordered case, depicted in the first row, all local SF parameters are identical, since all sites have the same BH parameters. The averaged order parameter $\bar{\psi}$, depicted as a blue cross, is identical to each local SF parameter ψ_i and the variance of the PD is zero. Therefore, the PD $P(\psi)$ is a delta function at the value $\bar{\psi}$. Here, in the ordered case, we find no deviation between LMF and SMF theory, as we have already described in Section 3.3.1 and as is visible in Figure 3.2.

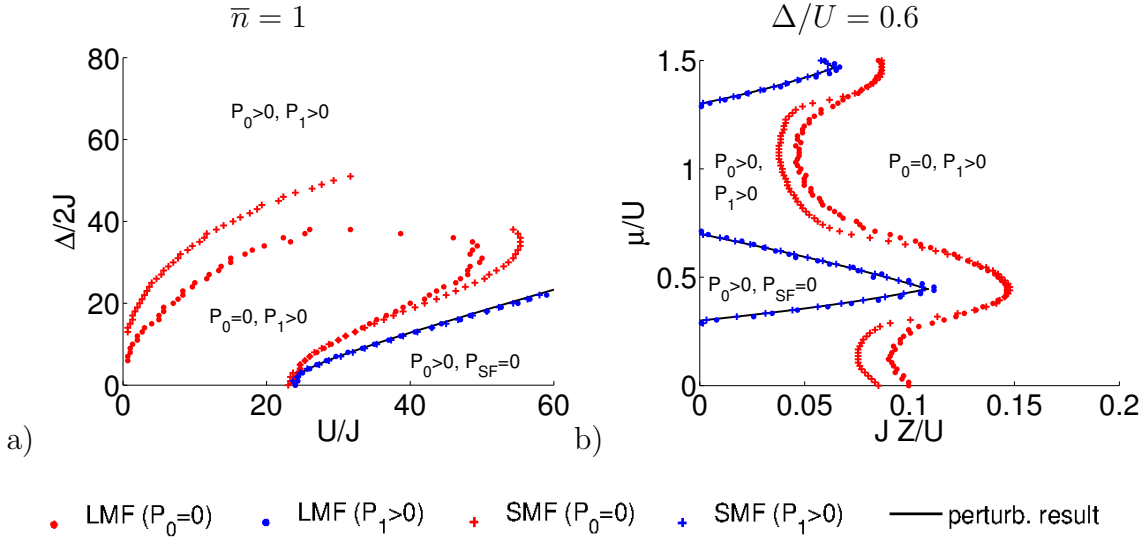


Figure 3.6: Regions of the three characteristic shapes of $P(\psi)$ for fixed density $\bar{n} = 1$ (a) and fixed disorder strength $\Delta/U = 0.6$ (b). The black line represents the MI-BG transition according to the perturbative result given by [48, 49]. In the regions enclosed by the blue line $P(\psi)$ consists only of a delta function at $\psi = 0$. Within the region bounded by the red line in Figure a) and to the right of the red line in Figure b) $P(\psi)$ only has a continuous part $P_{SF}(\psi)$. In other parts of the parameter space the PD is a superposition of a delta function at $\psi = 0$ and $P_{SF}(\psi)$.

This situation changes if disorder is introduced, since then the on-site energy differs from site to site resulting in a variety of different values of the local SF parameter ψ_i . Although, in the MI regime the PD is a sharp delta function at $\psi = 0$ still, it becomes a broad distribution in the BG and SF phase. In the BG phase sites with zero local SF parameter and sites, which have non-zero local SF parameter coexist. Far in the SF regime the PD is a broad distribution representing the variety of positive values for the local SF parameter. In the disordered case the deviations between LMF and SMF theory become apparent. In the disordered case both distribution show roughly the same shape, but especially for small values of ψ , which are crucial for the determination of the phase transition in the BG and SF phase they differ significantly.

Due to its characteristic shape, the PD can be written as a superposition of a delta function at $\psi = 0$ and a broad distribution representing the values $\psi > 0$:

$$P(\psi) = a\delta(\psi) + P_{SF}(\psi) . \quad (3.19)$$

In order to get an overview of the behavior of the PD in parameter space, we identify regions in parameter space, in which the PD assumes one of the three different shapes:

1. The PD is a delta function at zero ψ .
2. The PD is a superposition of a delta function at $\psi = 0$ and the distribution $P_{SF}(\psi)$.
3. The PD is a broad distribution $P_{SF}(\psi)$ and all ψ are positive.

For that purpose we numerically identify two benchmarks of the histograms representing $P(\psi)$. The first one is the value of the histogram at the first bin, P_0 , representing the delta function of $P(\psi)$. The second characteristic point is the value of the histogram at the second bin, P_1 , which is given by $P_1 = P(\psi = \delta_\psi)$ with δ_ψ being the bin size of the histogram representing $P(\psi)$ ($\delta_\psi = 0.0025$ in LMF and $\delta_\psi = 0.015$ in SMF theory).

The regions determined on that basis are shown in Figure 3.6 for fixed density $\bar{n} = 1$ on the left and fixed disorder strength $\Delta/U = 0.6$ on the right. The LMF results are depicted with circles, SMF results with crosses. The blue curves enclose the regions in which $P(\psi)$ is just a delta function at $\psi = 0$ (numerically: $P_0 > 0$ and $P_1 < 10^{-3}$). The red curves delimit the regions, in which the delta function part of $P(\psi)$ vanishes (numerically $P_0 < 10^{-6}$). In the remaining part of the parameter space $P(\psi)$ consists of a superposition of a delta function at $\psi = 0$ and a continuous part $P_{SF}(\psi)$.

Along the blue line, which describes the occurrence of the SF distribution LMF and SMF theory coincide very well. In other words, here the first sites with positive local SF order parameter $\psi_i > 0$ appear. Moreover, this line also perfectly agrees with the perturbative predictions [48, 49] for the MI-BG transition. At the red line deviations are visible. Here the delta function at $\psi = 0$ disappears and the PD is purely given by $P_{SF}(\psi)$. While these deviations are rather small for low disorder strengths and $U/J > 23$, they grow with increasing disorder.

Conclusion

Within LMF approximation (3.3) the full Hamiltonian is decomposed into M quantum systems, one for each lattice site, which are coupled to each other in a mean-field way. We have seen that within this LMF approximation the global order parameters, usually used for the determination of the phase diagram of the ordered as well as the disordered BH model [44, 45], vary smoothly at the phase transition of the disordered system without showing a precise kink. On the contrary, the global order parameters determined with the SMF technique [46, 47] show a precise kink at the phase transition. Since both techniques are based on the LMF approximation, the only difference is an additional approximation introduced in SMF theory, which assumes that the local SF parameters of different sites are uncorrelated. A thorough study of the correlations of the local SF parameters showed that they are indeed uncorrelated within the Mott regime, but maximally correlated at the phase transition. Therefore, it is to doubt whether the SMF technique predicts the correct phase transition. Moreover, a comparison of the PD for pairs of the local SF order parameter with the PD of one single parameter showed grave deviations, confirming the claim that the local SF parameters of different sites actually are correlated.

4 Local mean-field cluster analysis

The local properties of the BG phase are the central topic of this chapter. As we will show, the BG phase is characterized by a finite number of SF sites, which are characterized by the occurrence of local particle fluctuations, within a background of MI sites, without any local particle fluctuations. We will see that this characterization can be used to identify the phase diagram of the disordered BH model by analyzing appearance and growth of clusters of SF sites: In the MI phase the system only consists of MI sites. In the BG phase SF clusters occur, which do not percolate. The SF phase is the region, where at least one SF clusters percolates. We call this treatment LMF cluster analysis [2] and apply it to the LMF ground states of the 2D disordered BH model. The resulting phase diagram excellently agrees with the phase diagram predicted on the basis of quantum Monte Carlo simulations [35] and deviates largely from the one of SMF and other mean-field predictions. We will also discuss the relation of the percolation transition of the SF clusters to the order parameters usually used to determine the phase transitions.

4.1 Percolation

Some of the sites of a 2D lattice with $M = L^2$ sites with index $i = 1, \dots, M$ are occupied with probability p , others are not with probability $(1 - p)$. We may define a mapping of this pattern by

$$G_i = \begin{cases} 1 & \text{if site } i \text{ is occupied,} \\ 0 & \text{otherwise.} \end{cases} \quad (4.1)$$

For increasing p the number of occupied sites increases and at a critical probability p_c a percolating cluster occurs. In other words, at the value p_c we can find a connected region of occupied sites ($G_i = 1$), which connects opposite borders of the system. This critical value p_c systematically depends on the system size L . With the help of finite-size scaling we can extract the limit $L \rightarrow \infty$ from results for different finite system sizes.

Let us now analyze this scaling behavior. The size s of a cluster is given by the number of sites contained in this cluster. The number of clusters of size s is denoted by n_s , which means that the number of sites belonging to clusters of size s is given by $s n_s$. For a cluster of size s we can define the radius R_s of a cluster by [94]

$$R_s^2 = \frac{1}{2} \sum_{i=1}^s \frac{|\vec{r}_i - \vec{r}_j|^2}{s^2}, \quad (4.2)$$

where \vec{r}_i are the coordinates of the cluster sites. Independent of the actual shape of the cluster, this radius is a measure of the average distance between two cluster sites. For

large clusters, $s \rightarrow \infty$, exactly at the percolation ($p = p_c$) the radius scales as

$$R_s \sim s^\rho, \quad (4.3)$$

where $1/\rho$ plays the role of a dimension, which might be natural or fractal. The correlation length [94]

$$\xi^2 = \frac{2 \sum_s R_s^2 s^2 n_s}{\sum_s s^2 n_s} \quad (4.4)$$

is the average distance between two sites belonging to the same cluster. The average squared distance between two sites of the same cluster is $2R_s^2$. A specific site belongs to a cluster of size s with the probability sn_s/M and is then connected to s sites. Therefore, the corresponding average over $2R_s^2$ of the probability s^2n_s/M gives the squared correlation length. At the percolation $p = p_c$ the correlation length diverges as

$$\xi \sim |p - p_c|^{-\nu} \quad (4.5)$$

with the critical exponent $\nu = 4/3$ in 2D systems [94]. The fraction of sites

$$R = p - \sum_s sn_s, \quad (4.6)$$

which belongs to the percolating cluster is given by the number of occupied sites p minus the fraction of sites that does not belong to the percolated cluster. Notice that the sum runs over all finite clusters except the percolating cluster. Approaching the percolation from below ($p \rightarrow p_c$ with $p < p_c$) R goes to zeros. Thus, Equation (4.6) can be transformed into

$$R = \sum_s s (n_s(p_c) - n_s(p)). \quad (4.7)$$

For large s and in the vicinity of the percolation $p \rightarrow p_c$ we assume n_s to behave like [94]

$$n_s(p) \sim s^{-\tau} e^{-cs} \text{ with } c \sim |p - p_c|^{\frac{1}{\sigma}}, \quad (4.8)$$

with the critical exponents τ and σ . Therefore, the fraction of sites, which belong to the percolating cluster, behaves like

$$R \sim \sum_s s^{1-\tau} (1 - e^{-cs}). \quad (4.9)$$

Transforming the sum into an integral, integrating by parts and applying the transformation $z = cs$ leads to

$$R \sim c^{\tau-2} \int dz z^{2-\tau} e^{-z}. \quad (4.10)$$

This integral is the Γ -Function $\Gamma(3 - \tau)$, which is constant. Therefore, we can conclude with Equation (4.8) that the fraction of sites, which belong to the percolating cluster near the percolation $p \rightarrow p_c$ behaves like

$$R(p - p_c) \sim |p - p_c|^\beta, \quad (4.11)$$

with the critical exponent $\beta = (\tau - 2)/\sigma$, which is $5/36$ for two dimensions [94]. Notice that in the vicinity of the percolation $p \rightarrow p_c$, this fraction is independent of the system size L .

Now we want to analyze the dependence of $R(p - p_c, L)$ not only on the distance $p - p_c$ to the critical value p_c , but also on the system size L of the system. According to the scaling hypothesis [94] for large systems ($1/L \rightarrow 0$) and in the vicinity of percolation ($p \rightarrow p_c$) this quantity behaves according to

$$R(p - p_c, L) = L^{-A} F(z), \quad z = L^B (p - p_c), \quad (4.12)$$

where F is a scaling function and A, B are critical exponents, which we will determine in the following.

For large systems, $L \rightarrow \infty$, the fraction $R(p - p_c, L)$ must agree with Equation (4.11), which means in particular that it is independent of L . Thus, in this limit the scaling function F behaves like $F \sim z^{A/B}$ and the L dependency cancels; therefore, we find $\beta = A/B$.

At the percolation, $z = 0$, the largest cluster is of the order of the system size, i.e. $R_s \sim L$. Due to Equation (4.3), the largest cluster contains $L^{1/\rho}$ sites. Therefore, the fraction of the largest cluster is given by $R = L^{1/\rho-d}$ in d dimensions. Thus, we find $A = d - 1/\rho$. With the help of $\nu/\rho = \beta + \gamma$ and $d\nu = \gamma + 2\beta$ [94], we conduct finally

$$R(p - p_c, L) = L^{-\frac{\beta}{\nu}} F\left(L^{\frac{1}{\nu}}(p - p_c)\right). \quad (4.13)$$

The schematic behavior of $R(p - p_c, L)$ is shown in Figure 4.1 a). For a finite system, $L < \infty$, this function shows a smooth variation from zero to one. In the limit $L \rightarrow \infty$ it approaches a function with a kink at the percolation point p_c . Above the critical value p_c , where $p - p_c \gg L^{1/\nu}$, the correlation length ξ is much smaller than the system size L and the finite system behaves like an infinite system. Approaching the critical value p_c , the correlation length ξ increase according to Equation (4.5) until it reaches the order of the system size L , where $|z|$ is on the order of one. At the critical value, where $z = 0$ the correlation length ξ diverges.

Let us now have a closer look at the probability $P_{\text{Perc}}(p - p_c, L)$ that in a given sample of size L and occupation probability p at least one percolating cluster occurs. Its schematic behavior is shown in Figure 4.1 b). In an infinite system this probability is one for all p above, and zero for all p below the critical value p_c . For a finite system we see a smooth variation between zero and one. The slope of this function at the critical point increase with the system size L and the function approaches the shape of the step function in the limit $L \rightarrow \infty$. The scaling behavior for a finite system is given by

$$P_{\text{Perc}}(p - p_c, L) = \Phi\left(L^{\frac{1}{\nu}}(p - p_c)\right), \quad (4.14)$$

where Φ is a scaling function which is universal for the problem. The probability P_{Perc} varies smoothly with p and its shape approaches a step function for increasing system sizes L . Notice that at the percolation ($p \rightarrow p_c$), the probability $P_{\text{Perc}}(p - p_c, L)$ is independent of the system size L . As a consequence all functions for different system sizes L

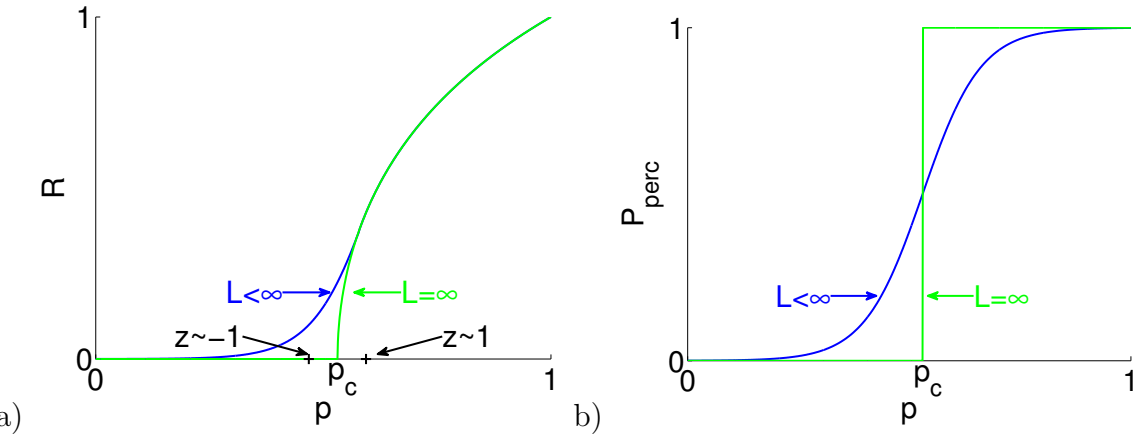


Figure 4.1: The schematic behavior of the fraction $R(p - p_c, L)$ of sites belonging to the percolating cluster (a) and the probability $P_{\text{perc}}(p - p_c, L)$ of having a percolating cluster in the sample (b). For a finite system $R(p - p_c, L)$ varies smoothly from zero to one. In the limit of an infinite system, $L \rightarrow \infty$, this function shows a kink at the percolation point. In a finite system $P_{\text{perc}}(p - p_c, L)$ also varies smoothly from zero to one. Its slope at the percolation point increases with the system size L and the function approaches a step function in the limit of an infinite system, $L \rightarrow \infty$. At the critical point the probability $P_{\text{perc}}(p - p_c, L)$ is independent of the system size L .

intersect at the same point. Within finite-size scaling analysis, Equation (4.14) is used to determine the critical value p_c for the percolation. Suppose we have numerical data for different system sizes L . If we plot P_{perc} versus $z = L^{1/\nu}(p - p_c)$ with the critical exponent $\nu = 4/3$ for two dimensions, the functions coincide for the right value of p_c . We will use this fact in the following, in order to determine the percolation point of the SF clusters of the disordered BH model.

4.2 Criteria for the phase transitions

With the help of the LMF approximation (3.3) it is possible to solve the self-consistency Equation (3.6). As a result, we are able to compute the local SF parameter ψ_i and the local particle number $\langle \hat{n}_i \rangle$ as well as the local particle fluctuations $\kappa_i = \langle \hat{n}_i^2 \rangle - \langle \hat{n}_i \rangle^2$ for each site. In order to determine the phase transitions we first distinguish so called MI sites from SF sites according to their local features. MI sites show the same behavior as sites in the MI phase of the ordered BH model, where tunneling of particle is suppressed leading to vanishing local particle fluctuations κ_i . At SF sites, however, analogously to the sites in the SF phase of the ordered system, tunneling of particles is favorable and the local particle fluctuations κ_i are positive.

Experiments have already reached the regime of single site detection [95, 96], where the local particle number at each site can directly be measured. Before the measurement the system can be described by a full quantum wave function, which in the measurement process is projected onto a product of states of local number eigenstates. By repeating

this process the possible configurations can be explored experimentally in a row of measurements.

As the local particle numbers $\langle \hat{n}_i \rangle$ are the observables in the experiment, we use them as the basis for the identification of MI and SF sites. Sites with an integer local particle number $\langle \hat{n}_i \rangle$ are called MI sites. They in general show vanishing particle fluctuations ($\kappa_i = 0$) and thus exhibit similar features as the sites in the MI phase of the ordered system. Sites with non-integer particle numbers $\langle \hat{n}_i \rangle$ are denoted as SF sites. At these sites tunneling of particles is favorable and local particle fluctuations occur ($\kappa_i > 0$), just as sites in the SF phase of the ordered system. Analogously, we distinguish SF clusters from MI clusters. Formally we map the local particle numbers $\langle \hat{n}_i \rangle$ for each site to a discrete map G_i according to

$$G_i = \begin{cases} 0 & \text{if } \hat{n}_i \text{ is integer (MI site),} \\ 1 & \text{if } \hat{n}_i \text{ is non-integer (SF site).} \end{cases} \quad (4.15)$$

In LMF approximation the BH Hamiltonian decomposes into a sum of local Hamiltonians, according to equation (3.4). As a result the wave function of the full quantum system reduces to a product of single site wave functions as given in equation (3.5). That is why we can determine sites being either SF or MI, individually. In this picture the single site wave functions of individual sites can be a coherent state, while the others are still a Fock state. Notice that the corresponding full quantum wave function is a high dimensional entangled many body quantum state also describing correlations between the sites as well as quantum fluctuations.

For numerical reasons we introduce a threshold γ into the definition of the discrete field G_i . We denote the local particle number $\langle \hat{n}_i \rangle$ as integer if it is inside a range of width 2γ around an inter number,

$$I - \gamma \leq \hat{n}_i \leq I + \gamma, \quad I = 0, 1, 2, \dots, \quad (4.16)$$

where $\gamma = 5 \cdot 10^{-3}$ is chosen to serve as the cut-off in this algorithm. In the whole parameter range, where sites with integer particle number occur, the histogram of the particle number $\langle \hat{n}_i \rangle$ has narrow peaks of width 2γ at integer values. The width decreases when we increase the number of iteration steps to solve the self-consistency Equations (3.6). Therefore, the threshold parameter γ introduced to identify MI sites (and complementarity SF sites) can be reduced by increasing the numerical effort without changing the final results.

In LMF approximation the expectation value of the local particle numbers $\langle \hat{n}_i \rangle$ in the ground state can actually exactly assume integer values. The corresponding full quantum ground state, however, shows non-integer values as it also contains spatial correlations between the sites as well as quantum fluctuations. In order to demonstrate this behavior, we focus on a small system for which the quantum Hamiltonian can easily be diagonalized exactly. For an asymmetric two site system the ground state in LMF approximation is compared with the full quantum state in Appendix B. While in the quantum case the local particles numbers $\langle \hat{n}_i \rangle$ are non-integer for positive tunneling rates $J/U > 0$, in LMF approximation there exists a regime where both local particle numbers $\langle \hat{n}_i \rangle$ are integer. Therefore, the chosen cut-off γ is introduced exclusively for numerical reasons in order to

limit the numerical effort for the recursive determination of the particle number. Please note that this is in contrast to the cut-off used in LMF theory [43–45], described in Section 3.1. In the framework of this theory the global order parameters vary smoothly in the vicinity of the phase transition, independent of the number of iteration steps and the system size as shown in Section 3.3.1. Here a cut-off is necessary to identify the phase transition; it is introduced in order to distinguish positive from zero order parameters. Thus, the resulting phase transition changes dramatically with the actual value of the cut-off.

Notice, that there exist SF sites, which by chance show integer local particle numbers $\langle \hat{n}_i \rangle$, while their local particle fluctuations κ_i still are positive. With the presented mapping (4.15) on the basis of the local particle numbers $\langle \hat{n}_i \rangle$, these occasionally occurring sites are misinterpreted as MI sites, although they behave like a SF. Because of their low number, their influence on the phase diagram can in general be neglected. An exception will be discussed in the context of disorder in the tunneling rates in Section 5.2. In Figure 4.2 typical results for one realization of disorder for $\Delta/U = 0.6$ and $\mu/U = 1.0455$ are shown for three different values of the tunneling rate JZ/U representing the three different phases. In the first column the local SF parameter ψ_i , in the second the particle number per site $\langle \hat{n}_i \rangle$ and in the third the resulting discrete map G_i are shown. In the MI regime all sites are occupied by the same integer number of particles. Here the particle number is one, since we are in the first Mott-lobe. The SF order parameter $\bar{\psi}$ as well as the compressibility κ are zero for this configuration. At the transition from the MI to the BG regime, SF sites ($G_i = 1$) with non-integer particle number occur, where locally particle fluctuation exists. Because of these locally occurring SF sites ($\psi_i > 0$) the SF order parameter $\bar{\psi} > 0$ is small, but not zero in this regime. Since the SF islands are compressible, this phase has positive compressibility $\kappa > 0$. The system consists of a MI background and some SF islands, in which phase coherence is established locally. Different disconnected SF islands do not have a precise phase coherence and as none of them percolates, yet the system does not show long range phase coherence. For increasing tunneling rates JZ/U these SF islands grow in number and size, until one of them finally percolates. With the percolation of a SF cluster long range phase coherence occurs in the system and thus represents the actual transition to the SF regime in parameter space. Just after the percolation the phase of the system is macroscopically coherence, which means that the SF order parameter is positive, $\bar{\psi} > 0$, as well as the compressibility, $\kappa > 0$. On the basis of these results, we will introduce a criterion for the phase transitions.

For each realization of disorder the map G_i is determined as given by Equation (4.15). The SF clusters in the sample are found with the Hoshen-Kopelman algorithm [97] and it is tested, if a percolating cluster exists. The probability P_{Perc} is one if we find such a percolating cluster, connecting two opposite sides of the system, and zero otherwise. Afterwards the results are averaged over 200 ($L = 50, 100$) and 2500 ($L = 10$) realizations of disorder for a fixed value of the tunneling rate JZ/U . The percolation probability P_{Perc} is shown in Figure 4.3 for different system sizes as a function of the tunneling rate JZ/U . Moreover, the finite-size scaling analysis for the percolation transition is depicted. This analysis yields $J_c Z/U = 0.15$ and $J_c Z/U = 0.04$ for fixed $\Delta/U = 0.6$ and $\mu/U = 0.439$ and $\mu/U = 1$ respectively, and a critical exponent of $\nu = 4/3$ in both cases. We find the

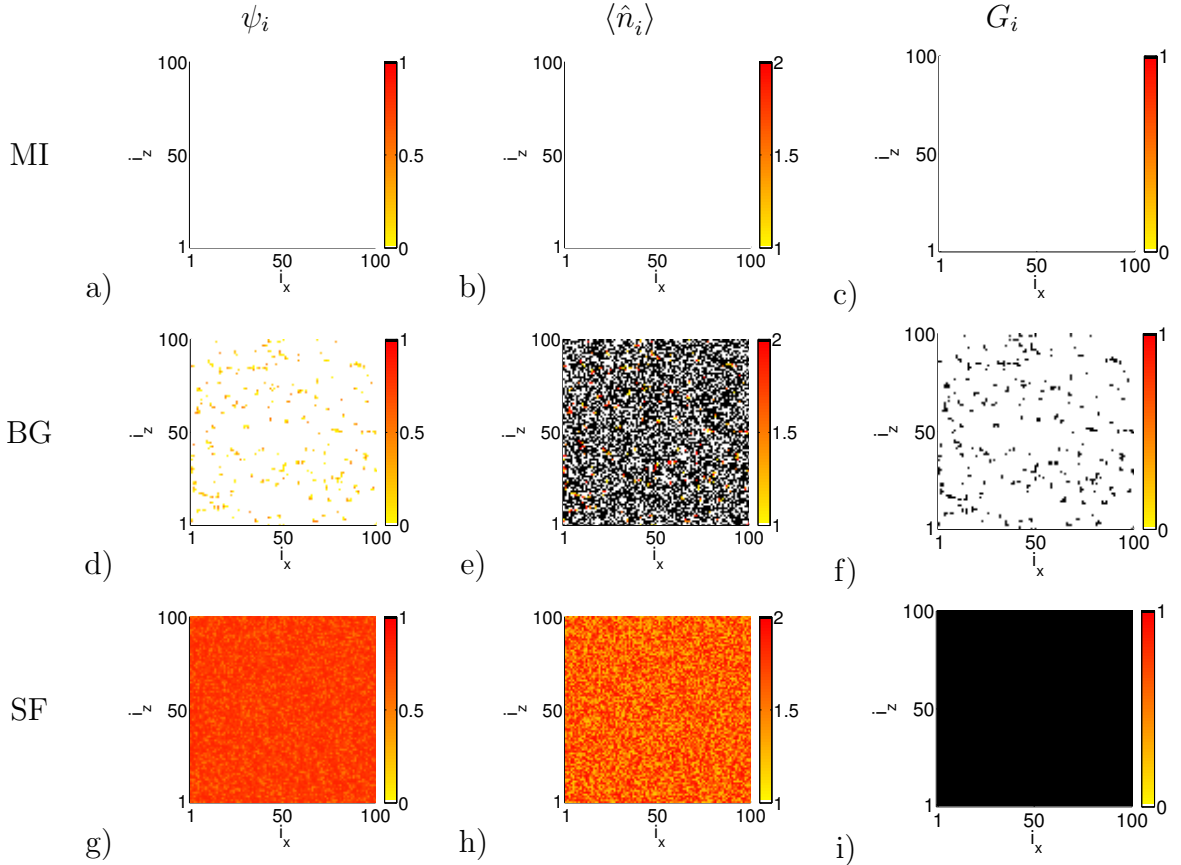


Figure 4.2: Configurations of the local SF parameter ψ_i , the local particle number $\langle \hat{n}_i \rangle$ and the discrete map G_i , given in Equation (4.15), for a single realization of disorder for $\Delta/U = 0.6$. The first row shows an example for a MI ($JZ/U = 0.0242$, $\mu/U = 0.4394$) followed by one for a BG ($JZ/U = 0.0182$, $\mu/U = 1.0455$) and a SF phase ($JZ/U = 0.141$, $\mu/U = 1.0455$). Note that white color marks the minimal value (zero in the left and right, one in the middle column) and black the maximal value (one in the left and right, two in the middle column).

same critical exponent of the percolation transition for all parameters we study. Thus, we may conclude that this transition is in the universality class of conventional 2D percolation [94].

At this point we hypothesize that the BG-SF transition is characterized by the percolation of SF sites. The MI-BG transition, however, is characterized by the appearance of the first SF site. In the MI phase the system contains only MI sites. In the BG phase the system consists of a mixture of MI and not percolating SF sites. Finally, in the SF phase a percolating SF cluster occurs, introducing long range order of the phases of the system. According to that, the criterion for the transitions is given by:

1. The MI-BG transition takes place, where the first SF site occurs in the system.
2. The BG-SF transition is the percolation transition of the SF clusters.

The appearance of the first SF site in a MI background marks the MI-BG transition. The compressibility κ , which is given by the particle fluctuation, is zero in the MI phase

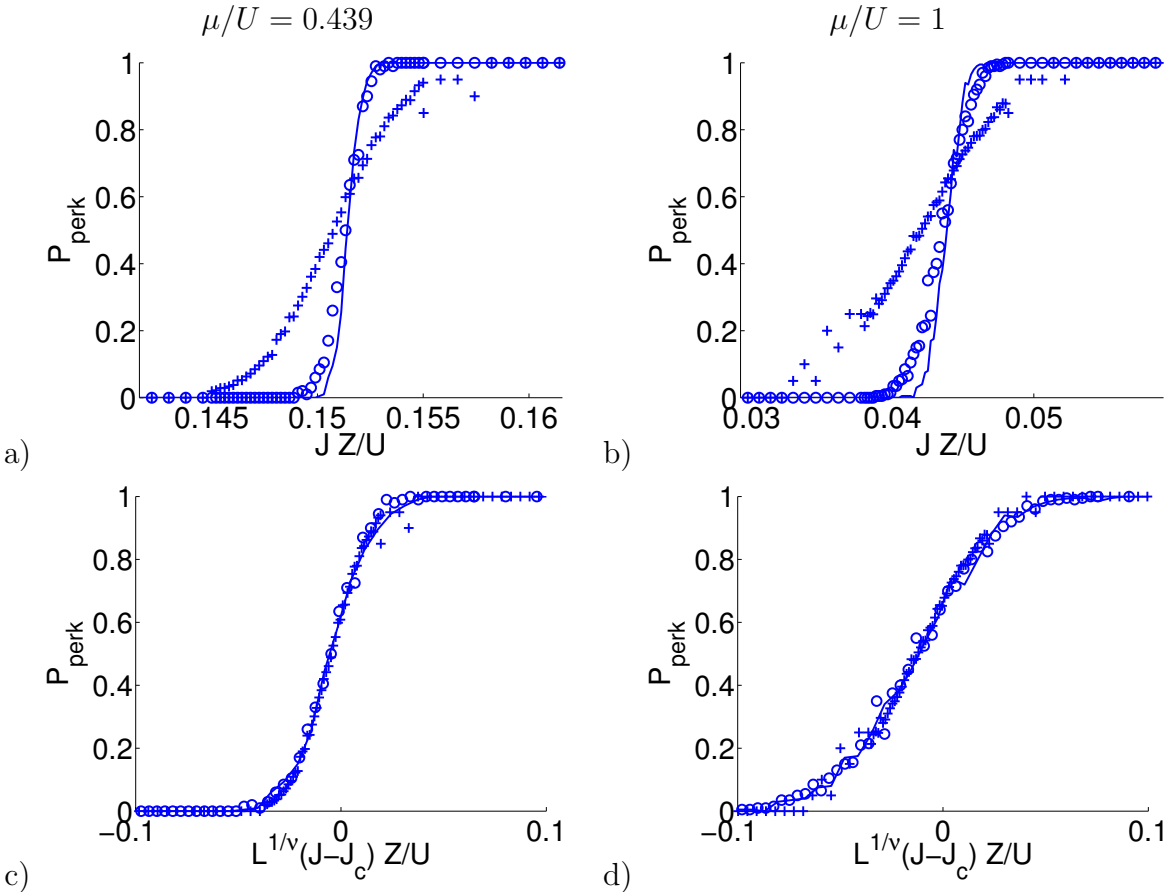


Figure 4.3: The percolation probability P_{Perc} (a), (b) and the finite-size scaling plot (c), (d) for different system sizes $L = 10$ (+), 50 (o), 100 (-). The critical tunneling rates according to the finite-size scaling (4.14) are given by $J_c Z/U = 0.15$ for $\mu/U = 0.439$ on the left and $J_c Z/U = 0.04$ for $\mu/U = 1$ on the right. The critical exponent is $\nu = 4/3$.

and non-zero in the BG and SF phase. Within the MI phase there exists an energy gap $E_g = E_0^N - E_0^{N+1}$ between the ground state energy of N and $N + 1$ particles. This means adding a particle at some site costs the energy E_g [1]. This energy gap suppresses particle fluctuations between sites, leading to a non-compressible ($\kappa = 0$) system. At the transition to the BG phase this energy gap closes locally and particles start to tunnel within these small SF islands. Since within these small islands particles tunnel freely from one site to the other, the system becomes compressible, which is characteristic for the BG phase. Therefore, the MI-BG transition is characterized by the appearance of the first SF sites in a sea of MI sites.

The BG-SF transition is marked by the percolation of SF sites. The SF order parameter is a measure for the coherence of the system, as it is zero if the ground state is not an eigenstate of the annihilator and positive otherwise. The BG phase is characterized by isolated SF clusters within a MI sea. The phases of different isolated clusters are uncorrelated, hence long range order of the phases is lacking and the SF order parameter

is zero, corresponding to the situation as in the MI phase. Because of the Heisenberg uncertainty relation clusters with sharp particle number (MI sites) have fluctuating phases, while clusters with sharp phases (SF sites) have fluctuating particle numbers. Connected clusters of SF sites with fluctuating particle numbers tend to have a fixed phase relation. Therefore, these clusters can be identified with SF regions, although, true superfluidity only exists in the infinite system. Indeed, once these phase ordered clusters percolate, true superfluidity emerges. Moreover, the appearance of the percolating cluster introduces the long range order of the phases and the SF order parameter become positive, describing the coherence of the whole system.

The SF fraction is also used to identify the BG-SF transition, as it is zero in the MI and BG phase and positive in the SF phase. The SF fraction is given by the stiffness of the system under a uniform twist θ on the phases and is given by [44, 98]

$$f_{SF} = \lim_{\theta \rightarrow \infty} \frac{E_\theta - E_0}{NJ\theta^2}, \quad (4.17)$$

where E_θ is the ground state energy of the system with twisted boundary conditions. Such a twist can be introduced by applying a certain twist to the boundary phases in one space direction. In absence of long range order of the phases such a twist at the boundary does not cost energy. This means that, the SF fraction is zero as long as the clusters do not percolate. The application of a phase twist at the system boundaries will only cost a macroscopic amount of energy when the percolating SF cluster appears. The percolating cluster establishes long range order of the phases and thus yields a non-vanishing SF fraction.

The SF density [36, 99]

$$\rho_{SF} = \frac{\langle W^2 \rangle}{2J\beta\rho}, \quad (4.18)$$

where $\beta = 1/(k_B T)$ is the inverse temperature and ρ is the average particle number per site, is proportional to the mean-square of the winding number $\langle W^2 \rangle$ of boson world lines in the path integral representation, which is used in quantum Monte Carlo simulations to identify SF order. An overview on quantum Monte Carlo techniques and the world line picture is given in the Appendix C. When on average a finite fraction of boson world lines wrap around the whole system, the mean-square winding number is positive and the system is SF. To wrap around the whole system, a boson world line, on its way through imaginary time, has to move along a path that traverses the whole system, thus attributing particle number fluctuations to the individual sites of this path. These sites will consequently attain non-integer expectation values for the local particle numbers $\langle \hat{n}_i \rangle$. This means, that there exists at least one percolating SF cluster in the system.

It should be noted that other quantum phase transitions of disordered systems are naturally percolation transitions: The critical point of the random transverse Ising model is governed by an infinite randomness fixed point (in $d \geq 1$ dimensions [100–103]), which signals the percolation of strongly coupled clusters that away from criticality constitute the Griffiths phase [104]. The percolation transition that we observe in our calculations falls into the universality class of a conventional, 2D site percolation, which means it does not carry the signature of the critical properties of the proper BG-SF transition. This is

most probably a consequence of the LMF approximation that we use, since it does not properly account for spatial correlations. If applied to the exact ground state one would expect the critical exponents of the percolation transition to be related to the critical exponents of the BG-SF transition.

4.3 Phase diagrams

We will determine the phase diagram on the basis of the LMF cluster analysis for two common representations, namely for commensurate filling as well as for fixed disorder strength. The BH model with disordered on-site energies drawn from a box distribution as given in equation (2.63), is described by two system parameters J and U , as well as by the disorder strength Δ and the chemical potential μ , which as a Lagrange multiplier fixes the total number of particles. There exist two common representations of the 2D phase diagram: In the first one the mean particle number N/M is fixed to an integer number, which fixes the chemical potential μ . Here it is fixed to one particle per site and the matching chemical potential μ must be determined for each set of parameters individually. Thus, the phase diagram can be presented in dependence of the scaled parameters $\Delta/(2J)$ and U/J . In the second representation the disorder strength Δ is kept fixed and the phase diagram is given in dependence of μ/U and JZ/U . In this representation the well known Mott-lobes occur. In the following we will discuss both representations and compare them to either quantum Monte Carlo simulations [35] and SMF or other mean-field predictions.

4.3.1 Commensurate filling

In this section we determine the phase diagram for commensurate density in dependence of $\Delta/(2J)$ and U/J , for which a prediction on the basis of quantum Monte Carlo simulations is available [35]. The mean particle density $\bar{n} = \sum_{i=1}^M \langle \hat{n}_i \rangle / M = 1$ is fixed with an accuracy of 10^{-4} by adjusting the chemical potential for each set of the system parameters $\Delta/(2J)$ and U/J . Outside of the Mott-lobes this result is unique, whereas inside the MI regime the chemical potential is fixed to the vertical center of the Mott-lobe. In the μ/U versus JZ/U representation, where the Mott-lobes are visible and which we will discuss in Section 4.3.2, the line for $\bar{n} = 1$ always passes the tip of the first Mott-lobe. In the $\Delta/(2J)$ versus U/J parameter space the corresponding line for fixed Δ is a straight line through the origin with slope $\Delta/2U$.

For the right chemical potential that fixes the density \bar{n} to one, we compute the ground state of the LMF Hamiltonian (3.4), the local particle number $\langle \hat{n}_i \rangle$ and determine the discretized map G_i (4.15), which is used to identify the MI, BG and SF phase on the basis of LMF cluster analysis [2]. The resulting phase diagram is shown in Figure 4.4 a). As expected [20, 35] the SF region is completely surrounded by the BG phase (except at $\Delta/(2J) = 0$). Its boundary has some characteristic features: It extends in a slight bump up to quite large disorder strength of up to $\Delta/(2J) \sim 75$ and in a pronounced

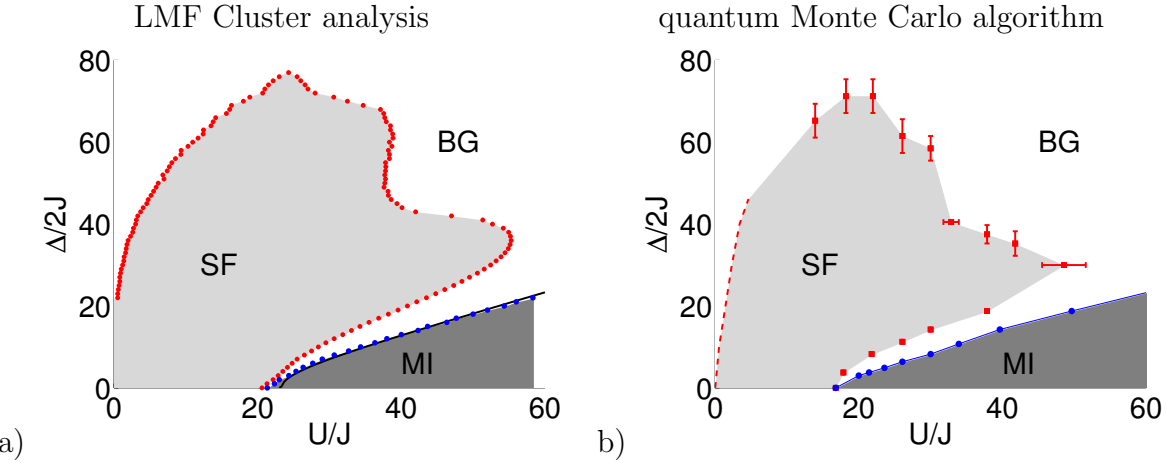


Figure 4.4: Comparison of LMF cluster analysis phase diagram (a) and quantum Monte Carlo phase diagram (b) for fixed mean particle number $\bar{n} = 1$. In the LMF cluster analysis phase diagram (a) the percolation transition of the SF sites occurs at the red line, which indicates the BG-SF phase boundary. The blue line marks the boundary of the MI region, in which all sites are MI sites. The black line indicates the MI-BG transition according to perturbative results [48, 49]. On the right the prediction for the phase diagram for fixed mean particle number $\bar{n} = 1$ based on the results of quantum Monte Carlo simulations is shown (data taken from [35]).

nose up to the inter-particle interaction of $U/J \sim 52$. Here in this region we find a re-entrance behavior. Starting in the MI regime and going along a line of fixed inter-particle interaction U/J , we enter the BG region for increasing disorder strength $\Delta/(2J)$. For larger values of $\Delta/(2J)$ the system is in the SF phase, while for even higher $\Delta/(2J)$ it re-enters the BG phase. Weak disorder thus supports superfluidity in the BH model, as has already been observed in [28, 35, 36, 105].

Most remarkably, our prediction on the basis of the LMF cluster analysis agrees very well with the results of quantum Monte Carlo simulations [35] shown for comparison in Figure 4.4 b). Further details on quantum Monte Carlo simulations are given in the Appendix C. The shape of the BG-SF phase boundary with its characteristic nose and bumps clearly coincide, but also the quantitative agreement is very good, regarding the substantial error bars of the quantum Monte Carlo data in the large disorder and large interaction regime. The quantum Monte Carlo method estimate for the extreme value of $\Delta/(2J)$ in the bump is $\Delta/(2J) \sim 72 \pm 4$ and of inter-particle interaction in the nose $U/J = 49 \pm 3$, see Figure 2 in [35]. Moreover, with our method we could also explore the region of weak inter-particle interaction, which is hardly accessible by quantum Monte Carlo methods and we found a singular behavior and a steep rise of $\Delta/(2J)$ with $U/J \rightarrow 0$, which is compatible with the analytically predicted behavior $\Delta/(2J) \propto \sqrt{U/J}$ [106]. Note that, $\Delta/(2J)$ rises steeply for $U/J \rightarrow 0$ and in order to obtain data for $\Delta/(2J) < 20$, it would be necessary to compute the ground state of even larger systems sizes. Finally, we conclude that the percolation criterion, that we introduced in Section 4.2 to locate the SF-BG transition, produces remarkably accurate predictions.

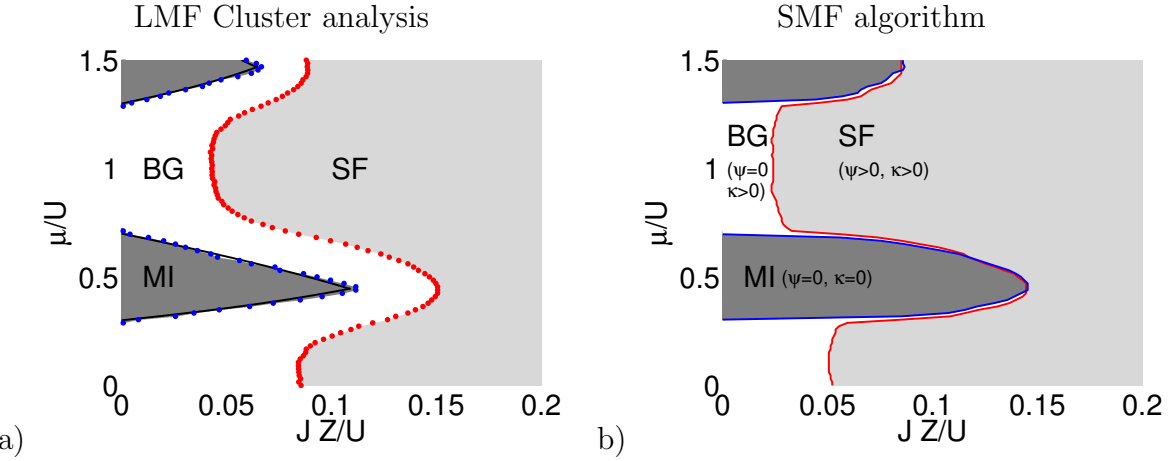


Figure 4.5: Comparison of LMF cluster analysis phase diagram (a) and SMF phase diagram (b) for fixed disorder strength $\Delta/U = 0.6$. The percolation transition of the SF sites occurs at the red line, which indicates the BG-SF phase boundary. The blue line marks the boundary of the MI region, in which all sites are MI sites. The black line is the MI-BG transition according to the perturbative result given by 2.61. The SMF phase diagram on the right is determined by using the SF order parameter $\bar{\psi}$ and the compressibility κ as described in [46, 47]. The red line indicates the critical tunneling rate JZ/U where the SF order parameter $\bar{\psi}$ becomes non-zero, the blue line the critical tunneling rate JZ/U , where the compressibility κ becomes non-zero.

Our result for the MI-BG transition line, which denotes the appearance of SF sites with non-integer local particle numbers $\langle \hat{n}_i \rangle$, agrees well with the perturbative result [48, 49], shown in Figure 4.4 a). Moreover, they agree with the line $\Delta = E_{g/2}$ obtained using the gap data from [34], shown in Figure 4.4 b).

4.3.2 Fixed disorder strength

After we have seen in the last section that our method to determine the phase diagram of the 2D disordered BH model leads to results that agree very well with quantum Monte Carlo predictions, in this section we determine the phase diagram for fixed disorder strength $\Delta/U = 0.6$ as a function of the chemical potential μ/U and the tunneling rate JZ/U and compare it with predictions of SMF theory. In this phase diagram the Mott-lobes occur and the line given by $\bar{n} = 1$ always passes the tip of the first one.

In Section 3.2 we introduced the SMF theory and emphasized that the SMF theory bases on the same LMF approximation (3.3) as LMF theory, but it involves the additional approximation (3.14) of the distribution $P_Z(\psi_1, \dots, \psi_Z)$, by assuming that the local SF parameters ψ_i are independent of each other. The validity of this restriction fails close to the phase transitions as was shown in Section 3.3.2. Despite or perhaps because of this approximation the SF order parameter $\bar{\psi}$ as well as the compressibility κ computed within SMF theory are exactly zero in specific regions of the parameter space (see Figure 3.2), which one might want to identify with MI and BG phase, as done in [46, 47].

	MI-BG		BG-SF		Δ/U
	JZ/U	μ/U	JZ/U	μ/U	
single site LMF [107]	0.155	0.5091			0.5
multi site LMF [107]	0.17	0.4364			0.5
LMF cluster analysis [2]	0.1115	0.4644	0.1509	0.4434	0.6
quantum Monte Carlo results [35]	0.124	(0.4561)	0.2012	0.4082	0.6
strong-coupling expansion [49]	0.1253	0.4345			0.6
SMF [46]	0.1433	0.5	0.1433	0.5	0.6
Gutzwiller variational techniques [90]	0.2748	0.3684	0.2748	0.3684	0.6
LMF cluster analysis [2]			0.0942	0.4868	1
quantum Monte Carlo results [35]			0.1047	0.4846	1
LMF cluster analysis [2]			0.0934	0.5043	2
quantum Monte Carlo results [35]			0.1062	0.4950	2

Table 4.1: Comparison of the parameters at the tip of the first Mott-lobe (MI-BG transition) and the BG-SF transition at the chemical potential μ/U which satisfies $\bar{n} = 1$. The MI-BG predictions of [35] were not obtained by quantum Monte Carlo of the disordered BH model, but are based on gap data for the ordered BH model [34] and given in brackets here. Methods predicting tapered Mott-lobes as the quantum Monte Carlo method and LMF cluster analysis, are shown with grey background. The others predict round Mott-lobes, like the mean-field techniques based on global order parameters.

The LMF cluster analysis and SMF [46, 47] phase diagrams for fixed disorder strength $\Delta/U = 0.6$ are shown in Figure 4.5. One immediately observes substantial differences: Firstly, in LMF theory the BG phase always separates the MI from the SF phase. The intervening BG phase is actually predicted to be quite large even at the tip of the Mott-lobes. However, SMF theory predicts a direct MI-SF transition, in contradiction to the theorem of inclusion [20], which states that the MI and the SF phase of the BM model with uncorrelated disorder are always separated by the BG phase. Secondly, large differences in the critical tunneling rate of the BG-SF transition occur, especially in the region around $\mu/U = 1$. Assume we fix the chemical potential there. In this case the SMF theory predicts the phase transition at $JZ/U = 0.0241$. However, the percolation of the SF cluster takes place at $JZ/U = 0.0430$. Thus, significant changes of the system in this case occur for values of the tunneling rate twice as large as predicted by $\bar{\psi}$ in SMF theory. A direct comparison of the LMF results with quantum Monte Carlo data from [35] is not possible here, since the latter is obtained for the canonical ensemble, where the chemical potential is fixed by the constraint $\bar{n} = 1$ and thus absent as a free variable. However, we can take our LMF estimate for the value of μ that fixes the particle density at $\bar{n} = 1$ for fixed U/J and $\Delta/(2J)$ to obtain an approximate comparison. This data is collected in Table 4.1, where we also show the prediction of other works. For the MI-BG transition there exist only small deviations of the quantum Monte Carlo [35] and strong-coupling [49] predictions from our LMF cluster analysis results at the tip of the Mott-lobe. For the BG-SF transition one observes deviations of the quantum Monte Carlo predictions from

our LMF cluster analysis results, but a good agreement for stronger disorder, $\Delta/U \geq 1$. We also note that the tapered shape of the Mott-lobe predicted by the strong-coupling expansion [49] agrees well with our result of the LMF cluster analysis shown in Figure 4.5. The LMF theory has been used in [43, 44] to solve the self-consistency Equations (3.2) and to calculate a LMF expression for the compressibility κ , given in Equation (3.8), and the SF fraction f_s , given in Equation (4.17). On the basis of these two observables the phase diagram as a function of μ/U and JZ/U is determined in [43, 44], which displayed a round shape of the Mott-lobes, a direct MI-SF transition for small disorder strengths Δ/U and an intervening BG phase at larger disorder strengths Δ/U . With this procedure one faces the problem, that the order parameters smoothly pass the phase transition instead of showing a precise kink, as discussed in Section 3.3.1. It is important to notice that although the starting point of the calculation in [43, 44] is the LMF approximation, which is identical to our, the usage of a different criterion to identify the phases leads to a phase diagram that differs significantly from the one predicted by our LMF cluster analysis [2]. Note that the SMF theory, as described in Section 3.2, predicts a direct MI-SF transition along the lower border of the SF region in the parameter range shown in Figure 4 in [46]. The characteristic BG region for small disorder strength Δ/U is absent in this parameter range, which is in contradiction to the theorem of inclusion, proven in [20], which excludes a direct MI-SF transition in any uncorrelated disordered systems. The tip of the Mott-lobe in SMF theory lies above the values predicted by the LMF cluster analysis [2], the quantum Monte Carlo technique [35] and the strong-coupling expansion [49] (see Table 4.1).

A multi site LMF theory is introduced in [107], where every plaque of two by two sites is treated quantum, which keeps the spatial correlation therein. Instead of single sites these plaques are coupled in a LMF way, analogously to the treatment described in Section 3.1. The Mott-lobe for $\Delta/U = 0.5$ is determined for both, the single site and multi site LMF theory, on the basis of the condensate fraction, which is the largest eigenvalue of the one-body density matrix. The Mott-lobe shows a round shape at the tip, which is in agreement with LMF predictions on the basis of the global order parameters [44] and SMF theory [46, 47]. The multi site LMF theory predicts a larger MI region than the single site LMF theory. In both cases the tip of the Mott-lobe is predicted for larger tunneling rates JZ/U as for the LMF cluster analysis [2], the quantum Monte Carlo technique [35] or the strong-coupling expansion [49] at $\Delta/U = 0.6$ (see Table 4.1). This is in contradiction with the fact, that the Mott-lobes shrink with increasing disorder strength. Note that the condensate fraction in [107] smoothly approaches zero, analogous to our observations on the SF order parameter $\bar{\psi}$ and the compressibility κ made in Section 3.3.1 and a linear fit is used to determine the transition point.

The so-called Gutzwiller projected variational technique is introduced in order to determine a canonical transformation of the quantum Hamiltonian, which requires the truncation of the hopping term [90–92]. Thus, it is possible to minimize the expectation value of the transformed Hamiltonian in Gutzwiller type LMF states with respect to its variational parameters. Finally, the SF stiffness and the compressibility yield a phase diagram, which shows a remarkably narrow BG region between the MI and the SF phase. The tip of the Mott-lobe here is predicted for larger value of the tunneling rate JZ/U and smaller values

of the chemical potential μ/U and differs from the predictions of LMF cluster analysis [2], quantum Monte Carlo technique [35] and strong-coupling expansion [49] (see Table 4.1). In all mean-field calculations (LMF theory [43, 44], SMF theory [46, 47], multi site LMF technique [107] and Gutzwiller variational technique [90]) mentioned here, we see characteristic deviations from the LMF cluster analysis [2], the quantum Monte Carlo technique [35] and the strong-coupling expansion [49]. The tip of the Mott-lobe of mean-field techniques is predicted for far higher values of the tunneling rate as listed in Table 4.1. Moreover, the shape of the Mott-lobes obtained from mean-field techniques is round at the tip, in contrast to a tapered shape in LMF cluster analysis [2], quantum Monte Carlo technique [35] and strong-coupling expansion [49].

Conclusion

We characterized the three occurring phases on the basis of local properties. In the MI phase the system consists exclusively of MI sites with zero local particle fluctuations. The BG phase is characterized by a mixture of MI sites and non percolating SF sites, where local particle fluctuations occur, while in the SF phase at least one SF cluster percolates. With this picture in mind, we have introduced a new criterion to identify the three different phases of the disordered BH model on the basis of the whole set of local particle numbers $\{\hat{n}_i\}$. The resulting phase diagram of this LMF cluster analysis for a fixed commensurate density $\bar{n} = 1$, shown in Figure 4.4, is in excellent agreement with the prediction of quantum Monte Carlo simulations [35], not only qualitatively, but also quantitatively within the numerical error bars. This is remarkably, since other LMF approaches using averaged quantities fail to identify the BG-SF transition, since the used indicator varies smoothly at the expected phase transition as discussed in Section 3.3.1. Therefore, the LMF cluster analysis can serve as a reliable tool to localize the transitions. Moreover, it provides an intuitive picture and a deeper understanding of the underlying physics of the BG-SF phase transitions in terms of SF islands their percolation at the phase transition.

5 Boxed uncorrelated disorder

In the following we will discuss the effect of uncorrelated disorder in each of the BH parameters ϵ_i , J_{ij} and U_i separately. With the help of the LMF cluster analysis [2, 4] we will determine, the phase diagram for a uniform distribution

$$p(\alpha) = \frac{1}{\Delta_\alpha} \Theta\left(\frac{\Delta_\alpha}{2} - |\alpha|\right) \quad (5.1)$$

for each BH parameter $\alpha = \epsilon_i, J_{ij}, U_i$ individually, while the other parameters are treated as sharp values. We will find all three phases in each of the disorder scenarios, however we will recognize substantial characteristic differences in the respective phase diagrams. Currently theoretical works mostly deal with uncorrelated disorder only with distributions of the on-site energies [2, 20, 29, 34–36, 44, 46, 49]. Studies on the effect of disordered tunneling rates are only limited to bimodal distributions, where only two different values are distributed randomly over the lattice sites [32, 47, 50, 51]. We, however, will discuss uncorrelated tunneling disorder according to a uniform distribution. Moreover, we will also discuss disorder in the inter-particle interaction, which can be realized experimentally in the vicinity of a Feshbach resonance [52, 54]. We will see the inter-particle interaction is the only BH parameter, for which isolated disorder can be realized in an experiment independent of the other parameters determined by the optical lattice. For a detailed understanding of the BH model, which is especially important for the correct interpretation of experimental data in comparison to theoretical results, the specific influences of disorder in the different BH parameters on the phase transition must be considered. Therefore, with the results of this chapter we will be prepared to study a quasi-random potential, which is widely used in experiments on disordered bosonic systems.

5.1 Disorder in the on-site energy ϵ

The most common disorder scenario is diagonal disorder introduced by site-dependent local on-site energies ϵ_i , which are drawn from a box distribution

$$p(\epsilon_i) = \frac{1}{\Delta_\epsilon} \Theta\left(\frac{\Delta_\epsilon}{2} - |\epsilon_i|\right), \quad (5.2)$$

where Δ_ϵ is the disorder strength. This system has been widely studied via quantum Monte-Carlo methods [29, 34–36], mean-field techniques [2, 44, 46] as well as analytic approaches [20, 49].

Figure 5.1 shows the phase diagram for increasing disorder strengths Δ_ϵ/U resulting from

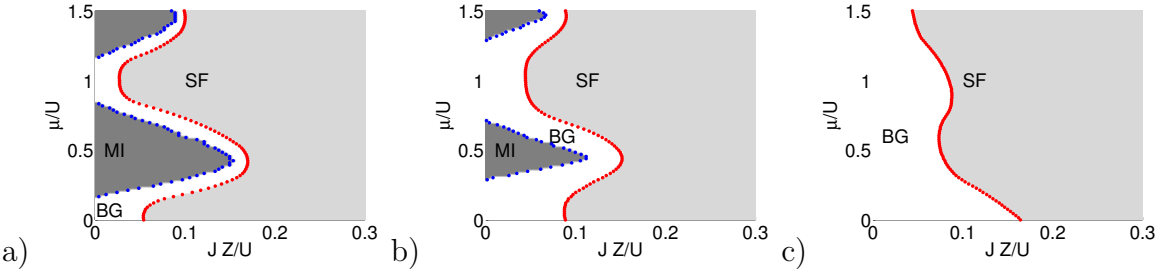


Figure 5.1: Phase diagram for box distributed disordered on-site energies ϵ_i with the disorder strengths $\Delta_\epsilon/U = 0.35, 0.6, 1.5$. There exist an infinite number of Mott-lobes, which disappear at the same critical disorder strength $\Delta_\epsilon^c/U = 1$. They are surrounded by a connected BG region and a SF region for even higher values of the tunneling rate JZ/U .

the LMF cluster analysis [2], as introduced in Chapter 4. The Mott-lobes with a fixed particle number $n = 1, 2, \dots$ per site reach from [1]

$$\mu_- = (n - 1)U + \frac{\Delta_\epsilon}{2} \quad \text{to} \quad \mu_+ = nU - \frac{\Delta_\epsilon}{2} \quad (5.3)$$

along the μ/U -axis and have a distance of Δ_ϵ/U from each other. As a result, there exist an infinite number of Mott-lobes, which all simultaneously disappear at the same critical disorder strength of $\Delta_\epsilon^c/U = 1$. At the tip the Mott-lobes have a tapered shape and coincide with the perturbative result [49], which is shown in blue in Figure 2.10. The Mott-lobes are surrounded by one connected BG region. For larger tunneling rates the phase transition to the SF regime occurs. While all three phases appear for $\Delta_\epsilon^c/U < 1$, in the strong disorder limit only the BG in the small tunneling and the SF phase in the high tunneling regime survive.

5.2 Disorder in the tunneling rate J

The influence of disordered tunneling rates was mainly studied for bimodal distributions, where two values of the tunneling rate are chosen and distributed randomly among the lattice sites [32, 47, 50, 51]. In contrast, here we focus on a general approach, where the local tunneling rates are uniformly distributed according to

$$p(J_{ij}) = J + \frac{1}{\Delta_J} \Theta \left(\frac{\Delta_J}{2} - |J_{ij}| \right), \quad (5.4)$$

where Δ_J is the disorder strength and the distribution is symmetric around a given value of the tunneling rate J .

In Figure 5.2 the phase diagrams resulting from LMF-Cluster-Analysis [2] in dependence of the chemical potential μ/U and the mean tunneling rate JZ/U are shown. It is important to notice that here the width of the disorder distribution Δ_J is the disorder strength and is one order of magnitude smaller than for on-site disorder Δ_ϵ . Here two new unique features occur in the phase diagram [4]:

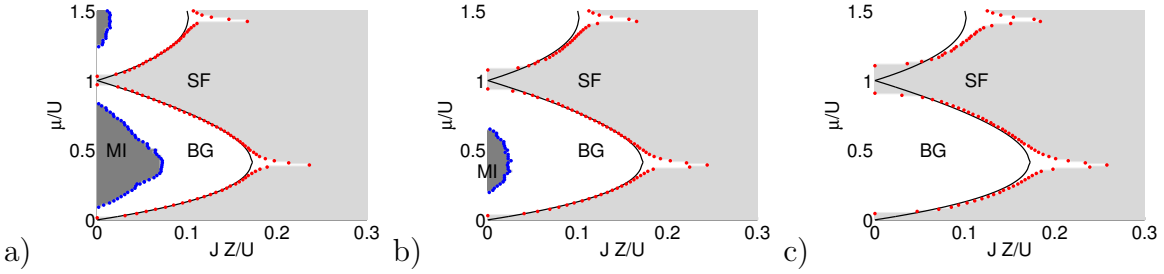


Figure 5.2: Phase diagram for box distributed disordered tunneling rates J_{ij} with the disorder strengths $\Delta_J/U = 0.035, 0.06, 0.095$. The number of Mott-lobes is finite and for increasing tunneling rate JZ/U they disappear one after the other. They are enclosed by individual BG regions, which are separated by one connected SF region, which exist for arbitrary small tunneling rates in the vicinity of integer chemical potential μ/U .

1. The BG regions are separated into individual regions by SF regions reaching down to small tunneling rates, $JZ/U \rightarrow 0$.
2. The distance between the Mott-lobes increases with their number n and the number of Mott-lobes is finite.

For an intuitive explanation, we recall the perturbative result of the ordered case, given in Equation (2.61), which is the limiting result for vanishing disorder strength $\Delta_J \rightarrow 0$. For a small but non-zero disorder strength Δ_J , the first SF regions in the lattice occur at sites with $J + \Delta_J/2$. Therefore, the MI regions are smaller than in the ordered case, where the relevant tunneling rate is J . In comparison to the ordered case the MI border is shifted to the left by $\Delta_J/2$. In the ordered case the JZ/U -coordinate of the tip of the Mott-lobes approaches the μ/U -axis asymptotically in the limit $n \rightarrow \infty$, leading to an infinite number of Mott-lobes. Thus, for a tunneling disorder strength Δ_J all shifted Mott-lobes with an extension smaller than $\Delta_J/2$ do not exist, since instead the system is already in the BG phase, as SF sites occur.

Let us now discuss the behavior of the transition thoroughly [4]: Along the μ/U -axis ($JZ/U = 0$) the Mott-lobes exist between

$$\begin{aligned} \mu_{\pm} \left(\frac{\Delta_J}{2}, Z, U, n \right) &= -\frac{1}{2} \left(\frac{\Delta_J Z}{2} - U(2n-1) \right) \\ &\pm \sqrt{\frac{1}{4} \left(\frac{\Delta_J Z}{2} - U \right)^2 - \frac{\Delta_J Z}{2} Un}, \end{aligned} \quad (5.5)$$

according to Equation (2.61). For fixed disorder strength Δ_J the height of the Mott-lobes is given by

$$\Delta_{\mu}^{\text{MI}} = 2 \sqrt{\frac{1}{4} \left(\frac{\Delta_J Z}{2U} - 1 \right)^2 - \frac{\Delta_J Z}{2U} n}, \quad (5.6)$$

which decreases with n . The height of the Mott-lobes becomes zero at a critical number

$$n_c^{\text{MI}} = \frac{1}{2} \left(\frac{\Delta_J Z}{2U} - 1 \right)^2 \frac{U}{\Delta_J Z}, \quad (5.7)$$

which means that only a finite number n_c^{MI} of Mott-lobes exist. As a consequence, the Mott-lobes disappear one after the other for increasing disorder strength Δ_J/U . The last Mott-lobe ($n = 1$) disappears at

$$\frac{\Delta_J}{U} = \frac{3 - 2\sqrt{2}}{2} \approx 0.0858. \quad (5.8)$$

This is different from the on-site disorder case, where all Mott-lobes vanish at the same critical disorder strength $\Delta_e^c/U = 1$. For a disorder strength of $\Delta_J/U = 0.035$, shown in Figure 5.2 a), three Mott-lobes exist, two of which are visible, while in Figure b) for a disorder strength of $\Delta_J/U = 0.06$ only one remains. In the last diagram for $\Delta_J/U = 0.095$ no Mott-lobe exists, as the critical disorder strength is exceeded.

The Mott-lobes are surrounded by the BG phase. As a new feature in comparison to the on-site disorder case, we find disconnected BG regions between

$$\begin{aligned} \mu_{\pm} \left(\frac{\Delta_J}{2}, Z = 1, U, n \right) &= -\frac{1}{2} \left(\frac{\Delta_J}{2} - U(2n-1) \right) \\ &\pm \sqrt{\frac{1}{4} \left(\frac{\Delta_J}{2} - U \right)^2 - \frac{\Delta_J}{2} Un}, \end{aligned} \quad (5.9)$$

which are separated from each other by the SF region in the vicinity of integer values of the chemical potential μ/U . The fact that the SF region survives in the limit $JZ/U \rightarrow 0$, is a unique feature of tunneling disorder. The height of the BG regions along the μ/U -axis is given by

$$\Delta_{\mu}^{\text{BG}} = 2 \sqrt{\frac{1}{4} \left(\frac{\Delta_J}{2U} - 1 \right)^2 - \frac{\Delta_J}{2U} n}, \quad (5.10)$$

which also decreases for growing n . The number of BG regions is given by

$$n_c^{\text{BG}} = \frac{1}{2} \left(\frac{\Delta_J}{2U} - 1 \right)^2 \frac{U}{\Delta_J}. \quad (5.11)$$

Even though the BG regions survive for even higher disorder strength than the Mott-lobes, they analogously disappear one after the other and finally the last one vanishes at

$$\frac{\Delta_J}{U} = 2 \left(3 - 2\sqrt{2} \right) \approx 0.3431. \quad (5.12)$$

The SF phase exists for infinitesimal small tunneling rates between these BG regions. At the ends of the BG regions narrowing tips occur, which are located along the line of mean integer filling but finally end in the SF region. They occur due to the criterion for the definition of the MI and SF sites bases on integer filling, given by Equation (4.15). In

the BG regions inside of this tip, there exist sites in the system, which show local particle fluctuations $\kappa_i = \langle \hat{n}_i^2 \rangle - \langle \hat{n}_i \rangle^2 > 0$ indicating a SF site, while their particle number $\langle \hat{n}_i \rangle$ is integer by chance. By the application of the above criterion these sites are mislabeled as MI sites, even though they rather behave like SF sites due to the occurrence of local particle fluctuations. That is why here the percolation of SF sites is predicted for larger values of the tunneling rate JZ/U . In order to overcome this flaw one could also use a different mapping criterion based on local particle fluctuations.

5.3 Disorder in the inter-particle interaction U

In an experimental setup disorder in the inter-particle interaction U_i can be realized near a Feshbach resonance [52, 53, 108]. We have seen in Section 2.2 that the inter-particle interaction U_i , which is proportional to the scattering length a (see Equation (2.54)), can be tuned from repulsive to attractive interactions in the vicinity of a Feshbach resonance by tuning an external magnetic field B , as shown in Figure 2.5 c). Near the Feshbach resonance small changes in the magnetic field B have a large effect on the scattering length a and consequently also on the resulting inter-particle interaction U_i . Therefore, a magnetic field with weak spatial modulations in the region of the optical lattice, will strongly influence the scattering properties locally and lead to a variety of values of the inter-particle interaction U_i [52, 54]. With this technique disorder in the inter-particle interaction U_i can be introduced without influencing the other BH parameters. Therefore, the inter-particle interaction is the only parameter, for which isolated disorder can be realized.

A uniform distribution of this parameter has been studied in [52, 54]. The phase diagrams for inter-particle interaction disorder, where U is the mean value of the disorder distribution

$$p(U_i) = U + \frac{1}{\Delta_U} \Theta \left(\frac{\Delta_U}{2} - |U_i| \right) \quad (5.13)$$

resulting from LMF cluster analysis [2], are shown in Figure 5.3. Analogously to the disordered tunneling case we find a finite number of Mott-lobes. Intuitively this can be understood by recalling the MI boundaries (2.61) of the ordered case, as we have already discussed for tunneling disorder. For small tunneling rates, the first SF sites occur where the tunneling rate J overcomes the reduced inter-particle interaction $U - \Delta_U/2$. Thus, the Mott-lobes shrink all by the same amount for fixed disorder strength Δ_U . Therefore, the smallest Mott-lobes of the ordered system disappear for small but non-zero disorder strength Δ_U leading to a finite number of Mott-lobes. Along the μ/U -axis the Mott-lobes spread from

$$\mu_- = (n-1) \left(U + \frac{\Delta_U}{2} \right) \quad \text{to} \quad \mu_+ = n \left(U - \frac{\Delta_U}{2} \right) \quad (5.14)$$

and they disappear at the critical disorder strength

$$\Delta_U^c/U = \frac{2}{2n-1}, \quad (5.15)$$

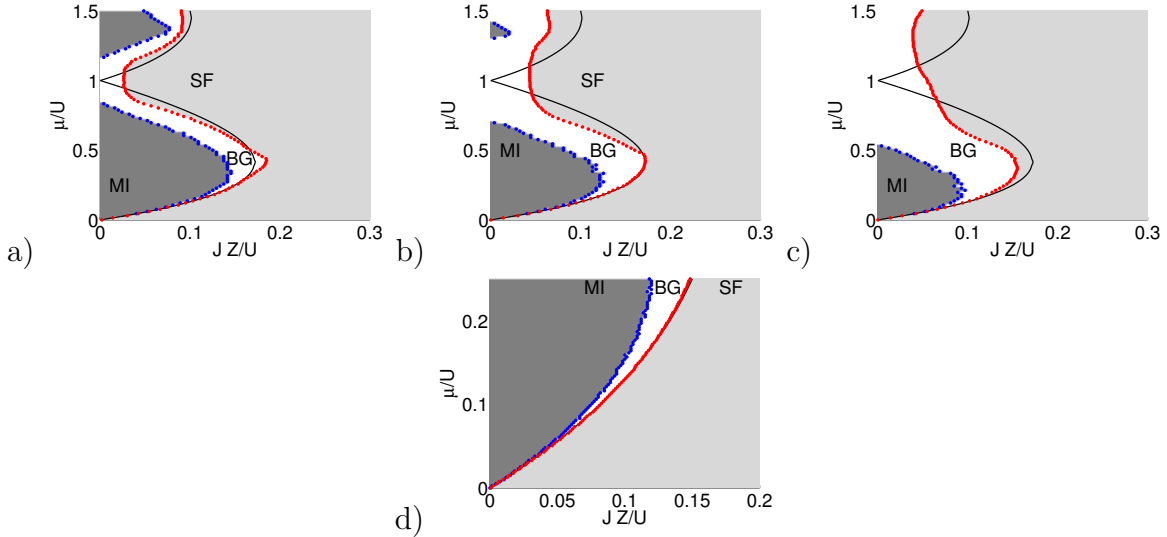


Figure 5.3: Phase diagram for box distributed disordered inter-particle interactions U_i with the disorder strengths $\Delta_U/U = 0.35, 0.6, 0.95$ and a blow-up for $\Delta_U/U = 0.6$. There is a finite number of Mott-sites, which disappear one after the other for increasing disorder strength Δ_U/U . One BG region and for even higher values of the tunneling rate JZ/U one SF region surrounds the Mott-lobes. These phase diagrams show the tricritical point at $\mu/U = JZ/U = 0$, where all three phases approach each other tightly.

where μ_- and μ_+ meet [52]. As the critical disorder strength Δ_U^c depends on the number n of the specific Mott-lobe, they vanish one after the other, until for $\Delta_U^c/U = 2$ the first Mott-lobe is the last to disappear. For all disorder strengths there is only one connected BG region, respectively one SF region. This is different from the system with tunneling disorder, but analogous to the on-site disordered case.

A new feature occurs below the first Mott-lobe, which is shown as a blow-up in the second row of Figure 5.3. In this region the BG-SF transition widely follows the MI-SF transition of the ordered case given by Equation (2.61). Between this transition line and the MI-BG transition line the BG phase forms a narrowing strip. Both transition lines approach each other tightly for small tunneling rates and form a tricritical point in the limit $\mu/U \rightarrow 0$ and $JZ/U \rightarrow 0$, which does not contradict the fact that a direct transition from MI to SF is impossible in the disordered case [19, 20].

This phenomenon can be understood recalling the transition line of the ordered system given in Equation (2.61) and studying the behavior of this equation under a variation of U [4]: According to its derivation, Equation (2.61) describes the transition line, at which the SF order parameter $\bar{\psi}$ becomes non-zero in the ordered case. In the disordered case this takes place at the BG-SF transition. Therefore, the BG-SF transition line in the disordered case follows Equation (2.61) in regions, where it is stable against variation of the inter-particle interaction U . This variation of $\mu_{\pm}(J, Z, U, n)$ under a change of U is given by the derivative

$$\frac{\partial \mu_{\pm}}{\partial U} = n - \frac{1}{2} \mp f(x) \text{ with } f(x) = \frac{x - 1 + 2xn}{2\sqrt{(x - 1)^2 - 4xn}}, \quad (5.16)$$

where $x = JZ/U$ is a small parameter since Equation (2.61) is a perturbative result for small x , as shown in Section 2.2.3.1. With the Taylor expansion $f(x) \approx -\frac{1}{2} - x^2 n(n+1)$ for small x , where the linear term in x cancels, we get

$$\frac{\partial \mu_{\pm}}{\partial U} \approx \begin{cases} x^2 n(n+1) + n & \text{upper branch,} \\ -x^2 n(n+1) + n - 1 & \text{lower branch.} \end{cases} \quad (5.17)$$

In general for $n = 1, 2, \dots$ this derivative is non-zero. In case of the first Mott-lobe ($n = 1$) it reduces to

$$\frac{\partial \mu_{\pm}}{\partial U} \approx \begin{cases} 2x^2 + 1 & \text{upper branch,} \\ -2x^2 & \text{lower branch,} \end{cases} \quad (5.18)$$

and for the lower branch the derivative vanishes for zero tunneling rate ($x = 0$). There exists no other configuration for which this derivative becomes zero. For small tunneling rates $0 < x < 1$ the rate grows sublinearly. This means that the lower branch of the first Mott-lobe is fairly stable against variation of U . For all other Mott-lobes with $n > 1$ the absolute value of the derivative is positive, even for small tunneling rates J . This feature of the lower branch of the first Mott-lobe is unique and does not occur for other branches of the disordered inter-particle interaction case, the tunneling or on-site disorder case. Therefore, the BG-SF transition of the inter-particle interaction disordered system below the first Mott-lobe widely follows the transition line of the ordered system [4] leading to the occurrence of the tricritical point at the origin of the phase diagram.

Conclusion

The influence of disorder in one of the BH parameter on the phase diagram leads to characteristic different features. For disordered on-site energies we find an infinite number of Mott lobes for small disorder strengths, which all simultaneously disappear at the critical disorder strength $\Delta_e^c/U = 1$. They are surrounded by one connected BG and one SF region.

For disordered tunneling rates, there only exists a finite number of Mott-lobes, which disappear one after the other with increasing disorder strength until the last one vanishes at $\Delta_J^c/U = (3 - 2\sqrt{2})/2 \approx 8.58 \cdot 10^{-2}$. As a new feature, the SF region also exists in the limit of vanishing tunneling rates and separates individual BG regions from each other. These individual BG regions also disappear one after the other and finally the last one vanish at $\Delta_J/U = 2(3 - 2\sqrt{2}) \approx 0.3431$.

In the case of disordered inter-particle interactions there also exists a finite number of Mott-lobes, which again vanish one after the other and the last one disappearing at $\Delta_U^c/U = 2$. Moreover, in this case there exists a tricritical point in the limit of vanishing chemical potential and tunneling rates, where all three phase approach each other asymptotically. As we have shown this results from the fact, that the lower branch of the first Mott-lobe is stable against variations of U .

The understanding of the characteristics of these three different types of disorder scenarios, will help us to understand phase diagrams of systems in which disorder affects

all BH parameters, as we usually find them in experiments. One common experimental realization of disorder is a quasi-periodic bi-chromatic optical potential, which we will discuss in the next chapter.

6 Quasi-periodic bi-chromatic potentials

One possible realization of disorder in an experiment is to use a bi-chromatic potential [3], where two overlapping optical lattices with incommensurate wave lengths form a quasi-periodic potential for the bosons, which leads to locally varying BH parameters. Their distribution can be described by the mean value and the variance of the PD for each BH parameter separately. With the help of both quantities the quasi-periodic potentials can be compared to the results of uncorrelated disorder in each of the BH parameters, as discussed in the preceding chapter. While the effect of bi-chromatic potentials on the BH parameters has only been described approximatively so far [37, 38, 55–57], we will follow the general derivation of the BH model, as presented in Chapter 2, by the determination of generalized Wannier functions and the corresponding BH parameters for each lattice site individually. In this way we introduce disorder to the BH model in a fundamental way. We will study the PD for each BH parameter and especially compare the occurring disorder strengths with the results of isolated uncorrelated disorder, which we have discussed in the last chapter. We will be able to show that, in contrast to the common expectation, the effect of tunneling disorder is actually not negligible and has a recognizable effect on the resulting phase diagram.

6.1 Bi-chromatic potentials

In an experiment disorder can be introduced either by a diffuser [26, 27] or by a bi-chromatic potential [3]. The diffuser modifies the intensity of the laser, which leads to inhomogeneities in the resulting optical lattice. For a detailed comparison with theoretical predictions a thorough characterization of the diffuser is necessary. Especially the width of the disorder distribution is a crucial system parameter, which cannot be tuned precisely. Alternatively a bi-chromatic potential is formed by a main optical lattice with a high intensity, which is superposed by a second weaker one with slightly different wave length [3]. By varying the amplitude of the second lattice the strength of disorder can be adjusted freely. With vanishing difference between the wave lengths, the period of such a pattern increases. Below a critical value of the difference of the two wave lengths the period of the pattern extends the system size. In this regime this so-called quasi-periodic potential serves as a model for uncorrelated disorder, showing local inhomogeneities. The quasi-

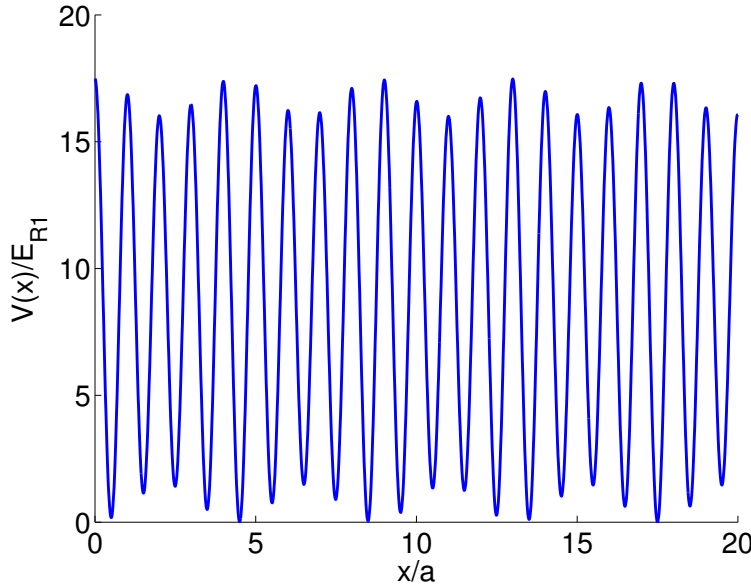


Figure 6.1: A 1D quasi-periodic potential according to $V(x) = V_1 \cos^2(k_1 x) + V_2 \cos^2(k_2 x)$ with the parameters $s_1 = 16$, $s_2 = 2.5$ and $V_2/V_1 \approx 0.09$. This potential shows inhomogeneities in the depth of the lattice and the barrier between the lattice sites.

periodic potential in two dimensions is given by

$$\begin{aligned} V(x, y) &= V_1 (\cos^2(k_1 x) + \cos^2(k_1 z)) \\ &\quad + V_2 (\cos^2(k_2 x) + \cos^2(k_2 z)), \end{aligned} \quad (6.1)$$

with the wave vectors $k_i = 2\pi/\lambda_i$ ($i = 1, 2$), the lattice constant $a = \pi/k_1$ and the intensities $V_i = s_i E_{Ri}$, which are given in units of the recoil energy $E_{Ri} = \hbar^2 k_i^2 / (2m)$. In the present simulations the wavelengths are chosen to be $\lambda_1 = 830$ nm and $\lambda_2 = 1076$ nm with reference to the experimental setup of [3]. In experiments ^{87}Rb atoms, which have a mass of $m_{\text{Rb}} = 1.45 \cdot 10^{-25}$ kg, are widely used. The amplitude of the main lattice s_1 determines the depth of the lattice. The amplitude of the second lattice s_2 is by far smaller than the first one, $s_2 \ll s_1$, and increases the influence of the disorder. Such a quasi-periodic potential in one dimension is shown in Figure 6.1 for a high value of s_2 . In comparison to a regular lattice there are inhomogeneities in the depth of the lattice and the barrier between the lattice sites.

6.1.1 Generalized Wannier functions

The calculation of the Bloch and the Wannier functions in the ordered case as described in Section 2.2.1, can also be applied to the non-symmetric case ($0 \neq s_2 \ll s_1$). Since the quasi-periodic potential (6.1) is a sum of individual periodic functions the Fourier-transform of the potential can be calculated analytically and individually for each summand according to Equation (2.50). In contrast to the regular case, where the determination of the Wannier function is necessary only for one lattice site, the Wannier function

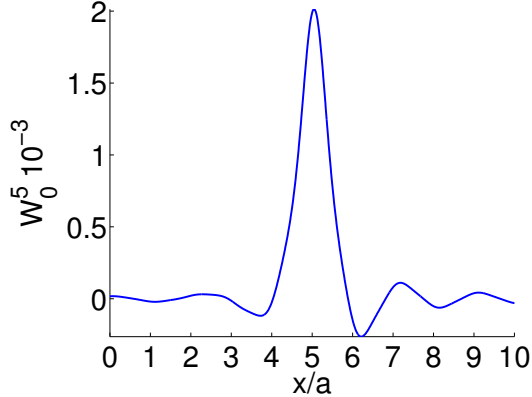


Figure 6.2: Wannier functions for a disordered asymmetric lattice for the parameters $s_1 = 2$, $s_2 = 1$ with $V_2/V_1 \approx 0.3$ for $l = 5$ and $n = 0$. The corresponding Wannier function for a symmetric lattice is shown in Figure 2.7.

in the non-symmetric case must be calculated for each site individually, therefore the computation time scales with the system size $M = L^2$. The resulting Bloch functions

$$\psi_n^{\vec{q}}(\vec{r}) = u_{\vec{q}} e^{i\vec{q}\vec{r}} \text{ with } u_{\vec{q}}(\vec{r}) = \sum_{\vec{G}} c_n^{\vec{q}-\vec{G}} e^{-i\vec{G}\vec{r}} \quad (6.2)$$

still form an orthogonal basis, but their coefficients $u_{\vec{q}}(\vec{r})$ are no longer periodic. But also in this case, localized functions which can be interpreted as generalized Wannier functions can be constructed according to Equation (2.51). As one can see in Figure 6.2, these functions are still localized at a specific lattice site, but they are asymmetric reflecting the asymmetry of the underlying lattice.

With this generalization of the Wannier functions for a asymmetric lattice system we follow the usual derivation made introducing the BH model in literature [22, 64] as described in Section 2.2.2. All BH parameter in the Hamiltonian (2.55) are site dependent now and can be computed on the basis of the generalized Wannier function according to Equation (2.56). With this method we introduce disorder via quasi-periodic potentials fundamentally in the calculations. Other approaches [37, 38, 55, 109, 110] avoid the computation of any Wannier function and describe this effect on the BH parameter effectively and argue that only disorder in the on-site energies is relevant. In Section 6.1.2 we will discuss the accuracy of these methods. Moreover, in other works [56, 57] the symmetric Wannier functions are used as an approximation for the quasi-periodic case. In Section 6.3.2 we will show that this is only accurate for $s_2 < 0.1$. Before we do this, in the next section we will use these generalized Wannier functions in order to determine the BH parameters.

6.1.2 Distributions of the Bose-Hubbard Parameters

For fixed values of s_1 and s_2 we get a set of individual BH parameters ϵ_i , J_{ij} and U_i at each lattice site. Exemplarily the BH parameters for $s_1 = 10$ and $s_2 = 0.5$ are shown

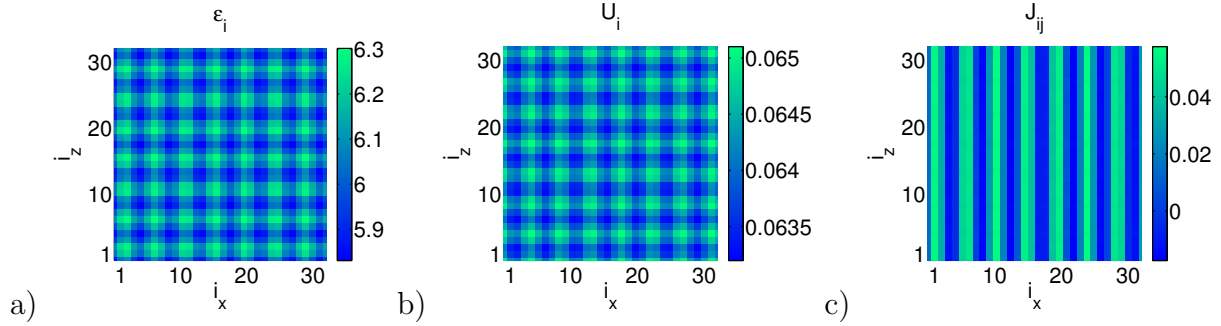


Figure 6.3: BH Parameters for a quasi-periodic potential according to Equation (6.1) with $s_1 = 10$ and $s_2 = 0.5$. The tunneling rate at site $i = (i_x, i_z)$ yields the value for the tunneling rate to the neighbor $j = (i_x + 1, i_z)$. Note that this contains all information, since the tunneling rate J_{ij} , given in Equation (2.56), is symmetric under a change of the indices and the Potential $V(x, z)$ (6.1) under a change of the coordinates x and z .

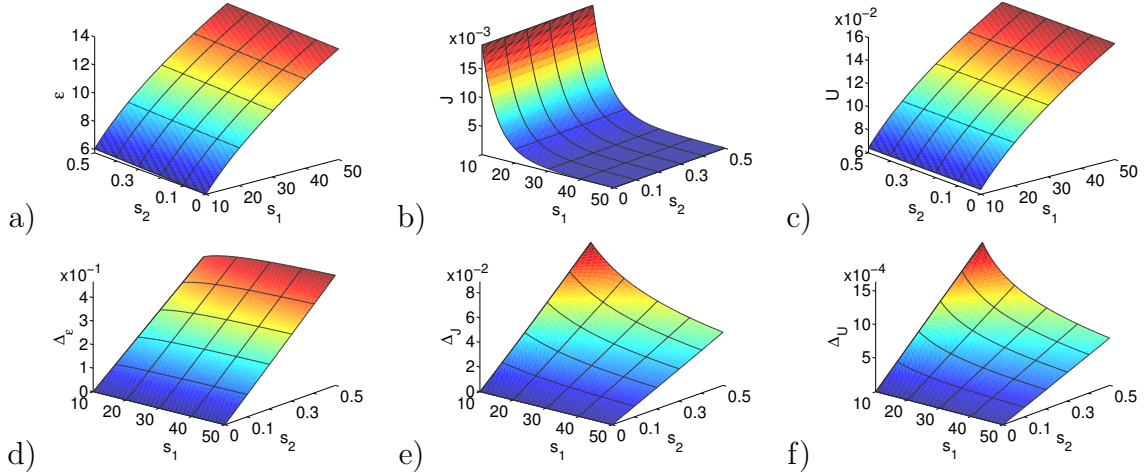


Figure 6.4: Mean values α (first row) and widths $\Delta_\alpha = \sqrt{12\sigma_\alpha^2}$ (second row) with variance σ_α^2 of the distributions of the BH-Parameters $\alpha = \epsilon, J, U$ in units of the recoil energy E_{R1} . Notice that in the figures of ϵ and U the s_1 - and s_2 -axis are switched in comparison to the other figures. As expected the mean value of ϵ and U increase with the depth s_1 of the lattice, while the mean value of J decreases. The widths of the distributions Δ_α increases with the amplitude s_2 of the second lattice.

in Figure 6.3. In the diagram showing ϵ_i , J_{ij} and U_i each pixel represents the value at a specific site. The BH parameters follow the modulation of the lattice potential and depend on the specific lattice site. Therefore, we now deal with distributions $P(\alpha)$ with $\alpha = \epsilon, J, U$, which depend on the parameter set (s_1, s_2) chosen for the amplitudes of the two lasers. Now we will especially focus on their mean value $\bar{\alpha} = \int d\alpha \alpha P(\alpha)$ and their variance $\sigma_\alpha^2 = \int d\alpha \alpha^2 P(\alpha)$. Since we want to compare results to the box distributed case from Chapter 5, where the variance is $\sigma_\alpha^2 = \Delta_\alpha^2/12$, we define the width of the distribution Δ_α according to this equation. With the help of both benchmarks we are able to compare the distributions with the scenarios of disorder in only one BH parameter,

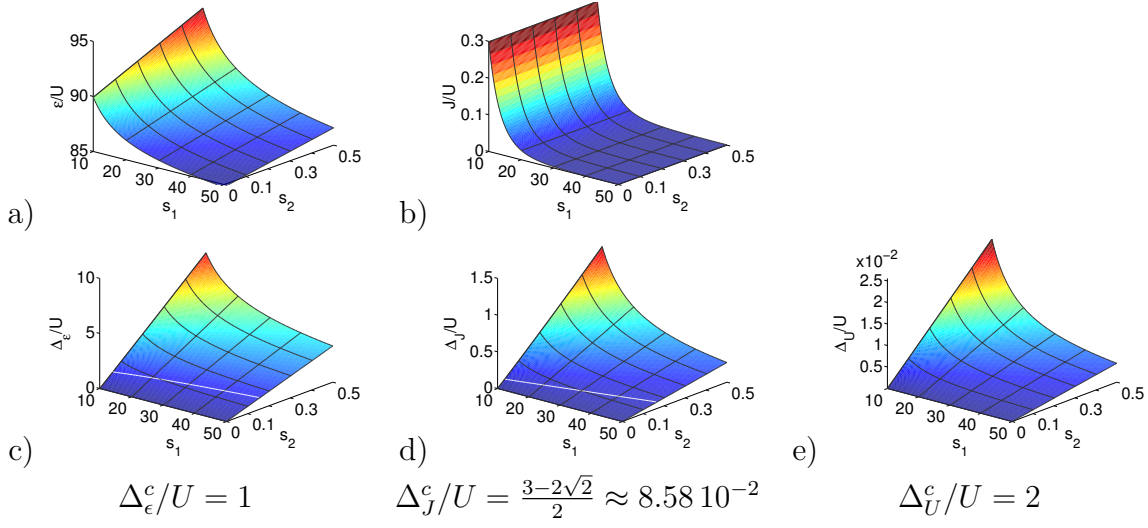


Figure 6.5: Mean values $\bar{\alpha}$ (first row) and the widths $\Delta_{\alpha} = \sqrt{12\sigma_{\alpha}^2}$ (second row) of the distributions of the BH-Parameters $\alpha = \epsilon, J, U$ in units of the inter-particle interaction U . The white lines in the second row show the critical widths Δ_{α}^c , where the last Mott-lobe disappears, which is also stated below the plot. In the case of on-site disorder as well as for tunneling disorder the widths of the distributions reach the critical value Δ_{α}^c .

as introduced in Chapter 5. The mean value of the distribution $P(\alpha)$ here matches the site independent BH parameters $\alpha = \epsilon, J$ and U from Chapter 5, while the width of the distribution

$$\Delta_{\alpha} = \sqrt{12\sigma_{\alpha}^2} \quad (6.3)$$

corresponds to the disorder strength given as free parameter in Chapter 5.

The resulting mean value and width of the distribution in units of the recoil energy E_{R1} are shown in Figure 6.4. The amplitude of the main lattice s_1 is one order of magnitude larger than the one of the second lattice s_2 . In a shallow lattice (s_1 small) the mean value of the on-site energy ϵ and the inter-particle interaction U are small and grow with increasing depth of the lattice s_1 . The mean value of the tunneling rate J reaches its maximal value in a shallow lattice (s_1 small) and decreases in a deep lattice (s_1 large). All mean values are independent on the strength s_2 of the second lattice. The width Δ_{ϵ} of the distribution of the on-site energy is independent of the amplitude of the main lattice s_1 , but increases with the amplitude of the second lattice s_2 . As expected the amplitude of the second lattice s_2 indeed increases the disorder strength in the system. The width Δ_J of the distributions of the tunneling rate and the inter-particle interaction Δ_U show a corresponding behavior, which depends on both parameters s_1 and s_2 , however their maximal values differ substantially. Both show increasing widths for increasing s_2 and adopt the maximal values for a shallow (s_1 small) and strongly disordered (s_2 large) lattice.

In Figure 6.5 the mean values $\bar{\alpha}$ and widths Δ_{α} of the distributions of the values $\alpha = \epsilon, J, U$ are shown in units of the inter-particle interaction U . The critical disorder strength at which the last Mott-lobe disappears, in the case where only one isolated BH parameter

is disordered, is given below the figures and as a white line in the graphs. The critical disorder strength for pure on-site energy disorder is given by $\Delta_\epsilon^c/U = 1$ and for pure tunneling rate disorder by $\Delta_J^c/U = (3 - 2\sqrt{2})/2 \approx 0.0858$. Above these values only the BG and SF phase remain. A comparison of these critical values with the widths of the distribution in units of U , displayed in Figure 6.5, shows that both, the width of the distribution of the on-site energy, as well as the tunneling rate reach the region, where all three phases occur in the phase diagram. Even though the occurring width of the distribution of the tunneling rate Δ_J is smaller than the width for the on-site energy Δ_ϵ , it reaches the parameter range, where all three phases compete in the phase diagram. This is in contrast to the width of the inter-particle interaction Δ_U , which indeed is small in comparison to the range in which all three phases occur. The field of on-site disorder has widely been studied in theory [2, 20, 29, 34–36, 44, 46, 49]. Our studies, however, show that this treatment is not sufficient, since in a quasi-periodic lattice system, like it is used in various experiments [3], the effects of disorder in the tunneling rate is not negligible and will affect the actual experimental phase diagram as well as the disorder in the on-site energy.

6.2 Phase diagrams

Let us first discuss the phase diagram for integer filling in dependence of the two laser intensities s_1 , which describes the intensity of the main lattice, and s_2 , which is one order of magnitude smaller and describes the influence of the disorder. Since the BH parameters are functions of the laser intensities, as derived in Section 6.1.2, it is possible to transform the phase diagram in dependence of the intensities into one, which depends on the BH parameters $\Delta_\epsilon/(2J)$, $\Delta_J/(2J)$ and U/J . This representation can be compared to common representations of the phase diagram of the BH model, as for example for on-site disorder, as shown in Figure 4.4.

Secondly, the phase transitions are determined in dependence of the chemical potential μ and the intensity s_1 of the main lattice for fixed intensity s_2 of the second one. This phase diagram can be compared to these for isolated disorder in one of the BH parameters, where the disorder strength is fixed and the phase transitions are given in dependence of the chemical potential μ/U and the tunneling rate JZ/U , as shown in Figure 4.5 and all figures of Chapter 5.

6.2.1 Intensity phase diagram

With BH parameters for each the site at hand we can determine the phase diagram in dependence of the laser intensities s_1 and s_2 for fixed mean particle number $N = \sum_i \langle \hat{n}_i \rangle = M$ of one particle per site. The mean particle number is fixed by adjusting the chemical potential μ . The resulting phase diagram for a 32×32 lattice is shown in Figure 6.6 a). Here the BH parameters are correlated according to the lattice potential (6.1). According to the LMF cluster analysis described in Chapter 4, the MI phase is characterized by the absence of any SF site, which means that every site in the MI region has an integer

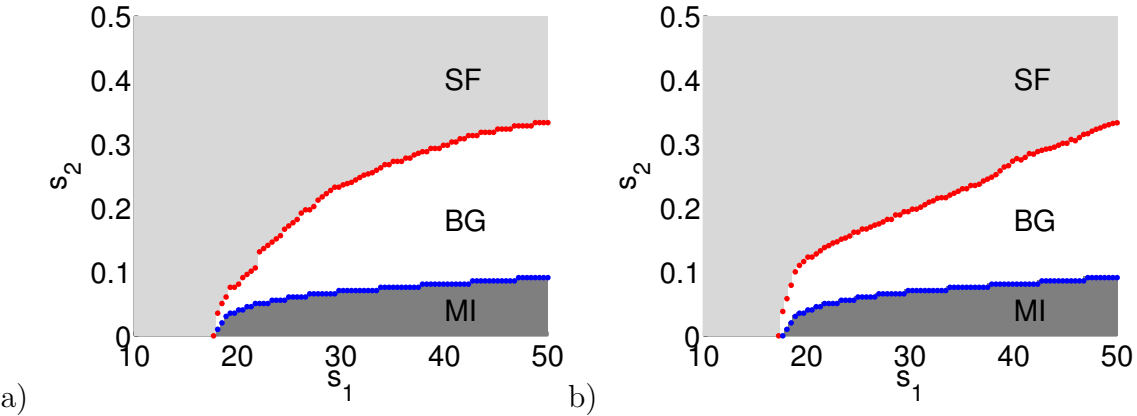


Figure 6.6: Phase diagram for the bi-chromatic quasi-periodic potential (6.1) for a mean particle number of $\bar{n} = 1$ in dependence of the laser intensities s_1 and s_2 for a system with 32×32 sites (a) and a system with uncorrelated disorder (b). In the ordered case ($s_2 = 0$) a direct phase transition between the MI and the SF phase exists. With increasing s_2 the MI, BG and SF phase occur in a stack.

particle number. In the SF region sites with non-integer particle number percolate. In between, in the BG region, the system consists of both, sites with integer and others with non-integer particle number, which do not percolate.

Next we compare the obtained phase diagram for the quasi-periodic potential with the one obtained for a BH model with uncorrelated disorder according to identical PDs of the BH parameters $P(\alpha)$ with $\alpha = \epsilon, J, U$, which depend on the laser intensities s_1 and s_2 . We start with one parameter set for ϵ, J and U given for fixed s_1 and s_2 , which we have determined and discussed in Section 6.1.2. We produce 200 different samples, by randomly choosing new site indices. In other words, we study 200 samples according to the same PD by switching lattice sites and in this way erasing local correlations in the parameter set. The phase diagram resulting from LMF cluster analysis and finite-size scaling is shown in Figure 6.6 b) and agrees quite well with the one on the left for correlated disorder. The BG-SF transition line for uncorrelated disorder is slightly distorted in comparison to correlated disorder.

In both phase diagrams, shown in Figure 6.6, all three phases occur in dependence of the lattice parameters s_1 and s_2 . Along the s_1 -axis ($s_2 = 0$) the direct SF-MI transition of the ordered system occurs. Below this point in a shallow lattice the SF phase covers the whole parameter region independent of s_2 . This corresponds to the fact that in this region the tunneling rate is largest, as shown in Figure 6.4 and dominants the system behavior. Above this point the MI phase occurs, which is completely surrounded by the BG for intermediate s_2 , which in turn is enclosed by the SF phase for even larger amplitudes s_2 of the second lattice. Notice that the potential (6.1) reduces to the ordered case for $s_2 = 0$ as well as for $s_1 = 0$. Therefore, along the s_2 -axis the system also undergoes a direct MI-SF transition. In the region where $s_1 \ll s_2$ the second lattice is dominant and a similar structure occurs.

6.2.2 Bose Hubbard parameter phase diagram

In the case of only one disordered BH parameter two possible representation of the phase diagram are common: For the first one [2,35] the particle number is fixed to one particle per site, which fixes the chemical potential μ . Then, the phase transitions are shown in dependence of the inter-particle interaction U/J and the disorder strength $\Delta/(2J)$. The phase diagram for the case of disorder only in the on-site energy in this representation is shown in Figure 4.4. The second representation [2, 43–45] shows the Mott-lobes in dependence of the tunneling rate JZ/U and the chemical potential μ/U for fixed disorder strength Δ/U . The corresponding phase diagrams for the case of disorder only in one of the BH parameters are shown in Figure 5.1, 5.2 and 5.3. In this section we will discuss our results in both representations, keeping in mind that all BH parameters ϵ , J and U as well as all disorder strengths Δ_ϵ , Δ_J and Δ_U are functions of s_1 and s_2 and thus are not independent of each other.

6.2.2.1 Commensurate filling

The data from the phase diagram as a function of s_1 and s_2 shown in Figure 6.6 can be translated into a diagram similar to the first representation for a fixed particle number: According to Figure 6.4 the mean parameters ϵ , J , U as well as the widths Δ_ϵ , Δ_J , Δ_U are functions of the two amplitudes s_1 and s_2 . Since Δ_U is two orders of magnitude smaller than the critical value Δ_U^c and smaller than the other widths, the inter-particle interaction U can be treated as a sharp value to a good approximation. As a result the phase diagram can be visualized as the surface $(U/J, \Delta_\epsilon/(2J), \Delta_J/(2J))$ in three dimensions. This is shown in Figure 6.7 for correlated and in Figure 6.8 for uncorrelated disorder, where each phase is colored differently. Notice that with a quasi-periodic potential (6.1), which depends on the two amplitudes s_1 and s_2 , only this surface in the BH parameter space can be reached, since all BH parameters are functions of s_1 and s_2 . As a consequence disorder, where only one parameter is disordered while the others are fixed, cannot be reached in this phase diagram. Either it is an ordered ($\Delta_\epsilon = \Delta_J = 0$) or a completely disordered ($\Delta_\epsilon \neq 0, \Delta_J \neq 0$) system. This has two important implications: With a quasi-periodic potential neither the whole parameter space nor a pure on-site disorder can be realized.

The phase diagrams in Figure 6.7 and 6.8 show all three phases: The BG phase (blue) separates the MI (dark gray) phase at strong inter-particle interaction U/J from the SF regime (light gray) at weak inter-particle interaction U/J . Both phase diagrams are also shown as a projection on the $(U/J, \Delta_\epsilon/(2J))$ -plane. The phase boundaries differ substantially from those of the BH model with uncorrelated disorder exclusively in the on-site energies as shown in Figure 4.4. Here the SF region shows a bump around $\Delta_\epsilon/(2J) \sim 10$ and a much larger BG region for both correlated and uncorrelated disorder in comparison to the case of exclusively on-site disorder. These differences are due to the additional presence of disorder in the hopping strengths, which we already found to be important in Section 6.1.2.

Moreover, we find differences between Figure 6.7 and the phase diagram as a function

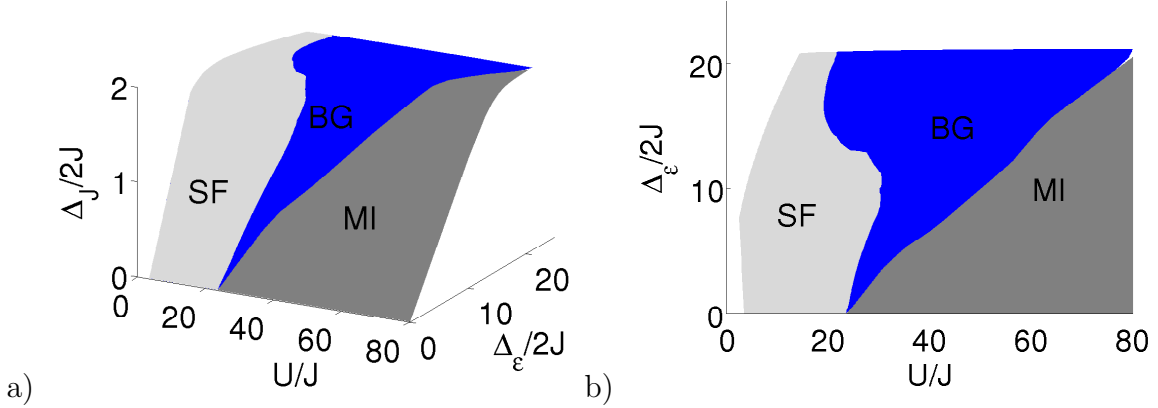


Figure 6.7: Phase diagram for a quasi-periodic potential (6.1) in dependence of the BH parameters $(U/J, \Delta_\epsilon/(2J), \Delta_J/(2J))$. Since these BH parameters all depend on s_1 and s_2 they span a surface in the 3D parameter space. The BG phase separates the MI from the SF region. On the right the projection onto the $(U/J, \Delta_\epsilon/(2J))$ -plane is shown.

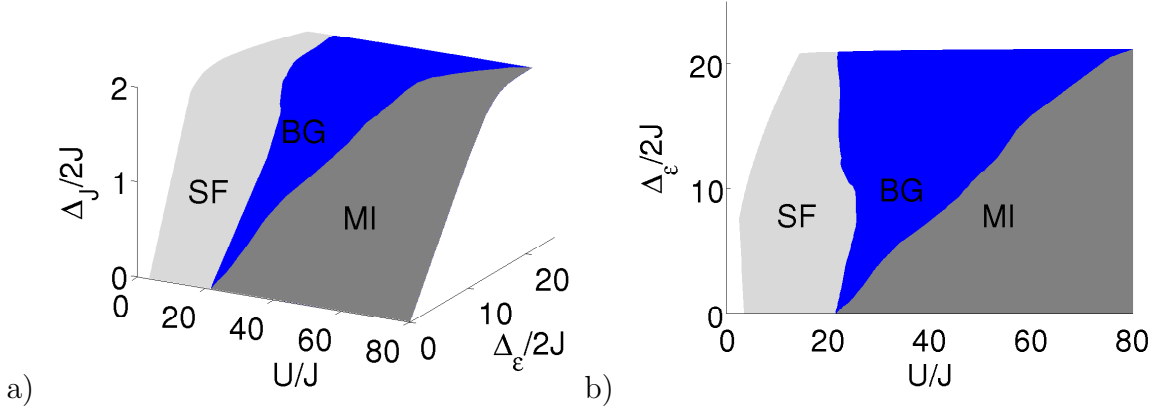


Figure 6.8: Phase diagram for uncorrelated disorder according to the distributions, which result from a quasi-periodic potential (6.1) in dependence of the BH parameter $(U/J, \Delta_\epsilon/(2J), \Delta_J/(2J))$. Since these BH parameters all depend on s_1 and s_2 they span a surface in the 3D parameter space. The BG phase separates the MI from the SF region. On the right the projection onto the $(U/J, \Delta_\epsilon/(2J))$ -plane is shown.

of V_2/J and U/J predicted for a one-dimensional BH model with quasi-periodic modulation of the on-site energies exclusively [37, 38]. Since Δ_ϵ is proportional to $V_2 = s_2 E_{R2}$ according to Figure 6.4, the phase diagram in Figure 6.7 is directly comparable to Figure 1 (left) of [37] and Figure 3 (bottom) of [38]. Both show a direct MI-SF transition along the whole border of the MI region. The latter is absent in our phase diagram in Figure 6.8, where an intervening BG phase occurs between the MI and SF phase. The reason is most plausibly that, already a small disorder strength Δ_J in the tunneling strength strongly enlarges the BG regions in the phase diagram, as Figure 5.2 demonstrates. In

Section 6.3.1 we will discuss the method of [37] in detail and compare it to results of the LMF cluster analysis for the disorder realization as proposed in [37].

6.2.2.2 Fixed disorder strength

For the second representation we fix the weaker amplitude s_2 , which introduces disorder to the system, and study the system in dependence of s_1 and μ . Since the tunneling rate JZ/U is a unique function of s_1 and independent of s_2 , as shown in Figure 6.9 b), the s_1 -axis can easily be converted into a JZ/U -axis. In theoretical works disorder is usually introduced by bounded distributions with zero mean values. In the quasi-periodic case the mean value of the distributions $P(\alpha)$ of the BH parameters $\alpha = \epsilon, J, U$ are non-zero in general, as shown in Figure 6.4. In order to take this into account, we use $\mu - \epsilon$ instead of simply μ at the axis. The phase diagrams as a function of the laser intensity s_1 and the chemical potential $(\mu - \epsilon)/U$ are shown in Figure 6.10 for correlated (first row) as well as for uncorrelated (second row) disorder. Thus, from the data in the (s_1, μ) -plane, we can extract a phase diagram in dependence of JZ/U and $(\mu - \epsilon)/U$, like it is shown in Figure 6.11. Notice that ϵ, J and U , as well as $\Delta_\epsilon, \Delta_J$ and Δ_U are all functions of s_1 and s_2 and are not independent from each other, while in the most simulations of disordered systems they are treated as independent parameters.

In Figure 6.9 the behavior of the system parameters for different values of the laser intensity $s_2 = 0.0354, 0.0758, 0.1162$ is shown as a function of JZ/U . Only in Figure 6.9 b) the tunneling rate in dependence of s_1 is shown. While the tunneling rate JZ/U is independent of s_2 , the on-site energy ϵ/U varies for different values of s_2 . In a shallow lattice (s_1 small) the tunneling rate JZ/U is large, while for increasing s_1 it approaches zero and finally in a deep lattice (s_1 large) the tunneling rate JZ/U is infinitesimally small. This means that in the phase diagram the μ/U -axis at $JZ/U = 0$ may be approached with arbitrary accuracy, but never reached. In a deep lattice (s_1 is large) the ratio ϵ/U is small and increases with growing JZ/U , see Figure 6.9. The disorder strengths $\Delta_\epsilon/U, \Delta_J/U$ and Δ_U/U increase with JZ/U and the amplitude s_2 .

The phase diagrams for three values of the laser intensity $s_2 = 0.0354, 0.0758, 0.1162$ as a function of s_1 and $(\mu - \epsilon)/U$ are shown in Figure 6.10 for correlated (first row) as well as for uncorrelated (second row) disorder. For all values of s_2 we find a regular structure of Mott-lobes, surrounded by individual BG regions. The number of Mott-lobes decreases with increasing disorder amplitude s_2 , which corresponds to an increase of the disorder strengths $\Delta_\epsilon/U, \Delta_J/U, \Delta_U/U$ with growing s_2 , see Figure 6.9. The regular pattern of Mott-lobes and BG regions repeats in a distance of one along the $(\mu - \epsilon)/U$ -axis. For fixed s_2 the lower and the upper extent of the Mott-lobes have all the same distance to the next integer number. Thus, the Mott-lobes have the same width along the $(\mu - \epsilon)/U$ -axis, while their extension in s_1 -direction shrinks with their number n . Except of the first BG region all the others are separated from each other by SF regions, reaching up to very high values of s_1 . The phase diagrams for both correlated as well as uncorrelated disorder show identical features. In the uncorrelated case the Mott-lobes are slightly smaller than in the correlated case.

The same data shown as a phase diagram as a function of JZ/U and $(\mu - \epsilon)/U$ is given

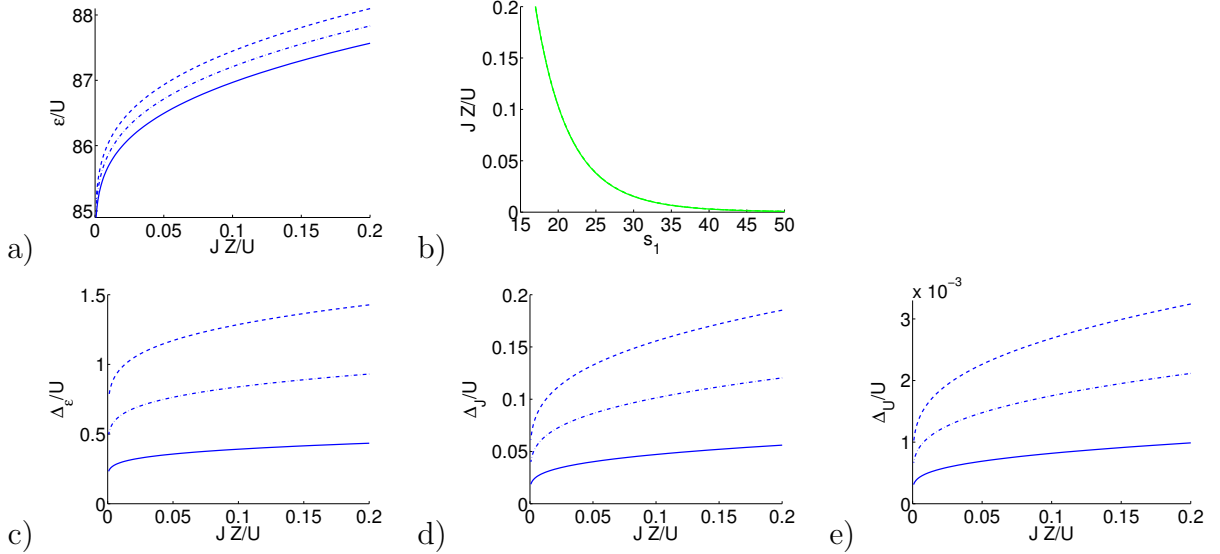


Figure 6.9: The on-site energy ϵ/U and the widths Δ_ϵ/U , Δ_J/U , Δ_U/U of the BH parameters as a function of JZ/U for different values of $s_2 = 0.0354$ (—), 0.0758 (---), 0.1162 (— · —). In Figure b) the tunneling rate JZ/U is shown as a function of s_1 . The tunneling rate is independent of s_2 and a unique function of s_1 . The on-site energy ϵ/U as well as all widths increase with the tunneling rate JZ/U and the amplitude s_2 .

in Figure 6.11 for correlated (first row) as well as for uncorrelated (second row) disorder. Notice that the BH parameters and their widths vary along the JZ/U -axis corresponding to Figure 6.9. Here we also find the structure of Mott-lobes surrounded by BG regions and finally enclosed by the SF phase for large tunneling rates JZ/U . Since the $(\mu - \epsilon)/U$ -axis is not changed in comparison to Figure 6.10, here we also see a decreasing number of Mott-lobes for increasing s_2 and the regular pattern of Mott-lobes, with identical widths for fixed s_2 . They are surrounded by individual BG regions, which are separated from each other by SF regions, except of the first one. The SF regions reach down to very small tunneling rates $JZ/U \rightarrow 0$. This is a unique feature of disorder only in the tunneling rates, as discussed in Section 5.2. The fact that we see this unique phenomenon here in the phase diagram of a quasi-periodic potential, ones more promotes our finding from Section 6.1.2, that the influence of disorder in the tunneling rate cannot be neglected.

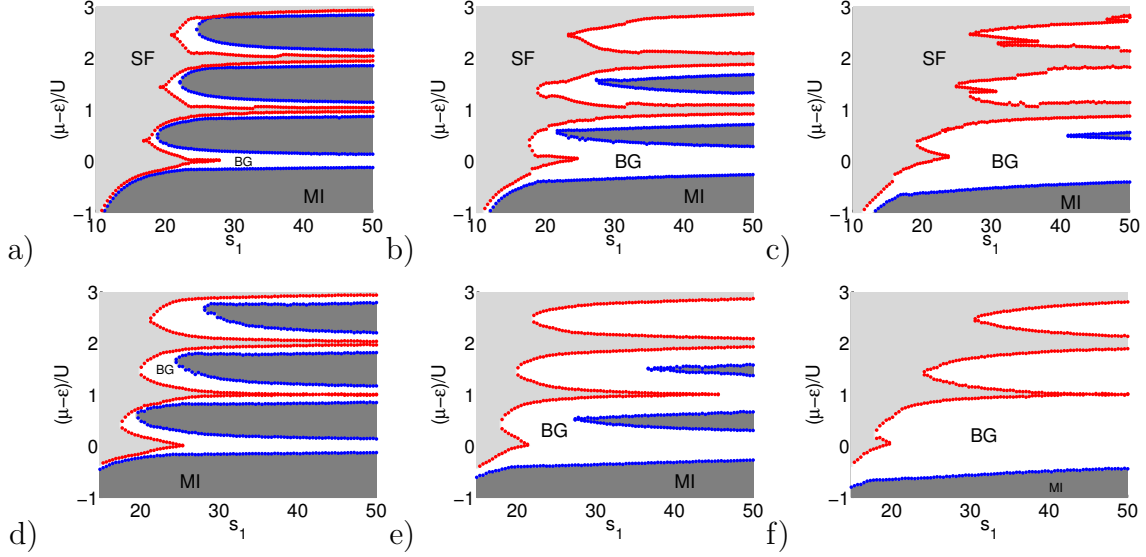


Figure 6.10: Correlated (first line) and uncorrelated (second line) disorder phase diagrams for different $s_2 = 0.0354, 0.0758, 0.1162$ as a function of the laser intensity s_1 and the chemical potential $(\mu - \epsilon)/U$. There is a regular pattern of Mott-lobes, completely enclosed by individual BG regions, which are surrounded by one SF region. The SF regions extend up to high values of the laser intensity s_1 .

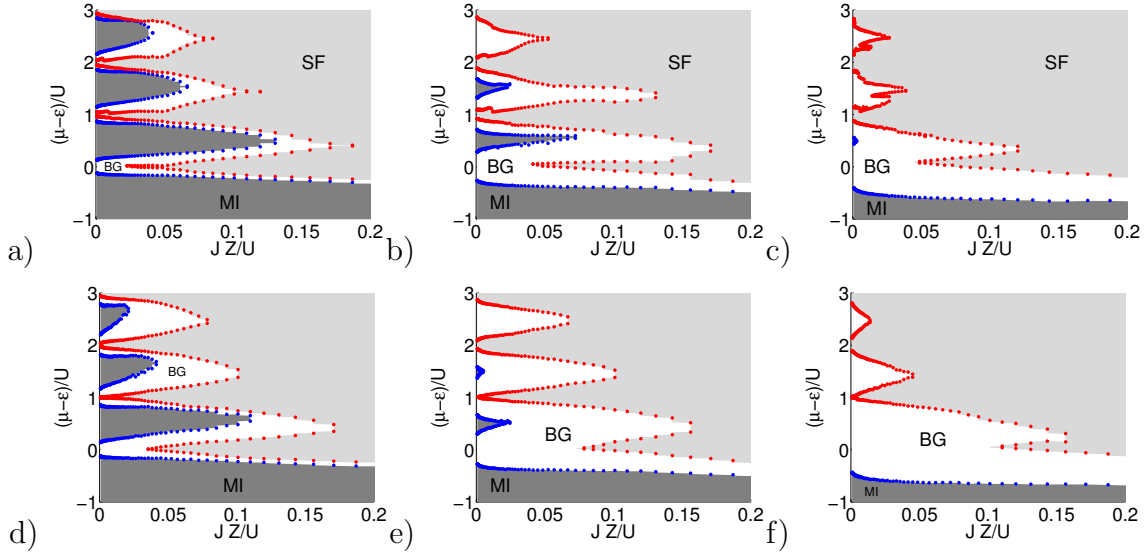


Figure 6.11: Correlated (first line) and uncorrelated (second line) disorder phase diagrams for different $s_2 = 0.0354, 0.0758, 0.1162$ as a function of the tunneling rate JZ/U and the chemical potential $(\mu - \epsilon)/U$. There exists a regular pattern of Mott-lobes, completely enclosed by individual BG phases, which are surrounded by one SF region. The SF regions survive in the limit $JZ/U \rightarrow 0$, which is a unique feature of uncorrelated disorder only in the tunneling rate.

6.3 Comparison with alternative approaches

The numerical effort for the computation of the non-symmetric Wannier functions is immense, as they have to be computed for each site individually. There exist other approaches, avoiding this step by modeling the influence of the quasi-periodic potential either by a specific pattern of the on-sites energies [37, 38, 55] or by using the symmetric Wannier function of the main lattice as an approximation for the non-symmetric ones [56, 57]. Both methods reduce the numerical effort by a factor of the system size $M = L^2$ compared to the computation of generalized Wannier functions. In the following we will discuss the phase diagram on the basis of the LMF cluster analysis for both approximative approaches and discuss their limitations.

6.3.1 Quasi-periodic potential for the Bose-Hubbard parameters

The influence of a quasi-periodic potential on the BH parameters with an alternative approach is discussed in [37]. The authors derive the site dependent perturbations of the BH parameters directly on the basis of the geometric shape of a quasi-periodic potential, as given in Equation (6.1) in one dimension, without computing any Wannier functions. After the authors have determined the resulting perturbations of the tunneling rate and the inter-particle interaction, they argue that these perturbations are small. Thus, they reduce the influence of the quasi-periodic potential to a site dependent on-site energy given by

$$\epsilon_i = V_2 \cos^2(r\pi i + \phi), \quad (6.4)$$

where $r = k_2/k_1$ is the ratio between the two wave vectors and ϕ is a constant phase shift between the first and the second lattice. An agreeing description for the BH parameters was also used in [38, 55].

In agreement with our findings from Section 6.1.2, the perturbation of the inter-particle interaction U is negligible. The authors of [37] argue, that the perturbative tunneling rate J_2 in units of the tunneling rate J is around $J_2/J \approx 0.002 - 0.1$ and the strength of the on-site disorder V_2 in units of the tunneling rate J is around $V_2/J \approx 2.6 - 53.3$. The perturbation of the tunneling rate J_2 is some orders of magnitudes smaller than that of the on-site energy V_2 . Thus, the authors concluded that the tunneling rate can also be neglected here. In Section 5.2 we have seen that the critical tunneling disorder strength is given by $\Delta_J^c/U \approx 0.0858$, beyond which all three phases occur in the phase diagram, and it is one order of magnitude smaller than that of the on-site energy disorder $\Delta_\epsilon^c/U = 1$. Therefore, it is necessary to check carefully if disorder in the tunneling rate is really negligible. On the basis of the data given in [37], there might be parameter ranges, in which it is essential to consider the perturbations in the tunneling rate also.

Their phase diagram as a function of U/J and s_2/J for a fixed mean particle number of $\bar{n} = 1$ for a 1D system is shown in Figure 1 in [37]. Since U/J is proportional to s_1 and independent of s_2 according to Figure 6.9 b), the s_1 - s_2 phase diagram for two dimensions, shown in Figure 6.6, can directly be compared to Figure 1 in [37]. Their phase diagram, for isolated disorder in the on-site energy according to Equation (6.4) shows a direct

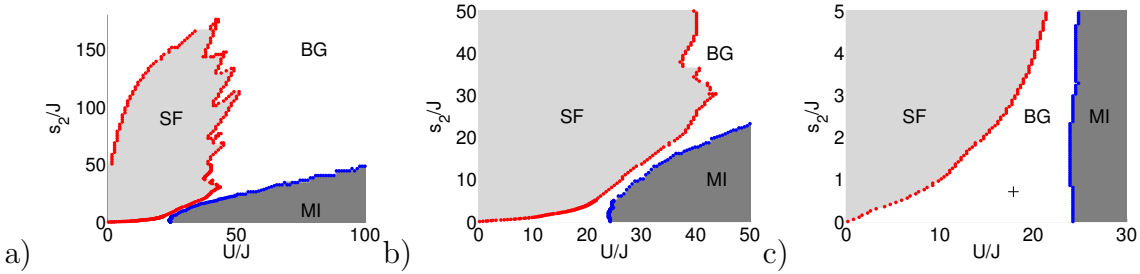


Figure 6.12: The same LMF cluster analysis phase diagram for the quasi-periodic potential given in Equation (6.4) for commensurate particle numbers $\bar{n} = 1$ shown in three different parameter ranges. Especially in Figure b) we see, that there is no direct MI-SF transition, even in the ordered case ($s_2 = 0$). The black cross in Figure c) marks the parameters used in Figure 6.13.

MI-SF transition along the whole border of the MI phase, while we found an intervening BG region between the MI and the SF phase with correlated disorder according to the treatment described in Chapter 6.

In order to study this contradiction we have determined the phase diagram for isolated on-site disorder according to the quasi-periodic potential (6.4) in two dimensions with the help of the LMF cluster analysis described in Chapter 4. The resulting phase diagram is shown in Figure 6.12 for three different parameter ranges. In Figure 6.12 a) we see a large SF region with a fingering border, which is completely surrounded by the BG phase. In the regime of small s_2 we find the MI region. As visible from the blow up in the middle, here we find no direct MI-SF transition, not even for the ordered case ($s_2 = 0$), which is in contradiction to the perturbative result, predicting the MI-SF transition at $U/J \approx 23$, see Equation (2.62). This regime is covered by the parameter range shown in the blowup in Figure 6.12 c). However, in our phase diagram shown in Figure 6.6 computed on the basis of the non-symmetric Wannier functions, we find the direct MI-SF transition for the ordered system. For the parameters marked by the black cross in Figure 6.12 c) the local particle number \hat{n}_i and the discrete map G_i , see Equation (4.15), are shown in Figure 6.13. The local particle number has values on the order of one. In the map G_i on the right, sites with a particle number of one are shown in white, while the SF sites with non-integer particle numbers are shown in black. Here none of the SF clusters percolate. Thus, this represents a typical BG situation, where we find a mixture of MI sites and SF sites, which have not percolated.

We concluded that for the quasi-periodic potential (6.4) with the LMF cluster analysis we find no direct SF-MI transition at all. For the disordered system ($s_2 > 0$) this is in agreement with the phase diagram shown in Figure 6.6 resulting from non-symmetric Wannier functions, but for the ordered system ($s_2 = 0$) this is in contradiction to the perturbative results (2.62). Therefore, the quasi-periodic potential (6.4) cannot describe the influence of a quasi-periodic potential of a 2D system especially in the small disorder (s_2 small) regime. How accurate this potential describes the influence of a quasi-periodic potential of a 1D system, as done in [37, 38, 55], where the phase transition occurs for smaller values of the parameters, is unclear.

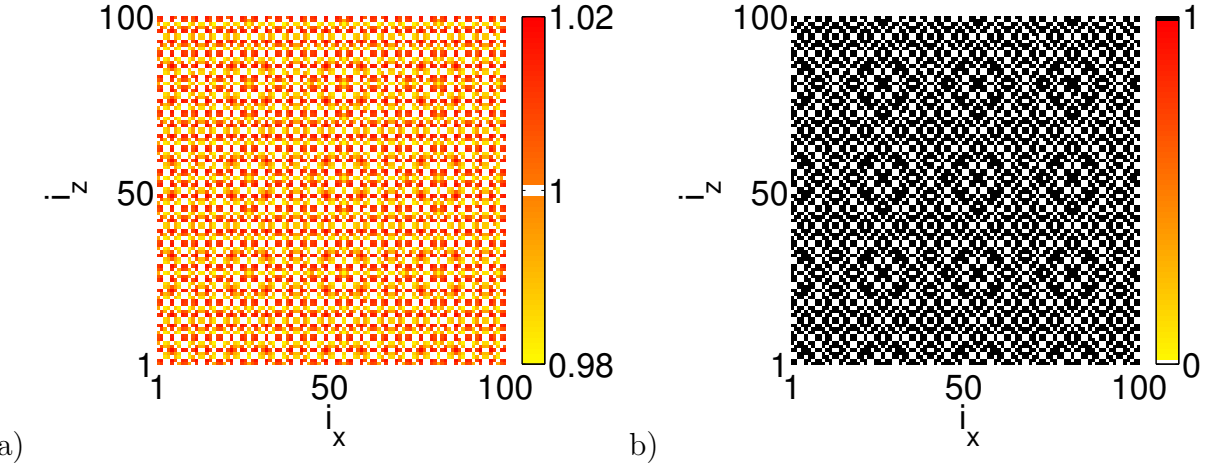


Figure 6.13: The local particle number \hat{n}_i and the discrete map G_i , given by Equation (4.15), for $U/J = 17.88$ and $s_2/J = 0.71$ corresponding to the black cross in Figure 6.12 c). The local particle number \hat{n}_i assumes values on the order of one. On the right MI sites with one particle per site are shown in white, while SF sites with non-integer particle number are shown in black. Here we see a typical pattern of a BG, with a mixture of MI and SF sites, which are not percolated.

6.3.2 Application of symmetric Wannier functions

Another method [56, 57] is to compute the Wannier function for the main periodic lattice

$$V_1(x, y) = V_1(\cos^2(k_1 x) + \cos^2(k_1 z)). \quad (6.5)$$

Then, the BH parameters according to Equation (2.56) are computed on the basis of the full potential (6.1) and the symmetric Wannier functions of the regular lattice V_1 . This drastically reduces the numerical effort in comparison to the computation of the non-symmetric Wannier functions of the full quasi-periodic potential as presented in Section 6.1.1, since here the Wannier function must be computed only once instead of $M = L^2$ times.

In Figures 6.14 and 6.15 the mean values and widths of the BH parameters resulting from this method are shown. In comparison to the results on the basis of the non-symmetric Wannier functions, shown in Figures 6.4 and 6.5, there are no visible deviations for all mean values and the width of the distribution of the on-site energies Δ_ϵ . Nevertheless, there are drastic differences in the width for the tunneling rate Δ_J and the inter-particle interaction Δ_U . The width Δ_J resulting from the symmetric Wannier functions is one magnitude smaller, than those of the non-symmetric Wannier functions, shown in Figure 6.4. Moreover, Δ_J/U , resulting from symmetric Wannier functions, is beyond the critical value of $\Delta_J^c/U \approx 8.58 \cdot 10^{-2}$ for all parameters. In the region of a shallow lattice (s_1 small) it assumes values slightly below the critical values Δ_J^c/U , which means that the influence of disorder in the tunneling rates is not negligible in this region. However, the width Δ_U/U is even ten orders of magnitudes smaller than the one determined using the method with non-symmetric Wannier functions.

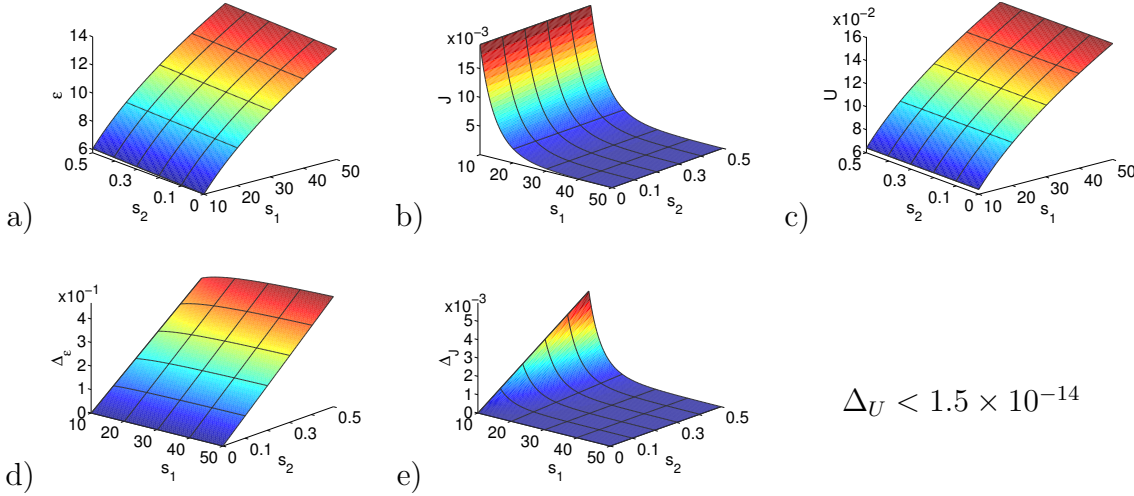


Figure 6.14: Mean values α (first row) and widths $\Delta_\alpha = \sqrt{12\sigma_\alpha^2}$ (second row) with variance σ_α^2 of the distributions of the BH-Parameters $\alpha = \epsilon, J, U$ in units of the recoil energy E_{R1} based on symmetric Wannier functions. Notice that in Figures a) and c) showing ϵ and U the s_1 - and s_2 -axis are switched in comparison to the other figures. In comparison with the method of using non-symmetric Wannier functions, shown in Figure 6.4, the usage of symmetric Wannier functions leads to agreeing results for the mean values and the disorder width Δ_ϵ . The width for the tunneling rate Δ_J is one, and for the inter-particle interaction Δ_U is ten orders of magnitudes smaller here.

The phase diagram for this method is shown in Figure 6.16 for a 10×10 and 32×32 system. The phase diagram on the right for the 32×32 system can directly be compared to the phase diagram for correlated disorder for the same system size shown in Figure 6.6 a). Independent of the system size L both phase diagrams determined on the basis of symmetric Wannier functions, shown in Figure 6.16, reveal a BG-SF transition line, which depends on both system parameters s_1 and s_2 only in a small regime where $s_2 < 0.1$, while for higher values it is independent of s_2 . This is in contrast to the phase diagram determined on basis of non-symmetric Wannier functions, which is shown in Figure 6.6, where the percolation line depends on both parameters s_1 and s_2 and in the high disorder regime (s_2 large) the SF phase covers the whole phase diagram. In Chapter 5 we have discussed uncorrelated disorder only in one of the BH parameters and have seen that for increasing disorder Δ_α (equivalent to increasing s_2) the BG region shrinks. This means that the BG-SF transition line moves to smaller tunneling rates JZ/U , which is inverse proportional to s_1 , as shown in Figure 6.9. Consequently, this means that the BG-SF transition line moves to higher values of s_1 for increasing s_2 . This is consistent with the phase diagram shown in Figure 6.6 determined from non-symmetric Wannier functions, but not with phase diagram shown in Figure 6.16 determined from the symmetric Wannier functions for $s_2 > 0.1$.

The border of the MI phase can only be determined in the regime of the blue dots shown in Figure 6.16. Above a value of $s_2 > 0.1$ the numerical data shows an irregular pattern instead of a precise line. In the parameter regime $s_1 < 20$ there exists no direct MI-SF

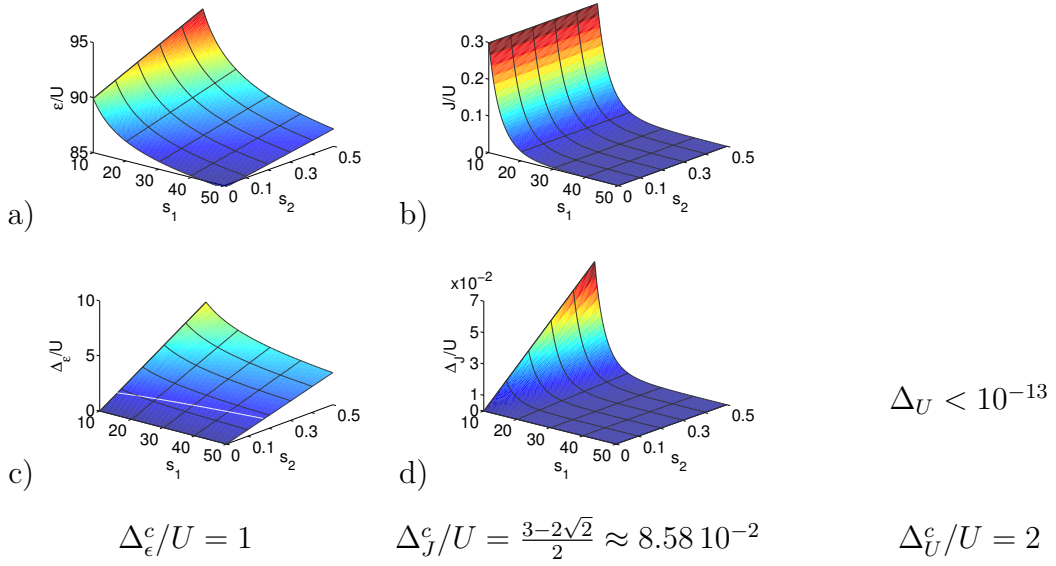


Figure 6.15: Mean values α (first row) and the widths $\Delta_\alpha = \sqrt{12\sigma_\alpha^2}$ (second row) of the distributions of the BH-Parameters $\alpha = \epsilon, J, U$ in units of the inter-particle interaction U based on symmetric Wannier functions. The white lines in the second row show the critical widths Δ_α^c , where the last Mott-lobe disappears, which is also stated below the plot. For on-site disorder the width of the distributions reach the critical value Δ_α^c . The width of the tunneling rates Δ_J approaches this critical value Δ_α^c only for very shallow lattices (s_1 small).

transition and for the 32×32 system on the right not even in the ordered case ($s_2 = 0$). This phenomenon is similar to what we have seen in the last section in the phase diagram in Figure 6.12. Although, the MI-SF transition in the ordered system is predicted at $U/J \approx 23$ according to Equation (2.62), it does not occur here. Therefore, we conclude that for a 2D system the usage of symmetric Wannier function is not applicable even in the regime of very small amplitudes of the second laser s_2 . Above this threshold this approximation leads to misleading results in the phase diagram. This method was introduced for a 1D BH system [56, 57], where the phase transitions of uncorrelated disorder in one BH parameter naturally occur for smaller values of $\Delta/(2J)$ and U/J . Therefore, the amplitudes s_1 and s_2 are smaller, too, and possibly this approximation might hold there with a higher accuracy.

Conclusion

We have investigated the quasi-periodic potential of a bi-chromatic potential and introduced it fundamentally using generalized Wannier functions. In Chapter 5 we had already showed that the critical disorder strength Δ_J^c for tunneling disorder, below which all three phases occur in the phase diagram, is one order of magnitude smaller than for the on-site interaction. Here, we have seen that for bi-chromatic quasi-periodic potentials the width of the distribution of the tunneling rate, as well as that of the on-site energy, reach the physically interesting region on the order of Δ_ϵ^c and Δ_J^c , where all three phases compete

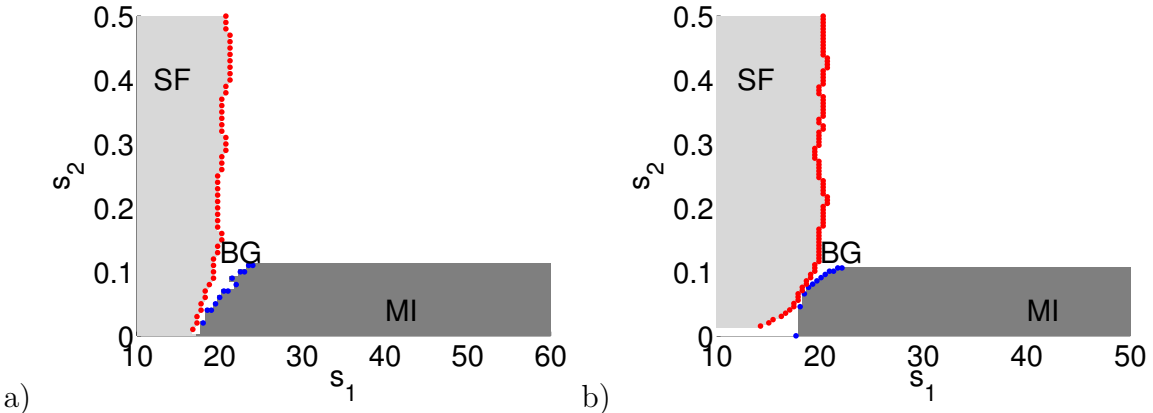


Figure 6.16: Phase diagram for the bi-chromatic quasi-periodic potential (6.1), where the symmetric Wannier functions were used, for fixed mean particle number of $\bar{n} = 1$ in dependence of the laser intensities s_1 and s_2 for a system with 10×10 sites (a) and 32×32 sites (b), which can be compared to the phase diagram determined on the basis of non-symmetric Wannier functions for the same system size and shown in Figure 6.6 b).

in the phase diagram (see Figure 6.4). This is true even though the width of the distribution of the tunneling rates is one order of magnitude smaller than that of the on-site energy. The influence of disordered inter-particle interaction, however, is negligible, since its width remains four orders of magnitude below the critical disorder strength.

Moreover, in Chapter 5 we have found that each scenario, where only one BH parameter is disordered, yields different characteristic features in the phase diagram. Having this in mind, the influence of tunneling disorder becomes obvious in the phase diagram of the quasi-periodic potential in dependence of the BH parameters. The transition lines, shown in Figure 6.8, deviate from pure box distributed on-site disorder, which are shown in Figure 4.4. In the quasi-periodic case the SF region is smaller, while the BG and the MI regions cover a larger region. In the phase diagram in dependence of JZ/U and $(\mu - \epsilon)/U$, shown in Figure 6.11, we find individual BG regions, which are separated by SF regions. This, however, is a unique feature exclusively occurring in systems with disordered tunneling rates (see Figure 5.2). Consequently one has to be aware that experimental setups using a bi-chromatic quasi-period potential, as for example [3], should be expected to produce a phase diagram that is qualitatively very different from predictions of the disordered BH model with exclusively on-site disorder. Moreover, it is important to know, that in a bi-chromatic quasi-periodic potential it is not possible to study on-site disorder exclusively, since as becomes evident from Figure 6.7, for growing intensity of the second laser s_2 , the width of the disorder distribution of both the on-site and the tunneling rate increase simultaneously.

7 Quasi-periodic structures due to cavity backaction

The interplay of a regular optical lattice and an additional optical field produced by photons inside a cavity will be discussed in this chapter. The bosons are tightly confined in an optical lattice produced by lasers of some wave length λ_0 . An optical dipole transition of the bosons is driven by an additional laser leading to scattering of photons into the cavity field, according to the geometry shown in Figure 7.1. These photons themselves in turn form an optical potential for the atoms, which is periodic with the wave length λ given by the cavity. This optical pattern, however, depends on the local particle density in the system. In situations, in which particle fluctuations are negligible, as for example deep in the MI regime of the main optical lattice, the scattering of photons into the cavity field is suppressed and the atoms experience only the regular optical lattice with wave length λ_0 . With the onset of particle fluctuations photons are scattered into the cavity field and the atoms experience the overlap of the main lattice produced by the laser with wave length λ_0 and the optical field of the photons with the cavity wave length λ . This interplay can be described by a BH model with correlated disorder in the on-site energies [5, 6]. As we will see in this chapter for commensurate wave lengths there are two classes of phase diagrams, one for odd and one for even ratios of the two wave lengths. For odd ratios the so-called SS phase occurs, where the system is in the SF phase and additionally the particle densities show a checker board like pattern. For incommensurate wave lengths the behavior is much richer and not only the SS phase, but also the BG phase and a variety of SF phases occur in the phase diagram.

7.1 The System

For a systematic description of this system we assume the ultracold bosons to be tightly confined in the lowest band of a regular 2D optical lattice in the x - z -plane, originated by a standing-wave potential

$$V(x, z) = V_0 (\cos^2(k_0 x) + \cos^2(k_0 z)) , \quad (7.1)$$

where $V_0 < 0$ is the potential depth and $k_0 = 2\pi/\lambda_0$ the wave number. The atomic motion is restricted to the x - z -plane, as motion in the y -direction is assumed to be frozen out. This potential (7.1) is regular and periodic with the lattice constant $a = \pi/k_0$, defining the location of lattice sites at its maxima.

In the considered setup the atoms are additionally confined within an optical resonator,

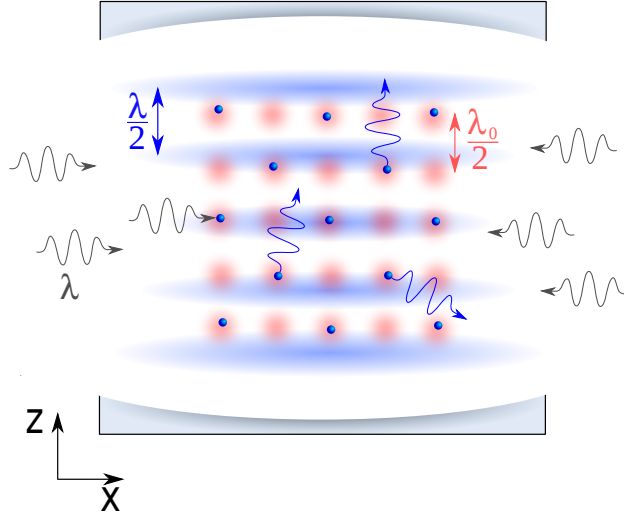


Figure 7.1: The atoms are tightly confined in a regular optical lattice, whose minima are shown in red and which is produced by lasers of the wave length λ_0 . A laser, shown in grey, drives an optical dipole transition of the bosons leading to coherent scattering of photons into the cavity mode. These cavity photons, shown in blue, form an additional optical lattice for the bosons at wave length λ . Therefore, the atoms, which are confined in the regular optical lattice with wave length λ_0 , also feel the optical potential of wave length λ . The interplay of both wave lengths leads to a dynamical on-site potential for the atoms.

which possesses a standing-wave mode at wave number $k = 2\pi/\lambda$ coupling quasi-resonantly to an atomic dipolar transition at frequency ω_0 . We assume that a laser field propagating along the x -direction drives the same optical transition from the side, such that the atoms scatter photons into the cavity along the z -direction, as depicted in Figure 7.1. In specific limits the cavity field dynamics adiabatically follows the atomic density dynamics; details are discussed in [5, 6], where it is argued that this regime is reached for the parameters of the experimental setup of [7, 8]. If this holds, the system is described by the Hamiltonian [5, 6]

$$\hat{H}_{\text{sys}} = \hat{H}_{\text{BH}} + \hat{H}_{\text{laser}} + \hat{H}_{\text{cav}}, \quad (7.2)$$

where \hat{H}_{BH} is the Bose-Hubbard Hamiltonian (2.43) as introduced in Chapter 2, \hat{H}_{laser} is the potential term due to the transverse laser field, and \hat{H}_{cav} is the long-range potential along the z -direction mediated by the cavity photons the atoms are interacting with. The specific form of these Hamiltonians will be discussed in the following section. In this chapter we will evaluate the phase diagram of this model for various relations of the two wave lengths λ and λ_0 .

7.2 The Bose-Hubbard model with long-range photon-mediated interactions

Let us now have a closer look on the three parts of the Hamiltonian (7.2). The first term is the BH Hamiltonian (2.43), which describes bosons in a regular 2D $L \times L$ lattice and has already been discussed in Chapter 2. The three different energy scales in this model, namely the on-site energy ϵ_i , the tunneling rate J and the inter-particle interaction U can be computed with the help of the Wannier functions $W_i(\vec{r})$ for the potential (7.1) according to Equation (2.56).

The Hamiltonian \hat{H}_{laser} results from a sinusoidal potential along the x -direction of the form $V_1 \cos(kx)$. Its depth V_1 is a tunable parameter, which is smaller than the gap between the lowest and the second band of the optical lattice. In this limit the decomposition into the lowest band Wannier functions $W_i(\vec{r})$ is consistent, and the corresponding term reads

$$\hat{H}_{\text{laser}} = V_1 \sum_i J_0^{(i)} \hat{n}_i, \quad (7.3)$$

with the coefficients

$$J_0^{(i)} = \int d\vec{r} W_i(\vec{r}) \cos^2(kx) W_i(\vec{r}) \quad (7.4)$$

and the amplitude $V_1 = \hbar\Omega^2/\Delta_a$. This Hamiltonian is diagonal and will lead to a site dependent correction of the on-site energy.

Cavity backaction is now constituted by the Hamiltonian

$$\hat{H}_{\text{cav}} = \hat{\delta}(\hat{\mathbf{n}}) L^2 \hat{\Phi}^2 \quad (7.5)$$

with $\hat{\mathbf{n}} = \{\hat{n}_1, \dots, \hat{n}_{L^2}\}$, which gives rise to selfordering. The operator

$$\hat{\Phi} = \frac{1}{L^2} \sum_i Z_0^{(i)} \hat{n}_i \quad (7.6)$$

depends on the particle number \hat{n}_i at each site and on the site dependent function

$$Z_0^{(i)} = \int d\vec{r} W_i(\vec{r}) \cos(kz) \cos(kx) W_i(\vec{r}), \quad (7.7)$$

which assumes values between 1 and -1 . The coefficient

$$\hat{\delta}(\hat{\mathbf{n}}) = \frac{\hbar s_0^2}{\hat{\delta}_{\text{eff}}^2 + \kappa^2} \hat{\delta}_{\text{eff}} \quad \text{with} \quad \hat{\delta}_{\text{eff}} = \delta_c + \frac{u_0}{L^2} \sum_i Y_0^{(i)} \hat{n}_i \quad (7.8)$$

and

$$Y_0^{(i)} = \int d\vec{r} W_i(\vec{r}) \cos^2(kz) W_i(\vec{r}), \quad (7.9)$$

depends on the particle density at each site. Notice that the values of the functions $J_0^{(i)}$, $Y_0^{(i)}$, $Z_0^{(i)}$ as well as the BH parameters ϵ , J , U depend on the potential depth of the

optical lattice V_0 , since the Wannier functions $W_i(\vec{r})$ change their shape according to potential (7.1). Thus, in this model these functions and the BH parameter are dependent parameters.

Both Hamiltonians \hat{H}_{laser} as well as \hat{H}_{cav} lead to a diagonal contribution to the BH Hamiltonian (2.43), such that the on-site energies $\epsilon_i = \epsilon + \delta\hat{\epsilon}_i$ become site dependent with the dynamic potential

$$\delta\hat{\epsilon}_i = V_1 J_0^{(i)} - \hat{\delta}(\hat{\mathbf{n}}) \hat{\Phi} Z_0^{(i)}. \quad (7.10)$$

While the site independent BH parameters ϵ , J and U are defined at the lattice sites given by the optical lattice with wave length λ_0 , the dynamic potential, which describes the influence of the cavity and the laser, is periodic with wave length λ . Consequently the setup shown in Figure 7.1 is described by the Hamiltonian

$$\hat{H} = -\hat{\delta}(\hat{\mathbf{n}}) L^2 \hat{\Phi}^2 + \sum_i \left(\epsilon - \mu + V_1 J_0^{(i)} \right) \hat{n}_i + \frac{U}{2} \sum_i \hat{n}_i (\hat{n}_i - 1) - J \sum_{\langle i,j \rangle} \left(\hat{a}_i^\dagger \hat{a}_j + \hat{a}_i \hat{a}_j^\dagger \right). \quad (7.11)$$

The static on-site potential $V_1 J_0^{(i)}$, describing the influence of the laser, is independent of the local particle numbers $\hat{\mathbf{n}}$ and its amplitude $V_1 = \hbar\Omega^2/\Delta_a$ is fixed. It induces a regular 2D stripe pattern, which is periodic in x -direction and constant in z -direction and exists in the whole parameter regime. However, the dynamic potential $\hat{\delta}(\hat{\mathbf{n}}) \hat{\Phi} Z_0^{(i)}$, describing the influence of the cavity, forms a 2D periodic pattern, whose amplitude depends not only on the absolute number of bosons, but rather on the distribution of bosons within the lattice and thereby introduces a long range interaction. Its amplitude is governed by $\hat{\delta}(\hat{\mathbf{n}})$ on the one hand, which depends on the particle numbers, and on the other hand by the operator $\hat{\Phi}$. According to Equation (7.6), the operator $\hat{\Phi}$ is the component of the Fourier transform of the particle density $\{\hat{n}_i\}$ at a given wave vector k . If this component is positive, the atoms coherently scatter photons at wave length λ into the cavity mode. Therefore, $\hat{\Phi}$ describes the occupation number of photons in the cavity. We will see, that there are parameter ranges in which coherent scattering of photons into the cavity is supported ($\hat{\Phi} > 0$), and others in which this process is suppressed ($\hat{\Phi} = 0$). The photons in the cavity mode themselves again form an optical potential for the atoms, which is described by the first part of Hamiltonian (7.11). The energy $-\hat{\delta}(\hat{\mathbf{n}}) L^2 \hat{\Phi}^2$ depends on the square of the occupation number $\hat{\Phi}$ of the cavity mode and thus is non-linear in the particle numbers \hat{n}_i . We will see, that for specific ratios of the wave length of the optical potential λ_0 and the cavity mode λ this dynamic potential gives rise to the formation of a checker board pattern in the local densities, where sites are occupied by an alternating number of particles. The occurrence of such a checker board pattern is indicated by the structure factor

$$S(\vec{k}) = \frac{1}{L^2} \sum_{i,j} \hat{n}_i \hat{n}_j e^{-ik(\vec{r}_i - \vec{r}_j)}, \quad \vec{k} = \frac{2\pi}{L} l, \quad \vec{r}_i = ai \quad (7.12)$$

with $i = (i_x, i_z)$ and $l = (l_x, l_z)$. This function shows a peak at the coordinates (π, π) , if the checker board pattern, which has a period of two sites, occurs in the density distribution.

The structure factor $S(\vec{k})$ equals the absolute value of the Fourier transform

$$F(\vec{k}) = \sum_i \hat{n}_i e^{-i\vec{k}\vec{r}_i} / L \quad (7.13)$$

of the density distribution. For wave length ratios, for which the checker board pattern can be established, the occurrence of coherent scattering into the cavity ($\hat{\Phi} > 0$) is accompanied by the appearance of the peak of the structure factor at (π, π) , which means that $S(\pi, \pi) > 0$. Thus, the value $S(\pi, \pi)$ is proportional to $\hat{\Phi}$ and can serve as an order parameter for the appearance of the checker board pattern in the particle density. SF phases in which the particle density shows such a pattern and thus show positive values of $S(\pi, \pi)$, were referred to as SS phases [111–113]. Notice that, the order parameter $S(\pi, \pi)$ directly occurs in the first part of Hamiltonian (7.11). Since the structure factor is accessible in experiments via time-of-flight techniques, the order parameter $S(\pi, \pi)$ is also an observable for the identification of the checker board pattern. The main lattice is defined by the maxima of the red detuned regular potential (7.1) with lattice sites at $x = i_x a$ and $z = i_z a$ with the lattice constant $a = \lambda_0/2$. The values of the site independent BH parameters ϵ , J and U are defined at each lattice site as the overlap integral of the Wannier functions $W_i(\vec{r})$ with the kinetic and potential part of the Hamiltonian, according to Equation (2.56). The dynamic potential $\delta\hat{\epsilon}_i$ introduces a correlated pattern modulated by a different wave length $\lambda = 2\pi/k$. This pattern is governed by the values of

$$\cos(kx) = \cos\left(i_x \pi \frac{\lambda_0}{\lambda}\right) \text{ and } \cos(kz) = \cos\left(i_z \pi \frac{\lambda_0}{\lambda}\right) \quad (7.14)$$

at the lattice sites occurring in the functions $J_0^{(i)}$, $Z_0^{(i)}$ and $Y_0^{(i)}$ as given in equations (7.4), (7.7) and (7.9). Thus, the ratio λ_0/λ of both wave lengths influences the behavior of the system fundamentally and will lead to a variety of different phase transitions.

The BH Hamiltonian discussed here can be realized in experiment [7,8], where ^{87}Rb atoms with mass $m_{\text{Rb}} = 1.45 \cdot 10^{-25} \text{ kg}$ are used. Therefore it is useful to recall all experimental parameters: The optical lattice is periodic with the wave length $\lambda_0 = 785 \text{ nm}$. The cavity field ω_C is characterized by wave number $k = 2\pi/\lambda$ and a linewidth of $\kappa = 2\pi \times 1.3 \text{ MHz}$ and a wave vector pointing in z -direction. While the difference between the laser frequency and the cavity field is denoted by $\delta_c = \omega_C - \omega_L = 5\kappa$, the difference between the laser and the optical lattice frequency is given by $\Delta_a = \omega_L - \omega_0$. The Rabi frequency of the cavity is denoted by g_0 and the Rabi frequency of the coherent coupling between the dipolar transition and a standing-wave laser along the x -direction by Ω . The frequency $u_0 = g_0^2 L^2 / \Delta_a = 237\kappa$ scales with the depth of the intra cavity potential generated by a single photon. The Raman scattering amplitude with which a single photon is scattered by a single atom between cavity and laser mode is denoted by $s_0 = g_0 \Omega L / \Delta_a = 0.15\kappa$ for $L = 100$. The potential depth of the pump laser is finally given by $V_1 = \hbar \Omega^2 / \Delta_a = \hbar s_0^2 / u_0$ [6, 77, 79].

7.3 Commensurate lattices

In this section our purpose is to study commensurate ratios of the wave lengths λ_0 , determining the position of the lattice sites and λ , describing the dynamic potential $\delta\hat{\epsilon}_i$. We will focus on the cases

$$\lambda = \frac{\lambda_0}{l}, \quad \text{with } l = 1, 2, \quad (7.15)$$

which means that the distance between the lattice sites $a = \lambda_0/2$ is larger than the beating of the dynamic potential $\delta\hat{\epsilon}_i$ given in Equation (7.10).

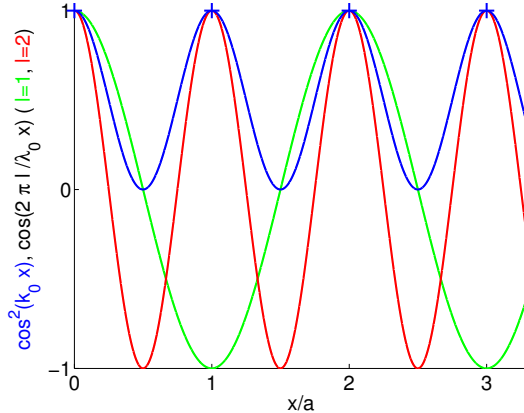


Figure 7.2: The function $\cos^2(k_0 x)$ (blue) defines the lattice sites at $x = i_x a$, which are marked with crosses. The functions $\cos(2\pi l/\lambda_0 x)$, shown for $l = 1$ (green) and $l = 2$ (red), represent the period of the dynamic potential $\delta\hat{\epsilon}_i$ as given in Equation (7.10).

Due to the functions $J_0^{(i)}$, $Y_0^{(i)}$ and $Z_0^{(i)}$, given in equations (7.4), (7.9) and (7.7), the values of the dynamic potential at lattice sites $(x, z) = (i_x, i_z) a$ with the lattice constant $a = \lambda_0/2$ are governed by the function

$$\cos(kx) = \cos\left(i_x \pi \frac{\lambda_0}{\lambda}\right) = \cos(i_x \pi l) = \begin{cases} (-1)^{i_x} & \text{for } l \text{ odd} \\ 1 & \text{for } l \text{ even} \end{cases} \quad (7.16)$$

in x -direction; an analogous dependency holds for the z -direction. In Figure (7.2) the function $\cos^2(k_0 x)$ is shown in blue and the lattice sites at $x = i_x a$ at the maxima of this function are marked with crosses. The function $\cos(kx)$ with $\lambda = \lambda_0/l$ is shown in green ($l = 1$) and red ($l = 2$). For even l this function is always positive in the vicinity of the lattice sites, while for odd l the sign changes at each site. As $J_0^{(i)}$ and $Y_0^{(i)}$ are proportional to $\cos^2(kx)$ and the setup is symmetric in x - and z -direction, they have the same value at each lattice site. Also the absolute value of $Z_0^{(i)}$ is identical at each site. As a result these functions fulfill

$$J_0^{(i)} = Y_0^{(i)} = Y(V_0) \text{ and } Z_0^{(i)} = (-1)^{i_x i_z l} Z(V_0), \quad (7.17)$$

where the values $Y(V_0)$ and $Z(V_0)$ are site independent, but vary as a function of the depth V_0 of the potential (7.1), since the Wannier functions $W_i(\vec{r})$ change their shape

	N_{SF}	P	$\hat{\Phi}$
MI	= 0	= 0	= 0
MICB	= 0	= 0	> 0
SF	> 0	= 1	= 0
SS	> 0	= 1	> 0

Table 7.1: For commensurate wave lengths the four occurring phases can be identified by the number of SF sites N_{SF} , the percolation probability P of SF clusters and the occupation number of photons in the cavity $\hat{\Phi}$.

according to this potential. In general these functions are smaller than one, since, according to the equations (7.4), (7.7) and (7.9), they are given by the overlap integral of the square of the Wannier function with a cosine. Simply setting them to one is equivalent to approximating the Wannier function by a δ -function, which is far away from a realistic description.

For even values of l the dynamic potential

$$\delta\hat{\epsilon}_i = V_1 Y(V_0) - \hat{\delta}(\hat{\mathbf{n}}) Z(V_0)^2 \hat{n} \quad (7.18)$$

has the same value at each site and acts like a shift of the chemical potential μ/U , which is different for every value of the tunneling rate JZ/U , as it depends on V_0 . The situation changes for odd values of l , since then, the dynamic potential

$$\delta\hat{\epsilon}_i = V_1 Y(V_0) - (-1)^{i_x i_z} \hat{\delta}(\hat{\mathbf{n}}) \hat{\Phi} Z(V_0) \quad (7.19)$$

changes its sign at each lattice site. This gives rise to the formation of a checker board like density distribution in regions, where the coherent scattering into the cavity is supported ($\hat{\Phi} > 0$). The occurrence of the checker board pattern is accompanied by a positive value of the order parameter $S(\pi, \pi)$. The static potential $V_1 Y(V_0)$ is a function of V_0 and shifts the chemical potential μ/U . This is why there exist two different classes of phase diagrams, one for odd and one for even values of l .

In the following we study the phase diagram of this system in dependence of the chemical potential μ/U and the tunneling rate JZ/U . The phases of the system can be identified by the number of SF sites N_{SF} , the percolation probability P of SF clusters and the occupation number of photons in the cavity $\hat{\Phi}$ and are summarized in Table 7.1:

MI phase: Each lattice site is occupied by an integer number of particles, which means that all sites are MI sites ($N_{SF} = 0$). This phase occurs in parameter regions, where no checker board pattern is established ($\hat{\Phi} = 0$) and the system is equivalent to an ordered BH model. Since there exists a energy gap in the excitation spectrum, tunneling of particles is suppressed, the system is not compressible and its ground state is not coherent.

MICB phase: This phase occurs in parameter regions, where coherent scattering into the cavity is supported ($\hat{\Phi} > 0$) and the dynamic potential $\hat{\delta}(\hat{\mathbf{n}}) \hat{\Phi} Z_0^{(i)}$ introduces a checker board pattern. The local density shows sites occupied by one particle, which are surrounded by empty sites. The structure factor $S(\vec{k})$, given in Equation (7.12), indicates

the formation of the checker board pattern by showing a peak at $\vec{k} = (\pi, \pi)$. Since the occurring particle numbers are integer, the system consists only of MI sites ($N_{SF} = 0$) and shows the same features as the MI phase.

SF phase: This phase is characterized by the occurrence of a least one percolating SF cluster ($P = 1$). In this phase all sites are occupied by the same non-integer number, forming a huge percolating SF cluster. Within these SF sites, particle tunneling is favorable and the ground state is coherent. Thus, the system is compressible and coherent.

SS phase: The system shows all features of the SF phase, especially the occurrence of a percolating SF cluster ($P = 1$). Additionally, the dynamic potential $\hat{\delta}(\hat{n})\hat{\Phi}Z_0^{(i)}$ introduces a checker board pattern and the particle number alters between two non-integer values. Thus, the structure factor $S(\vec{k})$ shows a peak at $\vec{k} = (\pi, \pi)$.

Let us now discuss the two classes of phase diagrams separately.

7.3.1 Odd ratios (l odd)

For odd values of l the function $\cos(kx)$ changes its sign at each site. In this case the static potential $V_1Y(V_0)$ causes a shift of the chemical potential. However the dynamic potential $(-1)^{ix}\hat{\delta}(\hat{n})\hat{\Phi}Z(V_0)$ establishes a checker board pattern in parameter regions, where the cavity is populated ($\hat{\Phi} > 0$). In regions where the cavity mode is empty ($\hat{\Phi} = 0$) the sites are occupied by the same number of particles.

In the limit of zero tunneling rates ($J = 0$), the upper and lower bounds of the Mott-lobes at the μ -axis can be determined analytically. For this purpose we distinguish the particle number at even n_e from those at odd sites n_o . According to the Hamiltonian (7.11) the energy per site for a checker board configuration ($n_e = n$ and $n_o = n - 1$) is given by

$$\frac{E_n^{\text{CB}}}{L^2} = -\frac{\hat{\delta}(n)Z^2}{4} + (\epsilon - \mu + V_1Y) \frac{2n - 1}{2} + \frac{U}{2}(n - 1)^2 \quad (7.20)$$

with $\hat{\Phi} = Z/2$. For a MI configuration ($n_e = n_o = n$) where $\hat{\Phi} = 0$ the energy per site reads

$$\frac{E_n^{\text{MI}}}{L^2} = (\epsilon - \mu + V_1Y)n + \frac{U}{2}n(n - 1). \quad (7.21)$$

The energy gap $E_n^{\text{CB}} - E_n^{\text{MI}}$ vanishes for

$$\mu_-(n) = \frac{\hat{\delta}(n)Z^2}{2} + \epsilon + V_1Y + U(n - 1), \quad (7.22)$$

which defines the lower bound of the Mott-lobe, while the energy gap $E_{n+1}^{\text{CB}} - E_n^{\text{MI}}$ vanishes for

$$\mu_+(n) = -\frac{\hat{\delta}(n)Z^2}{2} + \epsilon + V_1Y + Un, \quad (7.23)$$

describing the upper bound of the Mott-lobes. Therefore, along the μ -axis there exists a row of MI regions between $\mu_-(n)$ and $\mu_+(n)$, which are separated from each other by

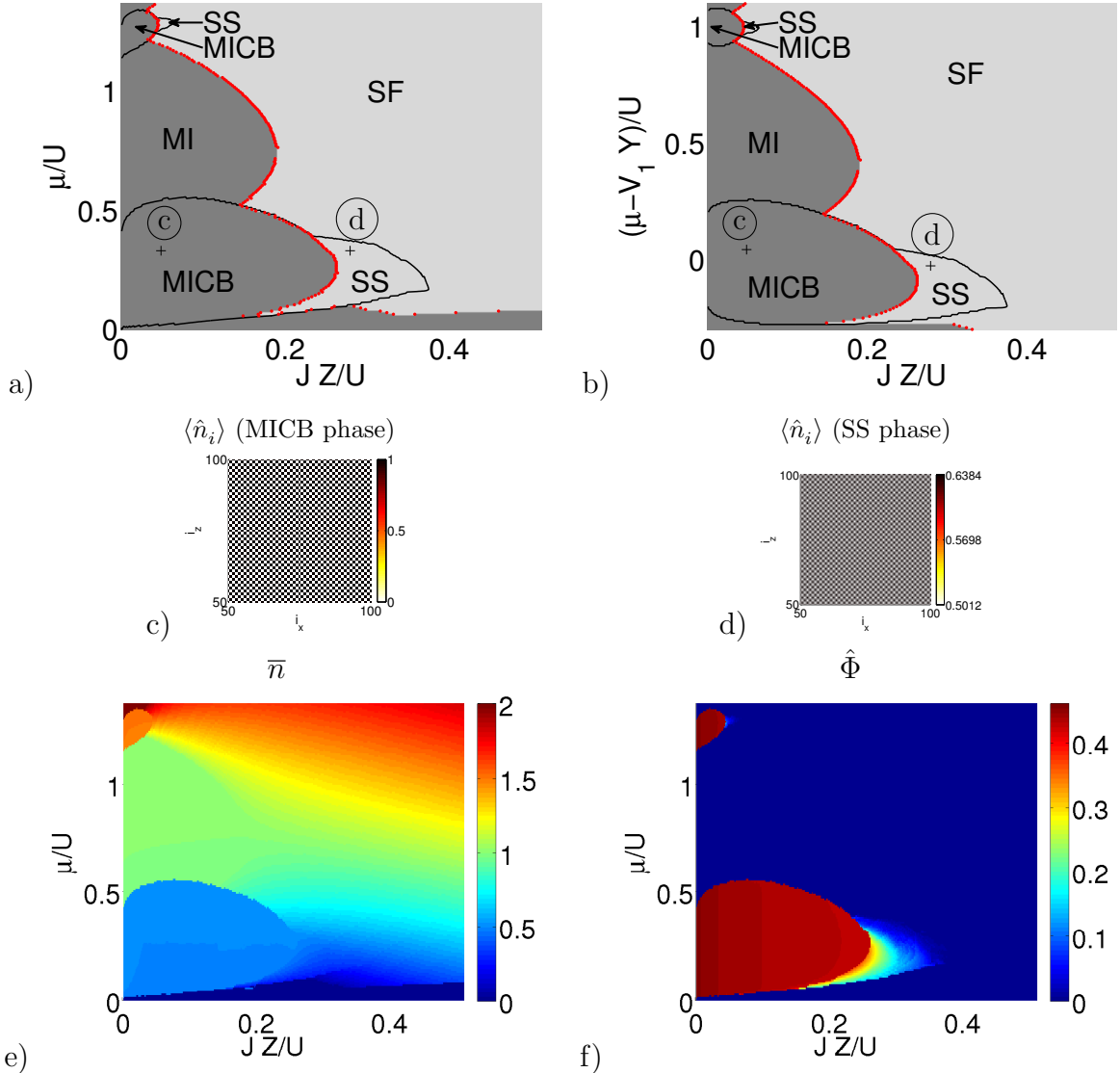


Figure 7.3: (a) and (b): The phase diagram for $\lambda = \lambda_0$ as a function of μ/U or rather $(\mu - V_1 Y)/U$ and JZ/U . The percolation line of the SF cluster is shown with red dots separating the MI from the SF region. Within the black lines there exists coherent scattering into the cavity ($\hat{\Phi} > 0$) and the dynamic potential forms a checker board pattern. The black crosses, which are labeled with the circled letter, mark the parameters chosen in Figure c) and d) showing the local boson occupation number $\langle \hat{n}_i \rangle$ for the parameters (c) $JZ/U = 0.0489$, $\mu/U = 0.3307$ and (d) $JZ/U = 0.2792$, $\mu/U = 0.3307$. (e) and (f): Mean particle number \bar{n} and occupation number of the cavity mode $\hat{\Phi}$.

a checker board region between $\mu_+(n)$ and $\mu_-(n+1)$. This pattern only occurs in the region, where $\hat{\delta}(n)$ fulfills the inequality

$$0 \leq \hat{\delta} \leq \frac{U}{Z^2}. \quad (7.24)$$

Above this threshold, for $\hat{\delta} \geq U/Z^2$, all Mott-lobes disappear, while below, for $\hat{\delta} \leq 0$, all CB regions vanish simultaneously. Thus, for small $\hat{\delta}$ only Mott-lobes exist, for intermediate $\hat{\delta}$ Mott-lobes and CB regions coexist, while for large $\hat{\delta}(n)$ only CB regions survive. The reader should notice that in this model $\hat{\delta}(n) \sim 1/n$ is inverse proportional to the particle number and thus is different for each Mott-lobe and CB region. As a result the Mott-lobes and CB regions do not disappear simultaneously but rather according to their specific value of $\hat{\delta}(n)$. For the parameters chosen in our simulations, $\hat{\delta}(n)$ always fulfills condition (7.24) and we consequently expect to observe the coexistence of Mott-lobes and CB regions.

The phase diagram, the mean particle number \bar{n} and the occupation number of the cavity field $\hat{\Phi}$ for $\lambda = \lambda_0$ are shown in Figure 7.3. In regions, where coherent scattering into the cavity is suppressed ($\hat{\Phi} = 0$), the phase diagram shows regular Mott-lobes with increasing integer particle number, which are shifted according to Equation (7.22) and (7.23). In between there are regions, where photons are coherently scattered into the cavity ($\hat{\Phi} > 0$) and the dynamic potential $\hat{\delta}(\hat{\mathbf{n}})\hat{\Phi}Z_0^{(i)}$ forms a checker board pattern, which is also visible in the particle density. In the MICB phase, occurring at half filling ($\bar{n} = 1/2$), an occupied site is surrounded by empty sites as shown in Figure 7.3 c). For larger tunneling rates JZ/U the transition to the SS region occurs, where the sites are alternatingly occupied by two different non-integer numbers of bosons, as shown in Figure 7.3 d). In the region around $\mu/U = 1.2$ another region of coherent scattering into the cavity occurs ($\hat{\Phi} > 0$), where we also observe the transition from the MICB region to the SS region.

7.3.2 Even ratios (l even)

For even values of l the function $\cos(kx)$ assumes a positive value in the vicinity of each lattice site and the functions $J_0^{(i)} = Y_0^{(i)} = Y(V_0)$ and $Z_0^{(i)} = Z(V_0)$ have the same positive value at each lattice site. Consequently, the influence of the dynamic potential $\delta\hat{\epsilon}_i$ reduces to a shift of the chemical potential μ/U , which depends on V_0 and thus is a function of the tunneling rate JZ/U . Since all sites have the same parameters, each lattice site is occupied by the same particle number $\hat{n}_i = n \forall i$. As a result the population of the cavity mode $\hat{\Phi} = Zn$, shown in Figure 7.4 d), is non-zero and positive in the whole parameter range. Therefore, the phase diagram consists of a row of shifted Mott-lobes, which are surrounded by a SF phase.

In the limit of zero tunneling rates ($J = 0$) the extension of the Mott-lobes along the μ/U -axis can be computed analytically. According to Hamiltonian (7.11) the energy per site is given by

$$\frac{E_n}{L^2} = -\hat{\delta}(n)Z^2n^2 + (\epsilon - \mu + V_1Y)n + \frac{U}{2}n(n-1) \quad (7.25)$$

and the energy gap $E_n - E_{n-1}$ vanishes for

$$\mu = Z^2 \left(\hat{\delta}(n)n^2 - \hat{\delta}(n+1)(n+1)^2 \right) + \epsilon + V_1Y + Un. \quad (7.26)$$

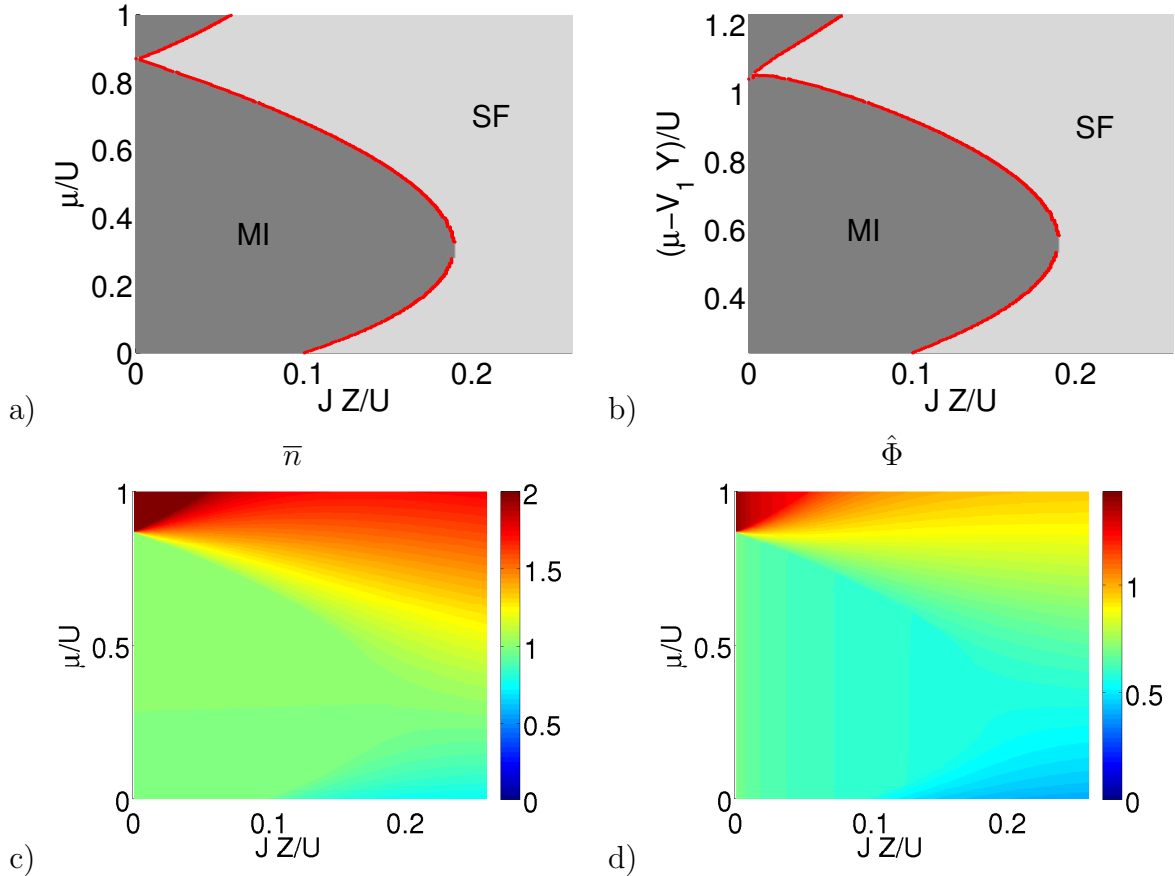


Figure 7.4: (a) and (b): The phase diagram for $\lambda = \lambda_0/2$ as a function of μ/U or rather $(\mu - V_1 Y)/U$ and JZ/U . The percolation line of the SF cluster is shown with red dots separating the MI from the SF region. (c) and (d): Mean particle number \bar{n} and occupation number of the cavity mode $\hat{\Phi}$.

For the ordered BH model the n -th Mott-lobe reaches from $\mu/U = n - 1$ to $\mu/U = n$. Here each Mott-lobe is shifted by the value

$$\Delta_\mu(n) = Z^2 \left(\hat{\delta}(n) n^2 - \hat{\delta}(n+1) (n+1)^2 \right) + \epsilon + V_1 Y, \quad (7.27)$$

which linearly depends on the particle number n , as $\delta(n)$ is inverse proportional to n . In the phase diagram for $l = 2$, shown in Figure 7.4 a), we find individual Mott-lobes, where each site is occupied by a fixed integer number of particles. Each Mott-lobe is shifted downwards by the amount $\Delta_\mu(n)$, which depends on n and varies as a function of the tunneling rate J , as it depends on the depth V_0 of the optical potential (7.1). The mean particle number \bar{n} increases with the chemical potential μ/U , as shown in Figure 7.4 c).

7.4 Incommensurate lattices

In the following we study the situation in which the wave length λ of the cavity field is a simple fraction of the one of the laser field λ_0 plus a small shift of $\epsilon_\lambda = 45$ nm according to

$$\lambda = \frac{\lambda_0}{l} + \epsilon_\lambda, \quad \text{with } l = 1, 2, 3. \quad (7.28)$$

In this situation the wave length λ_0 , which defines the position of the lattice sites at $(x, z) = (i_x, i_z) a$ with the lattice constant $a = \lambda_0/2$, is incommensurate with the wave length λ of the dynamic potential $\delta\hat{\epsilon}_i$, which is given in Equation (7.10). According to Equation (7.14) the values of the dynamic potential evaluated at the lattice sites in both spatial directions is governed by the function

$$\cos(kx) = \cos\left(\frac{i_x \pi l}{1+K}\right) = (-1)^{i_x l} \cos\left(i_x \pi l \frac{K}{1+K}\right) = (-1)^{i_x l} \cos\left(2\pi \frac{i_x}{i_p}\right), \quad (7.29)$$

where we used the geometric series $1/(1+K) = \sum_{r=0}^{\infty} (-K)^r$ with $K = l\epsilon_\lambda/\lambda_0$ as a small parameter. This function is a superposition of a factor, which changes sign at each lattice site for all odd values of l and a periodic envelope with a period of

$$i_p = \frac{2}{l^2} \frac{\lambda}{\epsilon_\lambda}. \quad (7.30)$$

The knots of the envelope are located at

$$i_r = (2r - 1) \frac{i_p}{4} = \frac{2r - 1}{2l^2} \frac{\lambda}{\epsilon_\lambda} \quad (7.31)$$

and are separated by

$$\frac{i_p}{2} = \frac{1}{l^2} \frac{\lambda}{\epsilon_\lambda} = \begin{cases} \frac{166}{9} \approx 18.44 & \text{for } l = 1 \\ \frac{175}{72} \approx 2.43 & \text{for } l = 2 \\ \frac{184}{243} \approx 0.76 & \text{for } l = 3 \end{cases} \quad (7.32)$$

lattice sites. As an example the function (7.29) and its envelope are shown in Figure 7.5 for $l = 1$.

Since the function $J_0^{(i)}$, as given in Equation (7.4), is proportional to $\cos^2(kx)$, it shows a periodic stripe structure in x -direction with the period $i_p/2$. The function $Z_0^{(i)}$ is proportional to $\cos(kx)\cos(kz)$, as given in Equation (7.7), and also shows a periodic pattern with the same period $i_p/2$, whose knots are located along the lattice sites (i_r, i_r) . For odd l this function additionally changes its sign at each site. Therefore, the dynamic potential $\delta\hat{\epsilon}_i$, as given in Equation (7.10), establishes two characteristic pattern: The static potential introduces a stripe structure, which exists in the whole parameter range since V_1 is fixed by experimental parameters [7,8]. The dynamic potential, which appears only in regions, where the coherent scattering of photons into the cavity is supported ($\hat{\Phi} > 0$), shows a 2D periodic pattern, which changes its sign at each site for odd l and thus gives

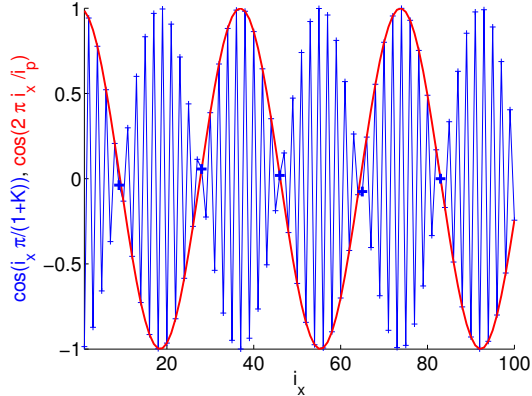


Figure 7.5: The function $\cos(i_x \pi / (1 + K))$, shown in blue, and its envelope $\cos(2\pi i_x / i_p)$, shown in red, according to Equation (7.29) for $l = 1$. The bold blue crosses mark the knots of $\cos(i_x \pi / (1 + K))$.

rise to the formation of a checker board pattern in the density profiles.

This interplay of the optical lattice with wave length λ_0 on the one hand, and the field due to the photons in the cavity, depending on λ , on the other hand, leads to the occurrence of different phases, which are summarized in Table 7.2:

MI phase: Each lattice site is occupied by an integer particle number, which means that all sites are MI sites ($N_{SF} = 0$). This phase occurs in parameter regions, where coherent scattering of photons into the cavity is suppressed ($\hat{\Phi} = 0$). Since there exists an energy gap in the excitation spectrum, tunneling of the particles is suppressed and the system is not compressible and its ground state not coherent.

BG phase: This phase occurs in parameter regions, where coherent scattering into the cavity is supported ($\hat{\Phi} > 0$) and the dynamic potential $\delta(\hat{n}) \hat{\Phi} Z_0^{(i)}$ introduces a checker board pattern for odd l . The local density shows a mixture of sites which are occupied by an integer particle number (MI sites) and non-integer particle number (SF sites) ($N_{SF} > 0$). The system consists of MI sites and not percolating, compressible SF islands, in which phase coherence occurs locally. This situation is analogous to the BG phase as it appears in the disordered BH model [2, 4]. In this phase the system is already compressible, due to the compressible SF islands, but long-range coherence is still lacking, since disconnected SF island cannot establish phase coherence.

SF phase: This phase is characterized by the occurrence of at least one percolating SF cluster and occurs in parameter regions, where coherent scattering into the cavity is suppressed ($\hat{\Phi} = 0$). Before the percolation, isolated SF clusters locally form coherent and compressible islands in the background of MI sites. With the percolation of one of these SF clusters local properties of the SF sites become globally relevant leading to a real SF system, which is compressible and shows long-range coherence. The behavior of the whole system is now governed by the percolating SF cluster. Due to the stripe structure introduced by the static potential $V_1 J_0^{(i)}$, there exists a preferred direction of percolation. Therefore, we distinguish between the **SF_X** and the **SF_Z** phase according to the direction of the percolation, which is described by the percolation probability P_X and P_Z . In these

	N_{SF}	P_X	P_Z	$\hat{\Phi}$
MI	= 0	= 0	= 0	= 0
BG	> 0	= 0	= 0	> 0
SF	> 0	= 1	= 1	= 0
SF _X	> 0	= 1	= 0	= 0
SF _Z	> 0	= 0	= 1	= 0
SS	> 0	= 1	= 1	> 0
SS _X	> 0	= 1	= 0	> 0
SS _Z	> 0	= 0	= 1	> 0

Table 7.2: For incommensurate wave lengths the occurring phase can be identified by the number of SF sites N_{SF} , the percolation probabilities P_X and P_Z corresponding to the direction of percolation of the SF clusters and the occupation number of photons in the cavity $\hat{\Phi}$.

phases the system is compressible in one direction, but not yet in the other direction. In the SF phase the percolation occurs in both directions ($P_X = P_Z = 1$), which means that the system is compressible in any direction.

SS phase: The system shows all features of the SF phase, especially the occurrence of percolating SF clusters. Here the dynamic potential $\hat{\delta}(\hat{n})\hat{\Phi}Z_0^{(i)}$ introduces a pattern, which is a superposition of a checker board pattern for odd l and a periodic function with period i_p , according to Equation (7.31). The particle density in some regions shows a checker board pattern, while along the knots of the function neighboring sites have similar values. We distinguish between SS, SS_X and SS_Z according to the direction of the occurring percolation. The occurrence of the checker board pattern in the local densities is accompanied by the appearance of a peak of the structure factor $S(\vec{k})$ at $\vec{k} = (\pi, \pi)$. Phases, showing such a pattern and positive values of $S(\pi, \pi)$, are referred to as SS phases [111–113].

7.4.1 Phase diagram for $\lambda = \lambda_0 + \epsilon_\lambda$

In the first case the mode of the cavity λ and the laser field λ_0 are slightly shifted off resonance by ϵ_λ . This system has already been studied in [6] with the help of 1d quantum Monte-Carlo techniques and 2D LMF theory on the basis of global order parameters, as introduced in Section 3.1. As we have seen in Section 3.3.1 the absence of a precise kink in the order parameters necessitated the introduction of a new criterion for the phase transitions based on local properties of the system, as done in Chapter 4. This LMF cluster analysis is the fundamental criterion for all phase diagrams discussed in this thesis.

The phase diagram obtained from 2D LMF cluster analysis [2, 4] for this model is shown in Figure 7.6 a), the mean particle number \bar{n} in g) and the photon occupation number $\hat{\Phi}$ of the cavity field in h). The occupation number $\hat{\Phi}$ of the cavity field shows a precise border between a region in which scattering into the cavity is supported ($\hat{\Phi} > 0$) and another

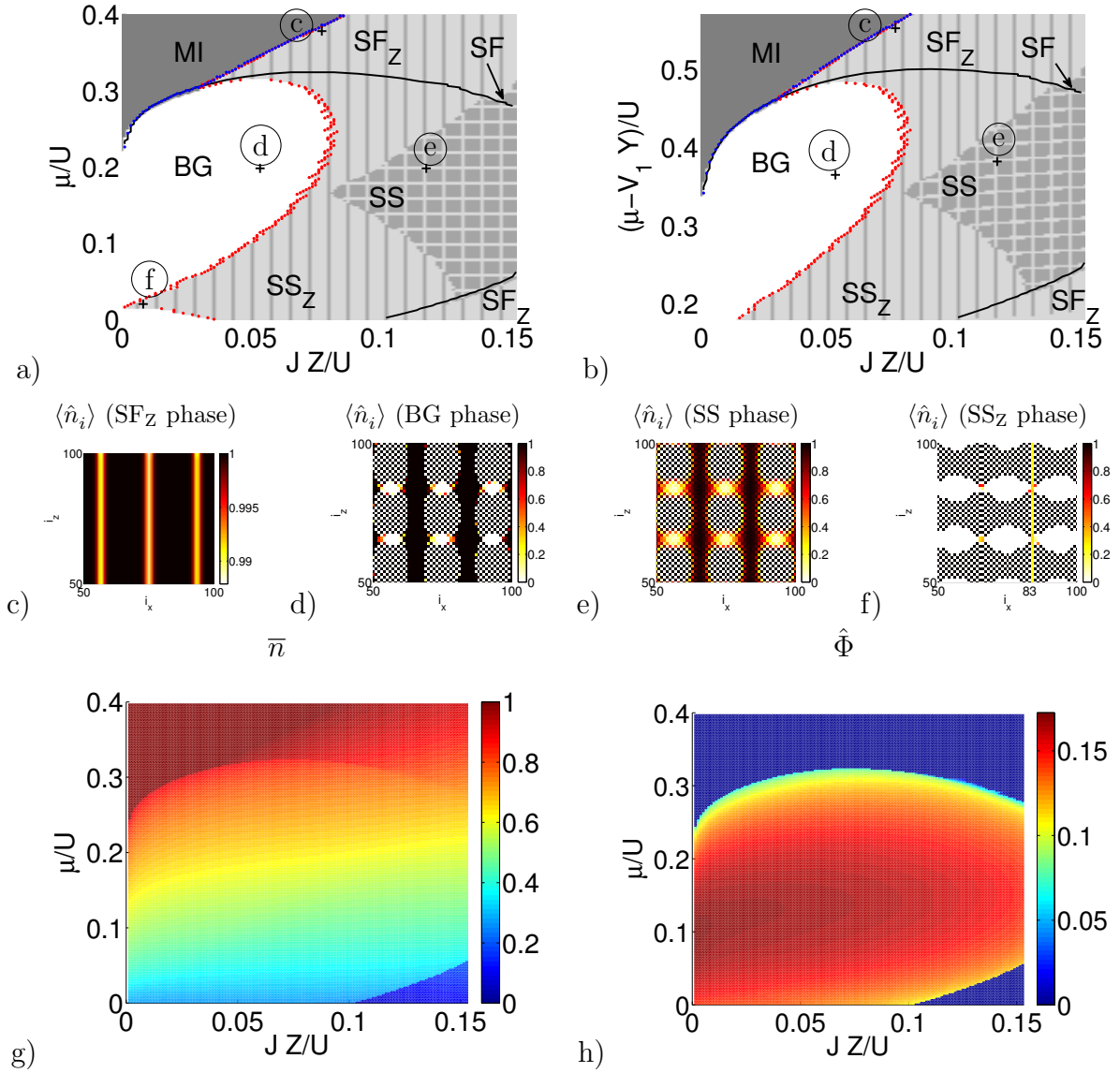


Figure 7.6: (a) and (b): The phase diagram for $\lambda = \lambda_0 + \epsilon_\lambda$ as a function of μ/U or rather $(\mu - V_1 Y)/U$ and JZ/U , where Y is the mean value of $J_0^{(i)}$. The border of the MI region is shown with blue dots and marks the appearance of SF sites. The border of the SF region, shown in red, marks the percolation of the SF cluster. Within the black line there exists coherent scattering into the cavity ($\hat{\Phi} > 0$) and the dynamic potential forms a checker board pattern. The black crosses, which are labeled with the circled letter, mark the parameters chosen in Figure c), d), e) and f) showing the local boson occupation number $\langle \hat{n}_i \rangle$ for the parameters (c) $JZ/U = 0.0777$, $\mu/U = 0.378$, (d) $JZ/U = 0.0537$, $\mu/U = 0.198$, (e) $JZ/U = 0.1184$, $\mu/U = 0.198$ and (f) $JZ/U = 0.0081$, $\mu/U = 0.02$. (g) and (h): Mean particle number \bar{n} and occupation number of the cavity mode $\hat{\Phi}$.

in which this scattering is suppressed ($\hat{\Phi} = 0$). This border is shown as a black line in the phase diagram. For large chemical potential μ/U the cavity is not occupied ($\hat{\Phi} = 0$) and thus the dynamic potential $\delta\hat{\epsilon}_i$ consist only of the static potential $V_1 J_0^{(i)}$, introducing

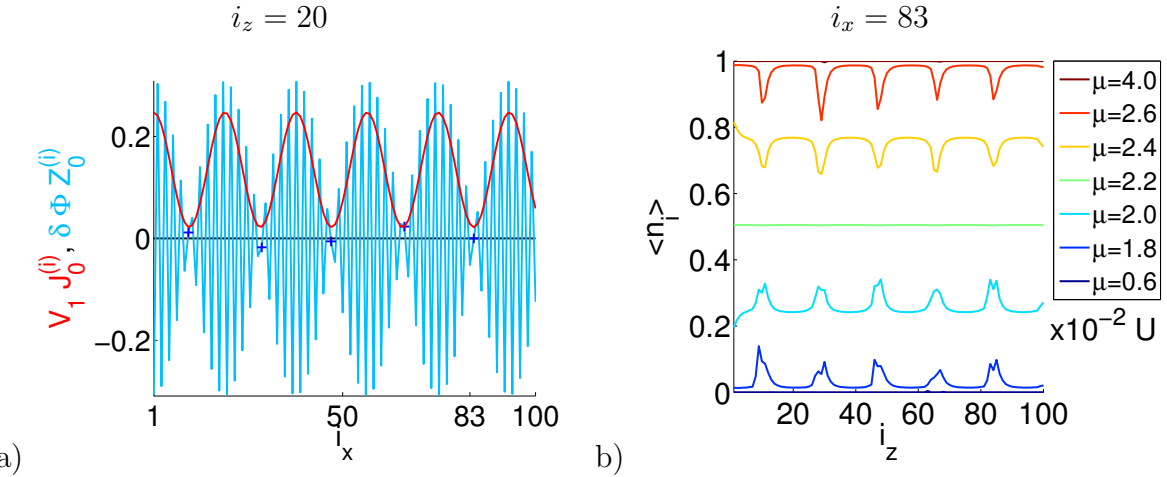


Figure 7.7: (a): The first (red) and the second (blue) part of the dynamic potential $\delta\hat{\epsilon}_i$ for $i_z = 20$ corresponding to the situation of Figure 7.6 f) for $JZ/U = 0.0081$ and $\mu/U = 0.02$. The dark blue crosses mark the value of $\hat{\delta}(\hat{\mathbf{n}}) \hat{\Phi} Z_0^{(i)}$ at the minima of $V_1 J_0^{(i)}$. At the site index $i_x = 83$ the dynamic potential becomes zero at the minimum static potential. (b): The local particle number $\langle \hat{n}_i \rangle$ at the site index $i_x = 83$ in dependence of i_z is shown for increasing chemical potential μ/U .

a stripe structure with period $i_p/2$. In this region a phase transition from the MI phase to the SF_Z phase occurs. The density distribution right after the percolation shows regular stripes with period $i_p/2$ at the minima of the dynamical potential $\delta\hat{\epsilon}_i$ as visible in Figure 7.6 c). Notice that, the value of the dynamical potential $\delta\hat{\epsilon}_i$ at its knots is slightly different at each site, since its periodicity with wave length λ mismatches the lattice constant $a = \lambda_0/2$ of the main lattice. This effect is visualized by the bold crosses at the knots of $\cos(kx)$ in Figure 7.5. As the ratio λ/λ_0 is not irrational for the chosen parameters, this pattern has a finite period. As long as the system size is below this period the system mimics a situation where the ratio of the wave lengths is irrational. Within the region of coherent scattering into the cavity ($\hat{\Phi} > 0$), inside the black line in the phase diagram, there exists a BG region. A typical situation of the BG phase is shown in Figure 7.6 d), where we find stripes of MI sites, which are populated by one particle. They are separated from each other by stripes which show a checker board pattern of empty sites and sites occupied by one particle and in between there are empty regions. All these sites are MI sites. At the border of these stripes there exist connected regions of SF sites with non-integer particle numbers, where particle fluctuations are possible. These SF islands grow with increasing tunneling rate JZ/U until they percolate in z -direction along the minima of $V_1 J_0^{(i)}$ at the BG-SS_Z transition. For even larger values of the tunneling rate JZ/U the percolation also occurs in x -direction, which we call the SS region, according to Table 7.2. A typical density distribution for the SS phase is shown in Figure 7.6 e). All sites, except of the checker board regions, show non-integer particle numbers and form a SF cluster, which connects all borders of the system. Above the upper rim of the black line in the phase diagram, for larger values of the tunneling

rate JZ/U , there exists also a SF region, where we find the percolation of SF sites in both dimensions, but since $\hat{\Phi} = 0$, there exists no checker board pattern.

For small chemical potentials μ/U there exists a pronounced SS_Z protrusion for small tunneling rates JZ/U . In order to understand the existence of this SS_Z region, we take a closer look at Equation (7.31) describing the knots of the dynamic potential $\delta\hat{\epsilon}_i$. At the fifth knot the index $i_{r=5} = 83$ is an integer value, which means that a minimum of $V_1 J_0^{(i)}$ and one knots of $\hat{\delta}(\hat{\mathbf{n}}) \hat{\Phi} Z_0^{(i)}$ coincide with the lattice site at $i_x = 83$.

An example for the situation inside this SS_Z protrusion is shown in Figure 7.6 f). There are empty regions alternating with checker board patterns. We see that the percolation of a SF cluster took place along the yellow line with the site index $i_x = 83$. A cut at $i_z = 20$ of both parts of the dynamic potential $\delta\hat{\epsilon}_i$ is shown in Figure 7.7 a). The static potential $V_1 J_0^{(i)}$ is shown in red and has regular minima at $z = i_r a$. The dynamic potential $\hat{\delta}(\hat{\mathbf{n}}) \hat{\Phi} Z_0^{(i)}$ is shown in blue. The values of the dynamic potential at the minima of the static potential are marked by the dark blue crosses. We see that here both, the minimum of the static potential as well as the knot of the dynamic potential appear at the site with the index $i_x = 83$. Along this specific lines the percolation of SF clusters is possible without any potential obstacles in between. At these small occupation numbers the minima of the dynamic potential $\delta\hat{\epsilon}_i$ are filled with particles first. Since the dynamic potential $\hat{\delta}(\hat{\mathbf{n}}) \hat{\Phi} Z_0^{(i)}$ changes sign at each site, a connected line of SF clusters can only occur along a knot, where the function is constant. The particle number of the percolating line $i_x = 83$ for increasing μ/U and fixed $JZ/U = 0.0081$ is shown in Figure 7.7 b). In the beginning for small chemical potential μ/U this line is empty, but since there are SF islands at the minima of the dynamic potential $\delta\hat{\epsilon}_i$ elsewhere in the lattice, the system is in the BG regime. With increasing chemical potential μ/U the particle number rises and this line is occupied by a non-integer particle number at all sites simultaneously. The particle number becomes non-integer, indicating particle fluctuations and the sites form a percolating SF cluster along this line. For even higher values of the chemical potential μ/U the particle number increases further until each site is filled up with one particle. Now particle fluctuations are suppressed and the sites behave like MI sites. It now forms a barrier for particle fluctuations and no longer a percolating SF cluster. Thus the system consists of a mixture of MI and SF sites, but does not contain a percolated SF cluster. Therefore, the system re-entered the BG region.

7.4.2 Phase diagram for $\lambda = \lambda_0/2 + \epsilon_\lambda$

In the second case the wave length of the cavity field is given by $\lambda = \lambda_0/2 + \epsilon_\lambda$. The corresponding phase diagram is shown in Figure 7.8 a). Analogously to the previous case there are parameter regions in which coherent scattering into the cavity is supported ($\hat{\Phi} > 0$) and others where it is suppressed ($\hat{\Phi} = 0$) as visible in Figure 7.8 e). Since l is even here, we do not expect the formation of a checker board pattern according to Equation (7.29). For $l = 2$ the period of the dynamic potential $\delta\hat{\epsilon}_i$ is rather small; the stripes of the static potential are separated by only $i_p/2 \approx 2.43$ lattice sites. A density distribution according to this pattern is shown in Figure 7.8 c) for a BG phase shortly before the percolation of

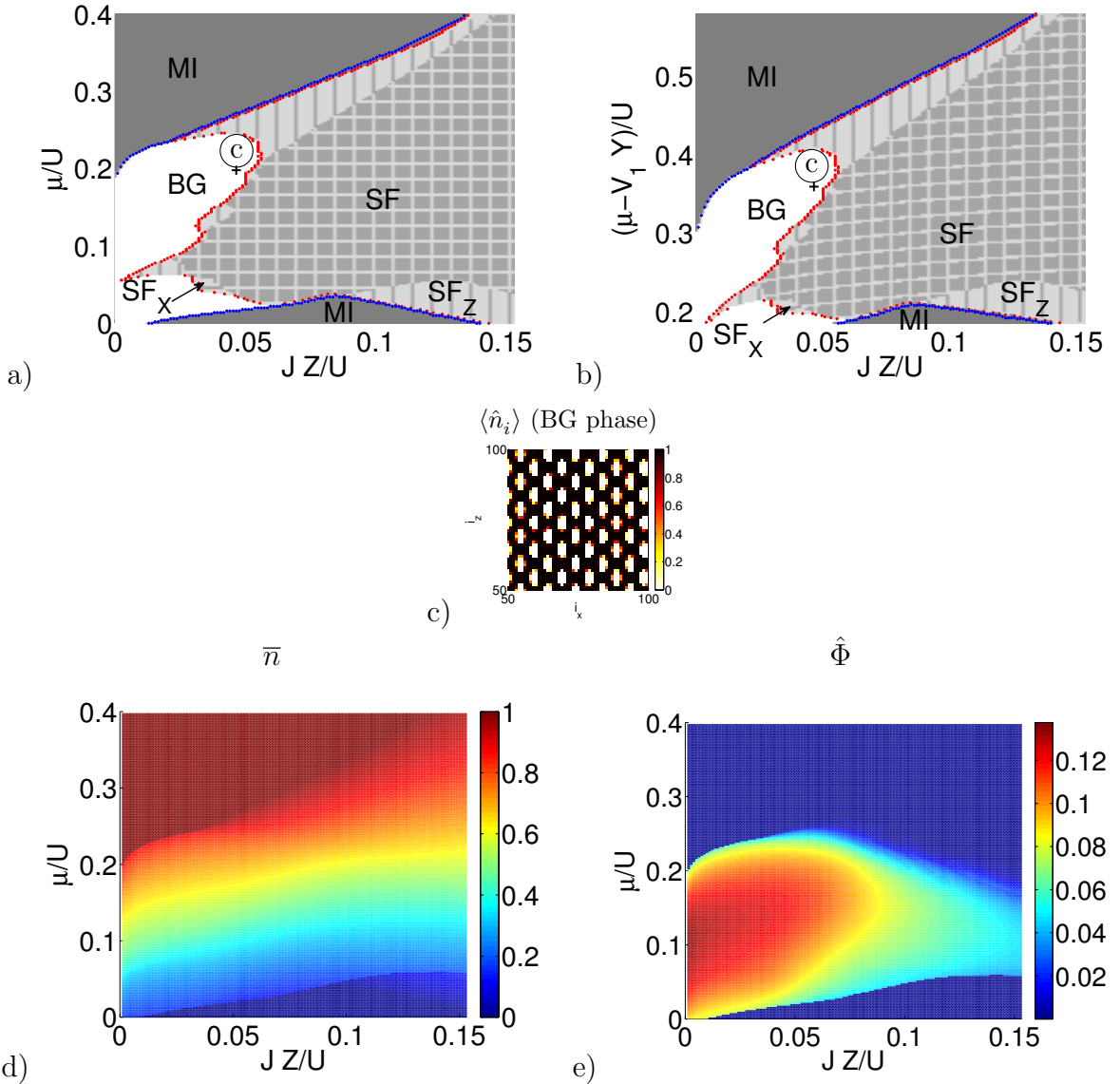


Figure 7.8: (a) and (b): The phase diagram for $\lambda = \lambda_0/2 + \epsilon_\lambda$ as a function of μ/U or rather $(\mu - V_1 Y)/U$ and JZ/U , where Y is the mean value of $J_0^{(i)}$. The border of the MI region is shown with blue dots and marks the appearance of SF sites. The border of the SF region, shown in red, marks the percolation of the SF cluster. The black cross, which is labeled with the circled letter, marks the parameters chosen in Figure c) showing the local boson occupation number $\langle \hat{n}_i \rangle$ for the parameters $JZ/U = 0.0465$, $\mu/U = 0.198$. (d) and (e): Mean particle number \bar{n} and occupation number of the cavity mode $\hat{\Phi}$.

the SF cluster. The system shows regions where the sites are occupied by one particle. In between there are empty islands according to the maxima of the dynamic potential $\delta\hat{\epsilon}_i$. At the borders of these MI regions SF regions with non-integer particle number occur, which are shown in yellow and red.

In the region of small chemical potentials μ/U we also find a pronounced SF protrusion.

In this region a minimum of the static potential $V_1 J_0^{(i)}$ and the knots of the dynamic potential $\hat{\delta}(\hat{\mathbf{n}}) \hat{\Phi} Z_0^{(i)}$ almost coincide with the lattice site at $i_x = 4, 10, 18$, which enables the system to populate these specific lines with an increasing number of particles as μ/U rises. While it is filled with a non-integer number of particles, particle fluctuations are possible and these lines form percolating SF clusters until they are filled up with one particle per site and the sites behave like MI sites again. This behavior is analogous to the situation discussed for $l = 1$ and shown in Figure 7.6 f).

In contrast to the previous case, where the percolation always takes place in z -direction, here we find all possible combinations. Along the percolation line, shown with red dots, the percolation occurs mostly in z -direction and we refer to this phase as the SF_Z phase according to Table 7.2. For intermediate chemical potentials μ/U the percolation occurs in both directions simultaneously. This SF phase exists in a wide parameter range of the phase diagram. There is also a small region, where the percolation occurs only along the x -direction leading to the SF_X phase, whose occurrence is a unique feature of the $l = 2$ case.

7.4.3 Phase diagram for $\lambda = \lambda_0/3 + \epsilon_\lambda$

The phase diagram of the third case, where the wave lengths of the cavity field is given by $\lambda = \lambda_0/3 + \epsilon_\lambda$ is shown in Figure 7.9 a). Since l is odd here, we expect the formation of a checker board pattern, according to Equation (7.29) in the regions where the occupation number of the cavity mode $\hat{\Phi}$ is positive. But as the frequency of the dynamic potential $\delta\hat{\epsilon}_i$ is also on the order of one lattice site, $i_p/2 \approx 0.76$, the checker board pattern is not visible in the particle densities.

Similarly to the previous cases there exists a MI region, where the lattice is empty and another one, where the lattice is occupied by one particle per site. In between the mean particle number \bar{n} , shown in Figure 7.9 d), increases smoothly. For small values of the chemical potential μ/U the pronounced SF_Z protrusion appears in the vicinity of the BG region. Within this region the percolation takes place at lattice sites, where the minima of the dynamic potential $\delta\hat{\epsilon}_i$ almost fit to the position of the lattice sites. An example of a BG is shown in Figure 7.9 c), where the sites are mainly occupied by one particle or are empty. At the borders of thesees MI regions non-integer particle numbers occur. Along the percolation line, shown with red dots in the phase diagram, the percolation mostly occurs in z -direction, but for intermediate chemical potentials μ/U , there exist also transitions to the SF phase, where the percolating SF cluster occurs simultaneously in both directions.

Conclusion

The interplay of a regular optical lattice of wave length λ_0 and an optical field produced by photons inside a cavity of wave length λ leads to different dynamical on-site potentials $\delta\hat{\epsilon}_i$, which depend on the local particle density of the system. In this chapter we have studied this situation for commensurate and incommensurate wave lengths. In all cases we have

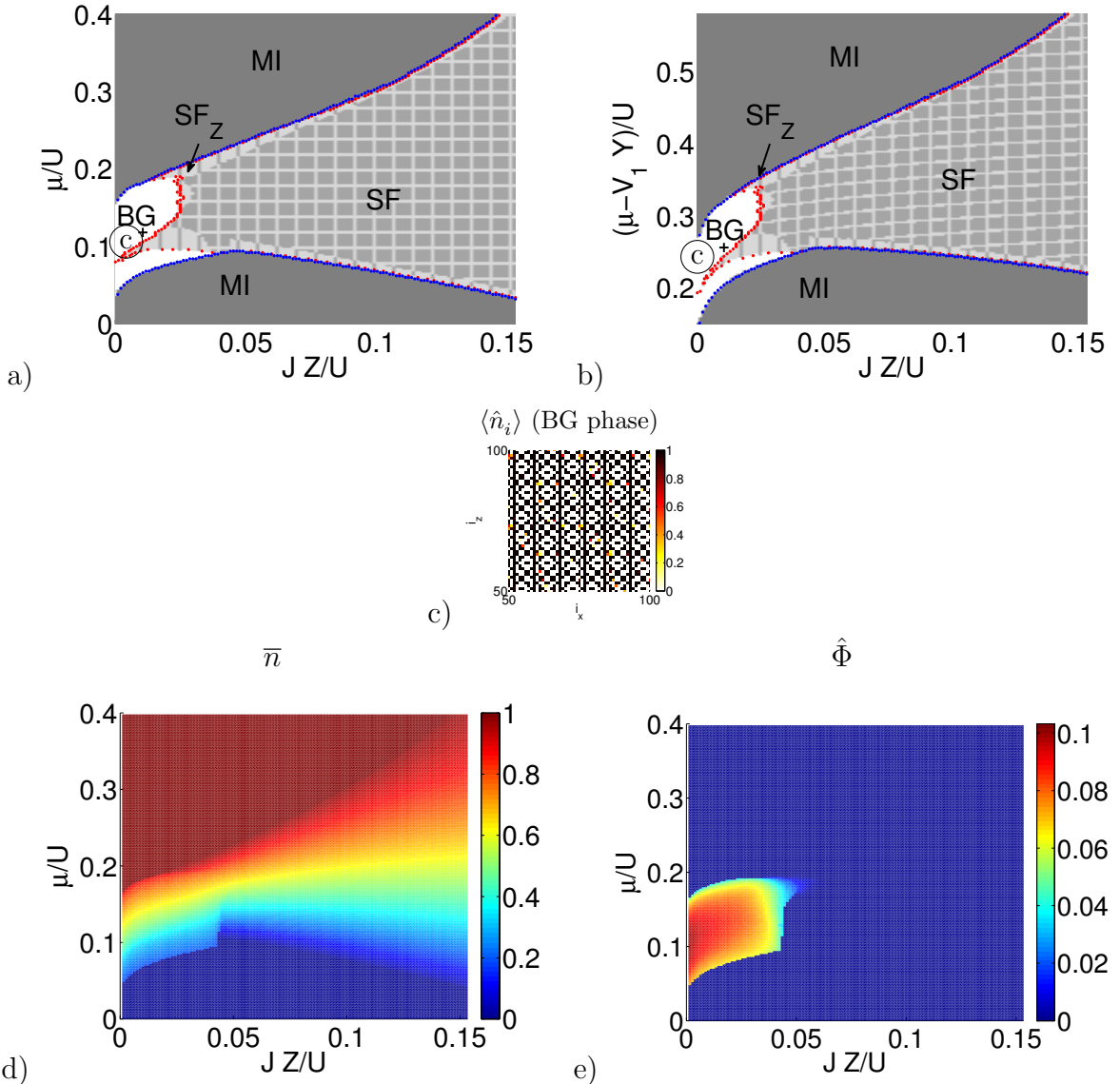


Figure 7.9: (a) and (b): The phase diagram for $\lambda = \lambda_0/3 + \epsilon_\lambda$ as a function of μ/U or rather $(\mu - V_1 Y)/U$ and JZ/U , where Y is the mean value of $J_0^{(i)}$. The border of the MI region is shown with blue dots and marks the appearance of SF sites. The border of the SF region, shown in red, marks the percolation of the SF cluster. The black cross, which is labeled with the circled letter, marks the parameters chosen in Figure c) showing the local boson occupation number $\langle \hat{n}_i \rangle$ for the parameters $JZ/U = 0.0105$, $\mu/U = 0.118$. (d) and (e): Mean particle number \bar{n} and occupation number of the cavity mode $\hat{\Phi}$.

found regions in parameter space, in which particle fluctuations are negligible and the scattering of photons into the cavity field is suppressed ($\hat{\Phi} = 0$). In these regions the particles only feel the regular optical lattice with wave length λ_0 and undergo a direct MI-SF transition. With the onset of particle fluctuations ($\hat{\Phi} \neq 0$) photons scatter into the cavity field and the atoms feel the overlap of the optical lattice with wave length λ_0

and the optical field of the photons in the cavity with wave length λ .

Depending on the relation of λ_0 and λ we have found different scenarios in the phase diagrams: For the case of commensurate wave lengths we find two classes of phase diagrams; one for odd and another for even values of l . For odd values of l , for example $\lambda_0 = \lambda$, there exists a row of MI region, where all lattice sites are occupied by an integer number of particles, alternating with MICB regions, where the particle density changes at each site according to a checker board pattern. At the tips of these MICB regions, there exists a SS phase, where the system is SF and still the particle density shows a checker board pattern. For even larger values of the tunneling rate JZ/U the SF phase is reached, where the particle number increases smoothly with the chemical potential μ/U . For odd values of l , the phase diagram consists of regular Mott-lobes, which are surrounded by the SF phase.

In the incommensurate case besides the MI, the SF and the SS phase a variety of additional phases occur. In contrast to the commensurate case, here the percolation of SF cluster does not occur in both directions simultaneously. That is why for intermediate tunneling rates J/U we find regions in the phase diagram, where the system is SF in one direction, while in the perpendicular direction it still behaves like a BG. For even larger tunneling rates JZ/U the percolation finally occurs in both directions. Moreover, for odd values of l the formation of a checker board pattern in the particle density is visible in parameter regions, where the cavity mode is occupied. In this phase the structure factor $S(\vec{k})$ shows a peak at (π, π) , and therefore this phase is referred to as the SS phase [111–113]. Within this phase the system is SF, which means that a percolating SF cluster exist, and the particle densities show a checker board pattern. In all incommensurate scenarios in the regime of small chemical potentials μ/U , a pronounced SF regions exists down to small tunneling rates JZ/U . This feature originates from the fact that a minimum of the static potential $V_1 J_0^{(i)}$ coincides with the saddle point line of the dynamic potential $\hat{\delta}(\hat{n}) \hat{\Phi} Z_0^{(i)}$. At these low densities this specific line can be filled up with particles, as the chemical potential μ/U , increases without any potential barrier in between. During this process these sites form a percolating SF cluster until they are filled up with one particle per site and become MI sites again. Then, the system re-enters the BG phase, since the percolating SF cluster has vanished.

8 Conclusion

In this thesis we have developed two innovative results: On the one hand an intuitive picture of the BG phase has been introduced, which enables us to determine the phase transitions of the disordered BH model in LMF approximation with high accuracy confirmed by quantum Monte-Carlo results. On the other hand we have shown that for the comparison of experimental setups, like the quasi-periodic bi-chromatic potential, with theoretical models, which are mostly restricted to disorder of the on-site energies, also disorder in the tunneling rates has to be taken into account. For a quasi-periodic bi-chromatic potential disorder in the tunneling rates is just as relevant as on-site disorder, even though the corresponding disorder strengths are separated by one order of magnitude.

In the ordered BH model local and global averaged parameters are identical. This, however, changes in the disordered case. Since in the ordered case all sites have the same BH parameters, local as well as global, averaged parameters behave simultaneously and both indicate the phase transitions at the same values of the BH parameters. In the MI phase each site is occupied by an integer number of particles and the mean particle number equals the local number of particles at each site. Since there exist no particle fluctuations all local SF parameters are zero as well as their mean, the SF order parameter. In the SF phase we find the same positive value of the local SF parameter at each site, agreeing with the global SF order parameter. In both cases the global parameters, which serve as identifiers of the phase transitions, coincide with the corresponding local quantities.

This situation changes if disorder is introduced to the BH model and all BH parameters vary locally resulting in a specific set of BH parameters for each site. The attempt of describing this system in LMF approximation with the help of global parameters fails, since they vary smoothly in the vicinity of the phase transition. The mean global parameters cannot reflect the processes occurring locally, especially at the phase transitions. Moreover, an intuitive local picture of the processes in the BG phase has thus been missing so far.

In some features the BG phase resembles the MI in others the SF phase. Its ground state is non-coherent, just as the MI phase, but yet the Bose cloud is compressible as in the SF phase. In agreement with this fact we have shown that in the BG phase the system consists of a mixture of so-called SF and MI sites. MI sites show an integer particle number and a zero local SF parameter, just like sites in the MI phase of the ordered system. SF sites are characterized by a non-integer fluctuating particle number and a non-zero local SF parameter corresponding to the sites in the SF phase of the ordered BH model. Connected SF sites form SF clusters, which are locally compressible, making the whole atomic cloud compressible. These SF islands show a fixed phase relation, but since the whole system only consists of small coherent SF islands, there exists no global phase co-

herence. Global coherence sets in with the appearance of a percolated SF cluster, which dominates the system behavior and establishes long range order. The percolation of one of the SF clusters, therefore, marks the BG-SF phase transition in parameter space.

The MI-BG transition in turn is given by the appearance of the first SF site in the system. This criterion for the phase transitions, to which we refer to as the LMF cluster analysis, leads to a phase diagram, which is in excellent agreement with quantum Monte-Carlo results, but which deviates gravely from other LMF phase diagrams determined on the basis of global parameters. Moreover, it yields an intuitive picture of the local processes going on in the BG phase. The phase transition can then be interpreted as the point, at which local properties of the system become globally relevant.

To introduce disorder in an experimental setup there exist two common possibilities. A diffuser modifies the intensity of the laser locally, leading to inhomogeneities in the resulting optical lattice [26, 27]. Another realization is to use a bi-chromatic potential, which is formed by a main optical lattice with high intensity and a second weaker one with slightly different wave length [3]. This forms a quasi-periodic potential, which serves as a quasi-random potential for a sufficiently small detuning of the wave lengths. As a clear advantage of this setup the system parameters can be varied freely, whereas for a diffuser the parameters are fixed by the optical device.

As the second main result, we have shown that for a quasi-periodic bi-chromatic potential the influences of disorder in the tunneling rates is just as important as in the on-site energies. With the help of the LMF cluster analysis we have studied the specific influences of disorder in each BH parameter separately and found characteristic features in the phase diagram for each case. Only in the case of on-site disorder there exists an infinite number of Mott-lobes. For tunneling disorder the SF phase reaches down to vanishing tunneling rates and separates individual BG regions from each other. A tricritical point, where all three phases approach tightly, occurs in the case of disorder in the inter-particle interaction. Moreover, the relevant disorder strengths, for which all three phases occur in the phase diagram, is one order of magnitude smaller for disorder in the tunneling rates than the one for disorder in the on-site energies or inter-particle interaction. This is an important fact, since in various works on the quasi-periodic bi-chromatic potential [37, 38, 55–57] it has been argued that disorder in the tunneling rate can be neglected, even though it would have been necessary to analyze this carefully.

The influence of disorder in the tunneling rates is also visible directly in the phase diagrams of a quasi-periodic bi-chromatic potential. To show this, we have generalized the Wannier functions by allowing them to be asymmetric, reflecting the inhomogeneities of the optical potential. Thereby, we were able to introduce disorder already in the usual derivation of the BH model. This treatment influences all three BH parameters locally, resulting in statistical distributions for each BH parameter. By comparing the variance of these distributions with the disorder strength in the case of isolated disorder in one single parameter, we have shown that besides of disorder in the on-site energies also disorder in the tunneling rates reaches the critical regime, where all three phases occur in the phase diagram. The influence of disorder in the inter-particle interaction can actually be neglected, since the variance of its distribution is found to be two orders of magnitude smaller than the critical disorder strength.

This is also reflected by the fact that the influence of tunneling disorder is clearly visible in the phase diagram for the quasi-periodic bi-chromatic potential. Even though its structure resembles the one for isolated on-site disorder, deviations of the transition lines are obvious. In the vicinity of integer values of $(\mu - \epsilon)/U$ the SF phase separates individual BG regions from each other, which is a unique characteristic feature of disorder in the tunneling rates. This finding once more promotes the statement, that disorder in the tunneling rates indeed influences the phase diagram for quasi-periodic bi-chromatic potentials, which is important in particular for the comparison of experimental and theoretical data.

Moreover, isolated disorder, as mostly studied in theory, cannot be realized with a quasi-periodic bi-chromatic potential, since in the whole parameter regime the disorder strength of both parameters is non-zero. We expect to find the same situation for the second experimental possibility, where disorder is introduced via a diffuser. Since a diffuser locally modulates the intensity, also in this case all BH parameters, especially the tunneling rates, will be affected. Experimentally real isolated disorder can only be realized for the inter-particle interaction. Since this parameter is adjusted by an external magnetic field, independently of the optical lattice, disorder can be realized in the vicinity of a Feshbach resonance without any interference with the other parameters [52, 54].

For future work it is important to notice, that the cluster analysis is not restricted to data determined within the LMF approximation. The cluster analysis depends only on the discrete map G_i representing the MI and SF sites of the system [2]. The mapping from numerical data on G_i can be adjusted to the method used for solving the ground state problem. In this work we distinguished between MI and SF sites on the basis of the particle number [2], but equivalently it is also possible to use, for example, the local SF parameter or the local compressibility. Therefore, the underlying LMF algorithm can be replaced by some other numerical method with a corresponding map G_i separating MI from SF sites.

Moreover, in modern experiments single site detection of ultra cold bosons in optical lattices is possible [95, 96], which yields the opportunity to observe the particle numbers at each site individually. Particle fluctuations can than be directly observed through in-situ imaging, allowing for a direct distinction between MI and SF sites using time averaged occupation numbers. Therefore, this experimental technique might allow access to the observation of SF islands and their percolation and thereby improve our understanding of the BG phase.

The last part of this thesis deals with the application of the LMF cluster analysis, developed in the previous parts, to current experimental research, which allows for a direct comparison [8]. This system consists of a regular optical lattice at some wavelength λ_0 and an additional cavity collecting photons producing an optical field at a different wavelength λ . The photon occupation number of the cavity mode depends on the local particle density of the whole system and thus introduces long-range interaction. This system can be described by a BH model, whose on-site energies are given by correlated disorder [5, 6]. Our theoretical studies on the basis of LMF cluster analysis for the first time yield the phase diagrams for this kind of systems covering both, commensurate and incommensurate ratios of the wave lengths. These systems in fact turn out to reveal a much richer

variety of occurring phases. Besides the MI, BG and SF phase, for certain ratios of the wave lengths also the so-called MICB and SS phase appear. In the MICB phase there exists an energy gap in the particle excitation spectrum preventing particles from tunneling, similar to a MI, but here additionally the density profile shows a checker board pattern, where the sites are occupied by an alternating number of particles. In the SS phase the system is SF but also here the particle densities show a checker board pattern. Even though tunneling of particles is favorable as they can move without energy cost, like in the SF phase, in the SS phase we, nevertheless, find a checker board density profile produced by superlattices with double period. At the moment it is possible to distinguish between the MI, SF, MICB and SS in experiments with a combination of time-of-flight imaging and measurement of the light output of the cavity. For the detection of the BG phase the measurement of an additional feature is necessary which is still a challenging project in experimental groups [114].

A Mean-field description

The mean-field description of BECs is governed by the widely used Gross-Pitaevskii equation. In this framework a wide range of features of BECs have successfully been captured. One of the possible derivations of the Gross-Pitaevskii equation is to compute the expectation value of the Hamiltonian in coherent states. By using the properties of Lie algebras, the coherent states of the harmonic oscillator can be generalized to various systems in second quantization. The expectation value $\langle \psi | \hat{a}_i | \psi \rangle$ of the annihilation operator and its complex conjugate are important quantities in the mean-field description, as all desired correlation functions factorize. In a coherent state these values are non-zero, whereas in a Fock state they vanish exactly. Therefore, the mean value $\langle \psi | \hat{a}_i | \psi \rangle$, which is the SF order parameter, can be interpreted as a number, showing whether local parts of the wave function have significant overlap with coherent states.

A.1 Glauber coherent states

Schrödinger already mentioned the coherent states in context of the quantum harmonic oscillator in 1926 for the first time as a possible connection between the quantum and classical mechanical description [115]. In their studies of the correlation functions of electromagnetic fields, Glauber and Sudarshan coined the term coherent states in 1963, as the correlation function of n th order factorizes in these states [116–119]. The fundamental introduction of coherent states in the context of Lie algebras was finally achieved by Perelomov and Gilmore in 1972 by extending the definition of the coherent states of the harmonic oscillator to general systems in second quantization [120–123].

The coherent states $|\alpha\rangle$ of the harmonic oscillator at frequency ω can be defined in three different, but equivalent ways [117, 123]:

1. The coherent state $|\alpha\rangle$ is an eigenstate of the annihilation operator \hat{a} with some complex eigenvalue α :

$$\hat{a}|\alpha\rangle = \alpha|\alpha\rangle. \quad (\text{A.1})$$

2. The coherent state $|\alpha\rangle$ shows minimal uncertainty relationship

$$(\Delta\hat{p})^2 (\Delta\hat{q})^2 = \left(\frac{\hbar}{2}\right)^2, \quad (\text{A.2})$$

where the coordinate and momentum operators are given by

$$\hat{q} = \sqrt{\frac{\hbar}{2m\omega}} (\hat{a}^\dagger + \hat{a}), \quad \hat{p} = \frac{1}{i} \sqrt{\frac{\hbar m\omega}{2}} (\hat{a}^\dagger - \hat{a}) \quad (\text{A.3})$$

and $(\Delta \hat{f})^2 = \langle \alpha | (\hat{f} - \langle \hat{f} \rangle)^2 | \alpha \rangle$ with $\langle \hat{f} \rangle = \langle \alpha | \hat{f} | \alpha \rangle$.

3. The coherent state $|\alpha\rangle$ can be represented as the displacement of the vacuum state $|0\rangle$ according to

$$|\alpha\rangle = D(\alpha)|0\rangle, \quad (\text{A.4})$$

while the displacement operator is given by

$$D(\alpha) = \exp(\alpha \hat{a}^\dagger - \alpha^* \hat{a}). \quad (\text{A.5})$$

In agreement with these definition the coherent state of the harmonic oscillator the particle number basis is given by

$$\begin{aligned} |\alpha\rangle &= \exp(\alpha \hat{a}^\dagger - \alpha^* \hat{a})|0\rangle \\ &= \exp\left(-\frac{\alpha^* \alpha}{2}\right) \sum_{n=0}^{\infty} \frac{\alpha^n}{\sqrt{n!}} |n\rangle. \end{aligned} \quad (\text{A.6})$$

As the operators $\{\hat{a}^\dagger, \hat{a}, \hat{1}\}$ obey the familiar commutation relations

$$[\hat{a}^\dagger, \hat{1}] = 0, \quad [\hat{a}, \hat{1}] = 0, \quad [\hat{a}, \hat{a}^\dagger] = \hat{1}, \quad (\text{A.7})$$

they span a closed algebra, called Lie algebra. All expectation values of elements of the Lie algebra in the corresponding coherent states can be computed analytically. Moreover, if the dynamics of a system is governed by a Hamiltonian, which is a linear superposition of operators of the Lie algebra, a coherent state remains coherent throughout the evolution in time. Coherent states are also denoted as classical states as the expectation values of coordinate and momentum operators in the coherent states $\langle \alpha | \hat{q} | \alpha \rangle$ and $\langle \alpha | \hat{p} | \alpha \rangle$ follow the trajectories of the classical harmonic oscillator. In this way, they can connect quantum to classical dynamics.

The concept of Lie algebras and the representation of coherent states by displacement of the vacuum state, as given in the third definition, can be extended to various systems in second quantization and has found its application in the description of bosonic as well as fermionic lattice systems as studied in quantum optics [117, 124]. Especially interesting in the context of the BH model is the bosonic multimode Lie algebra $u(M)$, given by $2M + 1$ operators $\{\hat{a}_i^\dagger, \hat{a}_i, \hat{1}\}$ for $i = 1, \dots, M$, where M is the number of sites in an optical lattice. The involved operators obey the commutation relations

$$[\hat{a}_i, \hat{a}_j^\dagger] = \hat{1} \delta_{ij}, \quad [\hat{a}_i^\dagger, \hat{a}_j^\dagger] = [\hat{a}_i, \hat{a}_j] = [\hat{a}_i^\dagger, \hat{1}] = [\hat{a}_i, \hat{1}] = 0. \quad (\text{A.8})$$

The corresponding coherent states, also called Glauber coherent state, can be constructed with the help of the generalized displacement operator according to

$$\begin{aligned}
|\vec{\alpha}\rangle &= D(\alpha_1, \dots, \alpha_M) |\vec{0}\rangle \\
&= \exp \left(\sum_{i=1}^M (\alpha_i \hat{a}_i^\dagger - \alpha_i^* \hat{a}_i) \right) |\vec{0}\rangle \\
&= \prod_{i=1}^M \exp \left(\alpha_i \hat{a}_i^\dagger - \alpha_i^* \hat{a}_i \right) |\vec{0}\rangle = \prod_{i=1}^M |\alpha_i\rangle \\
&= \prod_{i=1}^M \exp \left(-\frac{\alpha_i^* \alpha_i}{2} \right) \exp \left(\alpha_i \hat{a}_i^\dagger \right) |\vec{0}\rangle \\
&= \exp \left(-\frac{\vec{\alpha}^\dagger \vec{\alpha}}{2} \right) \prod_{i=1}^M \exp \left(\alpha_i \hat{a}_i^\dagger \right) |\vec{0}\rangle \\
&= \exp \left(-\frac{\vec{\alpha}^\dagger \vec{\alpha}}{2} \right) \sum_{n_1=0}^{\infty} \dots \sum_{n_M=0}^{\infty} \frac{\alpha_1^{n_1} \dots \alpha_M^{n_M}}{\sqrt{n_1! \dots n_M!}} |n_1, \dots, n_M\rangle. \tag{A.9}
\end{aligned}$$

For vanishing inter-particle interaction U the BH Hamiltonian (2.43) is a linear combination of operators of the $u(M)$ algebra and a coherent state remains coherent under this time evolution. The expectation values of any product of elements of the Lie algebra can be computed analytically. This is of main interest as any coherence respectively correlation function, for example of the form $C_r = \langle \vec{\alpha} | \hat{a}_i \hat{a}_{i+r}^\dagger | \vec{\alpha} \rangle$, can be calculated easily, as this function factorizes. That is why Glauber called these states coherent states [116].

Within the $su(M)$ algebra the total particle number $N = \sum_{i=1}^M n_i$ is a given parameter and the corresponding coherent state is given by [124]

$$|\vec{\alpha}\rangle = \sum_{n_1+\dots+n_M=N} \sqrt{\frac{N!}{n_1! \dots n_M!}} \alpha_1^{n_1} \dots \alpha_M^{n_M} |n_1, \dots, n_M\rangle, \tag{A.10}$$

where the sum runs over all combination of n_1, \dots, n_M satisfying $n_1 + \dots + n_M = N$.

A.2 Gross-Pitaevskii equation

Taking expectation values in the $u(M)$ coherent states is one possibility to introduce a mean-field description of the BH model. This ansatz leads to a hamiltonian function

$$\mathcal{H}(\alpha_i^*, \alpha_i) = \sum_i (\epsilon_i - \mu) |\alpha_i|^2 + \sum_i \frac{U_i}{2} |\alpha_i|^2 (|\alpha_i|^2 - 1) - \sum_{\langle i,j \rangle} J_{ij} \alpha_i^* \alpha_j, \tag{A.11}$$

describing the corresponding classical energy. The dynamics of this systems is then given by the equations

$$i\dot{\alpha}_i = \frac{\partial \mathcal{H}}{\partial \alpha_i^*} \quad \text{and} \quad i\dot{\alpha}_i^* = -\frac{\partial \mathcal{H}}{\partial \alpha_i}, \tag{A.12}$$

where α_i and α_i^* are conjugate variables. With the canonical transformation

$$q_i = \sqrt{\frac{\hbar}{2m\omega}} (\alpha_i^* + \alpha_i) , \quad p_i = \frac{1}{i} \sqrt{\frac{\hbar m\omega}{2}} (\alpha_i^* - \alpha_i) \quad (\text{A.13})$$

these equations resemble the canonical classical equations

$$\dot{q}_i = \frac{\partial \mathcal{H}}{\partial p_i} \quad \text{and} \quad \dot{p}_i = -\frac{\partial \mathcal{H}}{\partial q_i} \quad (\text{A.14})$$

with $\mathcal{H}(q_i, p_i)$ being the hamiltonian function. Plugging the hamiltonian function (A.11) into the Equations (A.12), this immediately yields the discrete Gross-Pitaevskii equation

$$i \dot{\alpha}_i = \sum_i (\epsilon_i - \mu) \alpha_i + \sum_i \frac{U_i}{2} (2|\alpha_i|^2 - 1) \alpha_i - \sum_{\langle i,j \rangle} J_{ij} \alpha_j , \quad (\text{A.15})$$

which also exists in the continuous limit and as a stationary version. This equation is the heart of the mean-field description of BECs [22, 64, 65].

There are also other possibilities to derive this equation, two of which will be shortly discussed here. The starting point for a second possible derivation of the Gross-Pitaevskii equation is the quantum Heisenberg equation, where according to the Bogoliubov prescription, all operators are replaced by complex numbers [125]. Specifically this means that, the operators \hat{a}_i and \hat{a}_i^\dagger are replaced by the so-called wave functions of the condensate Ψ and Ψ^* . This step is justified by the fact that in a BEC a large number of atoms occupy the ground state and can be described by a single wave function $|\Psi\rangle$ [22]. This widely used description covers the collective motion of the atoms condensed in a BEC. To include other effects like the depletion of the BEC, higher order approximations, like for example Bogoliubov theory, are necessary.

For a third approach the many body wave function of N condensed particles can be written as a product of identical single particle wave functions $\chi_0(\vec{x}_i)$ according to

$$\Psi(\vec{x}_1, \dots, \vec{x}_N) = \prod_{i=1}^N \chi_0(\vec{x}_i) . \quad (\text{A.16})$$

The expectation value of the BH Hamiltonian in this wave function leads to the so-called Gross-Pitaevskii energy functional, which with the help of a variational ansatz also leads to the Gross-Pitaevskii equation [65].

To conclude, there are three different mean-field approaches, namely the approximation of the full many body wave function by a product of single particle wave functions, the replacement of operators by complex numbers as well as taking the expectation values in a coherent state, which all lead to the Gross-Pitaevskii equation. As they all result in the same mean-field equation, they are therefore equivalent approximations, where the BEC can be described by one single wave function obeying non-linear dynamics according to the Gross-Pitaevskii equation. Mean-field theory has turned out to be a very powerful framework to describe collective features of the BEC, like for example solitons or vortices [64]. Quantum effects, as for instance entanglement, break-down and revival or the

quantum phase transitions, however, are not covered by this theory. One possibility to go beyond, is the introduction of the LMF theory, which is able to capture more of the quantum nature of the system and shows break-down and revival as well as the quantum phase transitions.

A.3 Superfluid order parameter

The expectation value of the annihilation operator $\langle \psi | \hat{a}_i | \psi \rangle$ in some system state $|\psi\rangle$ is an important quantity in any mean-field description. In the first derivation of the Gross-Pitaevskii equation, presented in the last section, the system state is approximated by a coherent state and the expectation value is given by $\langle \vec{\alpha} | \hat{a}_i | \vec{\alpha} \rangle = \alpha_i$ and is non-zero. However, in the second derivation it is assumed that the expectation value $\langle \psi | \hat{a}_i | \psi \rangle$ exists without specifying the system state $|\psi\rangle$. This method is analogous to the introduction of the local SF parameter $\psi_i = \langle \psi | \hat{a}_i | \psi \rangle$ in Section (3.1), where the expectation value is taken in the ground state of the $|\psi\rangle$ without assuming a special shape. The actual ground state is then determined by solving the LMF problem recursively.

The expectation value of the particle number of the ground state $|\psi\rangle$ is given by

$$\langle \psi | \hat{n}_i | \psi \rangle = \langle \psi | \hat{a}_i^\dagger \hat{a}_i | \psi \rangle \approx \langle \psi | \hat{a}_i^\dagger | \psi \rangle \langle \psi | \hat{a}_i | \psi \rangle = |\psi_i|^2 \quad (\text{A.17})$$

and the total number of particles in the macroscopically occupied ground state is given by $\sum_{i=1}^M |\psi_i|^2$.

Suppose the system state is given by a Fock state $|\psi\rangle = |n_1, \dots, n_M\rangle$, then the expectation is zero as the Fock states are orthogonal

$$\langle m_1, \dots, m_M | n_1, \dots, n_M \rangle = \delta_{m_1 n_1}, \dots, \delta_{m_M n_M}. \quad (\text{A.18})$$

However, if the system state $|\psi\rangle$ is a coherent state, this expectation value is simply given by $\langle \vec{\alpha} | \hat{a}_i | \vec{\alpha} \rangle = \alpha_i$ and in general non-zero as $|\vec{\alpha}\rangle$ is an eigenstate of \hat{a}_i . In LMF description the system state is approximated by a product of single site wave functions, according to Equation (3.5). This approximation enables us to introduce the picture of SF and MI sites in Chapter 4. While single sites can be described by a coherent state, leading to a positive local SF parameter ψ_i , others are in some other state showing zero values. Therefore, the SF order parameter $\psi = \overline{\psi_i}$, which according to Equation (3.7) is the mean value of all local SF parameters ψ_i , is a measure of the fraction of sites, which can be described by a coherent state.

In general states of the quantum system are some high dimensional possibly entangled many body states, which makes the situation more difficult. But from its shape it is not obvious if some degrees of freedom form something like a coherent state. With the help of the local SF parameter $\psi_i = \langle \psi | \hat{a}_i | \psi \rangle$ one can probe if the wave function locally leads to a positive value of the local SF order parameter ψ_i . If the wave function in this subspace of site i shows a significant overlap with exact eigenstates of the annihilation operator \hat{a}_i , namely the coherent states, the complete wave function may approximately be decomposed into a direct product of local coherent states and entangled many body

states for the rest of the system.

In the ordered BH system all sites are identical copies of each other with the same BH parameters. Thus, the local SF parameters ψ_i of each site are identical and equal to the SF order parameter $\psi = \bar{\psi}_i = \psi_i$. In this case the local quantity ψ_i reflects the behavior of the whole system. The particle number of the ground state is given by $\sum_{i=1}^M \langle \psi | \hat{n}_i | \psi \rangle = \sum_{i=1}^M |\psi_i|^2$. This situation changes in the disordered case, where at least one BH parameter randomly changes from site to site. This leads to varying local SF parameters ψ_i , which can be described by the PD $P(\psi)$ as discussed in Section 3.3.3. In the BG phase at some sites there exists a significant overlap with coherent states leading to positive values of the local SF parameter ψ_i , namely the SF sites. In this situation the SF order parameter $\psi = \bar{\psi}_i$ is small but non-zero. This effect has already been discussed in Section 3.3.1. According to LMF theory the SF order parameter ψ is supposed to indicate the BG-SF transition [44, 45], at which long range coherence occurs. This would imply that the SF order parameter ψ is zero in the BG phase and positive in the SF phase showing a precise kink at the phase transition. As discussed in Section 3.3.1, the SF order parameter ψ is small but positive in the BG phase and does not show a kink. As in the BG phase there always exist regions with positive local SF parameter ψ_i , its mean value, the SF order parameter ψ , may in fact be small, but positive. As shown in Section 3.3.1 in LMF description this is not due to finite size effects. However, since the local SF parameter ψ_i indicates an overlap with a coherent state locally, its mean value cannot serve as a measure for long range coherence. Thus, in contrast to the ordered case, in the disordered case the SF order parameter ψ , obtained in LMF approximation, does not yield the desired properties of an order parameter.

Conclusion

The concept of coherent states, as it was first introduced in the context of the quantum harmonic oscillator, can be extended for various systems in second quantization. The introduction of Lie algebras allows for a generalization of the displacement operator and a universal definition of coherent states. By the usage of these states, also called classical states, the well-known Gross-Pitaevskii equation can be derived, which is the basis of the widely used mean-field theory for the description of the collective features of a BEC. In this context the expectation value $\langle \psi | \hat{a}_i | \psi \rangle$ of the annihilation operator is an important quantity. In a coherent state this value is non-zero, while for example in a Fock state it is always exactly zero. This expectation value can be used in order to decide if local parts of the wave function show a significant overlap with coherent states.

B Two site Bose-Hubbard system

In LMF approximation there exist sites, which show integer particle numbers $\langle \hat{n}_i \rangle$, while the corresponding value of the full quantum ground state is non-integer. In order to stress this fact, we will compare the ground state of the two site problem with only two particles, for which the exact quantum result is available.

For the two site problem the quantum BH Hamiltonian (2.43) reduces to

$$\hat{H} = -\mu \hat{N} + \epsilon_1 \hat{n}_1 + \epsilon_2 \hat{n}_2 + \frac{U}{2} (\hat{n}_1 (\hat{n}_1 - 1) + \hat{n}_2 (\hat{n}_2 - 1)) - J (\hat{a}_1^\dagger \hat{a}_2 + \hat{a}_1 \hat{a}_2^\dagger) \quad (\text{B.1})$$

with the total particle number $\hat{N} = \hat{n}_1 + \hat{n}_2$. In the symmetric case ($\epsilon_1 = \epsilon_2 = 0$) the local particle number at each site is identical and integer ($\langle \hat{n}_1 \rangle = \langle \hat{n}_2 \rangle = 1$) independent of the other BH parameters J and U . The situation changes for the asymmetric case ($\epsilon_1 = -0.3$, $\epsilon_2 = 0.3$), for which the local particle numbers $\langle \hat{n}_1 \rangle$ and $\langle \hat{n}_2 \rangle$ as well as the mean particle number per site $\langle \hat{N} \rangle / 2$ are shown in Figure B.1 a). In the ground state the site with the lower on-site potential ϵ_1 shows a higher local particle number $\langle \hat{n}_1 \rangle$. Moreover, the local particle numbers $\langle \hat{n}_1 \rangle$ and $\langle \hat{n}_2 \rangle$ show non-integer particle numbers in the whole parameter range of the tunneling rate $J/U > 0$, while the total particle number $\langle \hat{N} \rangle$ is conserved, as the BH Hamiltonian in general commutes with the particle number operator \hat{N} .

Within the LMF approximation the two site Hamiltonian (B.1) is given by

$$\begin{aligned} \hat{H} &= \hat{H}_1 + \hat{H}_2, \\ \hat{H}_1 &= (\epsilon_1 - \mu) \hat{n}_1 + \frac{U}{2} \hat{n}_1 (\hat{n}_1 - 1) - J \psi_2 (\hat{a}_1^\dagger + \hat{a}_1 - \psi_1), \\ \hat{H}_2 &= (\epsilon_2 - \mu) \hat{n}_2 + \frac{U}{2} \hat{n}_2 (\hat{n}_2 - 1) - J \psi_1 (\hat{a}_2^\dagger + \hat{a}_2 - \psi_2). \end{aligned} \quad (\text{B.2})$$

The ground state of this system is computed self-consistently, as described in Section 3.1, for a given density of one particle per site, which fixes the chemical potential μ . In the symmetric case ($\epsilon_1 = \epsilon_2 = 0$) also here we find an equally distributed particle density, where the local particle numbers are integer values ($\langle \hat{n}_1 \rangle = \langle \hat{n}_2 \rangle = 1$), which is in full agreement with the exact quantum result. For the asymmetric case ($\epsilon_1 = -0.3$, $\epsilon_2 = 0.3$) the expectation values of the local particle number operators $\langle \hat{n}_1 \rangle$ and $\langle \hat{n}_2 \rangle$ are shown in Figure B.1 b). The local particle numbers $\langle \hat{n}_1 \rangle$ and $\langle \hat{n}_2 \rangle$ show non-integer values for large, but also integer values for small tunneling rates J/U . This is in contradiction to the exact quantum result shown in Figure B.1 a), where the local particle numbers are non-integer in the whole parameter regime of tunneling rate $J/U > 0$.

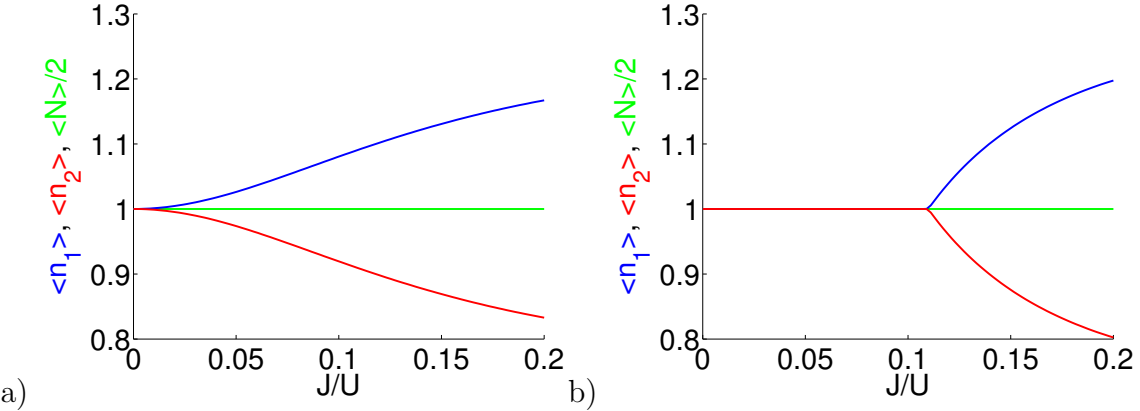


Figure B.1: The local particle numbers $\langle \hat{n}_1 \rangle$ (blue) and $\langle \hat{n}_2 \rangle$ (red) as well as the particle number $\langle \hat{N} \rangle / 2 = (\langle \hat{n}_1 \rangle + \langle \hat{n}_2 \rangle) / 2$ (green) resulting from exact diagonalization of the full quantum Hamiltonian (a) and from LMF theory (b).

Conclusion

From these results we can learn that for certain values of the tunneling rate J/U the LMF approximation predicts integer local particle numbers, while the quantum system shows non-integer values for all positive tunneling rates $J/U > 0$. This is due to the fact, that in LMF approximation the whole quantum wave function is approximated by a product of local wave functions, neglecting spatial correlations between the sites as well as quantum fluctuations.

C Monte-Carlo algorithm

In this appendix we will recall the fundamental principles of Monte-Carlo techniques, which are used in various fields of physics [126–129]. This method poses no restrictions on the system parameters, which means that it can be used in the whole parameter regime of the considered model. Finite size effects, which occur in all numerical simulations, can be treated with systematic descriptions. An example for such a treatment is described in Section (4.1). Advanced quantum Monte Carlo algorithms can improve the accuracy of QMC results up to a very high level. Therefore, the excellent agreement of the phase transition of the disordered BH model on basis of the LMF cluster analysis with QMC results presented in Section 4.3.1, is a strong evidence for the reliability of our method.

C.1 Classical Monte-Carlo algorithm

To understand the classical Monte-Carlo algorithm [130], let us consider the partition function

$$Z = \text{Tr } e^{-\beta H}, \quad (\text{C.1})$$

of the system, which is given by the trace over the exponential of the product of the inverse temperature $\beta = 1/(k_B T)$ and the Hamiltonian function H . The average value of a physical quantity A is then given by

$$\langle A \rangle = \frac{1}{Z} \text{Tr } A e^{-\beta H}. \quad (\text{C.2})$$

This equation states that the average of a quantity A is given by the average over all possible configurations ν with energy E_ν weighted by their probability

$$P_\nu = \frac{1}{Z} e^{-\beta E_\nu}, \quad (\text{C.3})$$

which is given by the Boltzmann weight $e^{-\beta E_\nu}$ [131]. There are configurations with a high Boltzmann weight, which provide a large contribution to the average of the quantity A and others with a small Boltzmann weight, which contribute less. In order to implement an effective algorithm, the challenge is to effectively generate configurations with high Boltzmann weights and only occasionally configurations with small Boltzmann weights. For this purpose let us assume we have some dynamical process producing the desired probability (C.3) in the long time limit

$$P_\nu(t \rightarrow \infty) = P_\nu. \quad (\text{C.4})$$

In order to investigate this process we introduce the master equation

$$\frac{dP_\nu(t)}{dt} = \sum_{\sigma} [P_{\sigma}(t) W(\sigma \rightarrow \nu) - P_{\nu}(t) W(\nu \rightarrow \sigma)] \quad (\text{C.5})$$

for the probability $P_{\nu}(t)$ of finding the system in a certain configuration ν at time t [131]. The probability per unit time for the system to undergo a transition from configuration σ to ν is given by the rate $W(\sigma \rightarrow \nu)$. The first term on the right hand side is the rate at which the configuration ν is populated, while the second term is the rate of its depopulation. If the system is in configuration ν it must undergo a transition to some other configuration σ or stay in configuration ν , which leads to the condition

$$\sum_{\sigma} W(\nu \rightarrow \sigma) = 1, \quad (\text{C.6})$$

where σ runs over all configurations including ν . The probability P_{ν} fulfills the condition

$$\sum_{\nu} P_{\nu}(t) = 1, \quad (\text{C.7})$$

since the system must be in one of the configurations ν .

So far the rates $W(\nu \rightarrow \sigma)$, bearing the information of the chosen dynamical process, are undefined. In general, every process fulfilling condition (C.4) is allowed. It is convenient to use the Markov process [131, 132], which satisfies two important properties: Firstly, the transition rates $W(\nu \rightarrow \sigma)$ are time independent. Secondly, the transition rate $W(\nu \rightarrow \sigma)$ depends only on the configurations ν and σ and is independent of the history, what had happened before the system reached configuration ν . Moreover, the Markov process is ergodic, which means that from all starting configurations ν every other configuration σ can be reached.

In the stationary limit $t \rightarrow \infty$ the master Equation (C.5) becomes

$$\sum_{\sigma} P_{\sigma} W(\sigma \rightarrow \nu) = \sum_{\sigma} P_{\nu} W(\nu \rightarrow \sigma). \quad (\text{C.8})$$

Due to Equation (C.6) the right hand side of this equality reduces to P_{ν} , while on the left hand side the sum runs over all configurations σ , which prevents the implementation of an effective algorithm. Therefore, this equation is replaced by the so-called detailed balance [131, 133]

$$P_{\sigma} W(\sigma \rightarrow \nu) = P_{\nu} W(\nu \rightarrow \sigma), \quad (\text{C.9})$$

which is a sufficient, but not necessary condition for Equation (C.8). This means, that rates $W(\nu \rightarrow \sigma)$, which fulfill this condition automatically satisfy the stationary master Equation (C.8). Since we want to generate probabilities according to the Boltzmann rates (C.3), we get

$$\frac{W(\nu \rightarrow \sigma)}{W(\sigma \rightarrow \nu)} = \frac{P_{\sigma}}{P_{\nu}} = e^{-\beta(E_{\sigma} - E_{\nu})}. \quad (\text{C.10})$$

This condition of detailed balance does not uniquely define the rates $W(\nu \rightarrow \sigma)$ so far. A common choice to fix this is the Metropolis algorithm [131, 134], which is defined by

$$\begin{aligned} W(\nu \rightarrow \sigma) &= 1 \quad \text{for} \quad P_\sigma \geq P_\nu \quad (E_\sigma \leq E_\nu) \\ W(\nu \rightarrow \sigma) &= \frac{P_\sigma}{P_\nu} \quad \text{for} \quad P_\sigma < P_\nu \quad (E_\sigma > E_\nu) \end{aligned} \quad (\text{C.11})$$

and fulfills the detailed balance (C.10). The dynamical process starts in some configuration ν , on which some change is proposed at random, producing the configuration σ . If this change lowers the energy ($E_\sigma \leq E_\nu$) it is always accepted with probability $W(\nu \rightarrow \sigma) = 1$ and applied to the configuration. However, when the energy increases ($E_\sigma > E_\nu$) due to the proposed change, it is accepted only with probability $W(\nu \rightarrow \sigma) = P_\sigma/P_\nu \leq 1$. In the limit of many steps this process leads to configurations σ with small energies E_σ and high Boltzmann weights P_σ . Therefore, this process produces mainly configurations with large contributions to the average $\langle A \rangle$ of a physical quantity given by Equation (C.2) and only rarely ones with a small contribution.

C.2 Quantum Monte-Carlo algorithm

The principle of classical Monte-Carlo algorithm can also be transferred to quantum systems, where the Boltzmann weight $e^{-\beta \hat{H}}$ now becomes an operator. Therefore, we need to redefine the criterion for the production of relevant configurations. In order to do so, the exponential in the partition function

$$Z = \text{Tr } e^{-\beta \hat{H}} = \text{Tr} \left(e^{-\Delta\tau \hat{H}} e^{-\Delta\tau \hat{H}} \dots e^{-\Delta\tau \hat{H}} \right) \quad (\text{C.12})$$

can be decomposed in L_τ Trotter slices of equal width $\Delta\tau = \beta/L_\tau$ [131]. Moreover, the full Hamiltonian $\hat{H} = \hat{H}_1 + \hat{H}_2$ is decomposed in two summands, which is specific for the model under consideration. For the Bose-Hubbard model (2.43) introduced in Chapter 2 the two parts are given by

$$\begin{aligned} \hat{H}_1 &= \sum_{i \text{ odd}} \left((\epsilon_i - \mu) \hat{n}_i + \frac{U_i}{2} \hat{n}_i (\hat{n}_i - 1) - \frac{1}{2} \sum_{j \text{ n.n.}} J_{ij} (\hat{a}_i^\dagger \hat{a}_j + \hat{a}_j^\dagger \hat{a}_i) \right) \text{ and} \\ \hat{H}_2 &= \sum_{i \text{ even}} \left((\epsilon_i - \mu) \hat{n}_i + \frac{U_i}{2} \hat{n}_i (\hat{n}_i - 1) - \frac{1}{2} \sum_{j \text{ n.n.}} J_{ij} (\hat{a}_i^\dagger \hat{a}_j + \hat{a}_j^\dagger \hat{a}_i) \right), \end{aligned} \quad (\text{C.13})$$

where the sum runs over all odd (even) sites i in \hat{H}_1 (\hat{H}_2). With the help of the Baker-Hausdorff identity the exponential in the partition function can be rewritten as

$$e^{-\Delta\tau \hat{H}} \approx e^{-\Delta\tau \hat{H}_1} e^{-\Delta\tau \hat{H}_2} + O(\Delta\tau^2), \quad (\text{C.14})$$

where contributions on the order of $\Delta\tau^2$ are neglected. This equation is called the Trotter-Suzuki approximation [131, 135]. Since the trace is invariant of the chosen basis, we may

use the particle number basis $|\mathbf{n}\rangle = |n_1, n_2, \dots, n_M\rangle$, where M is the number of sites. Using the decomposition of the Hamiltonian (C.13) and the Trotter-Suzuki Equation (C.14) the partition function, finally takes the form

$$Z = \sum_{\{\mathbf{n}\}} \langle \mathbf{n}^1 | e^{-\Delta\tau\hat{H}_2} | \mathbf{n}^{2L_\tau} \rangle \langle \mathbf{n}^{2L_\tau} | e^{-\Delta\tau\hat{H}_1} | \mathbf{n}^{2L_\tau-1} \rangle \dots \langle \mathbf{n}^3 | e^{-\Delta\tau\hat{H}_2} | \mathbf{n}^2 \rangle \langle \mathbf{n}^2 | e^{-\Delta\tau\hat{H}_1} | \mathbf{n}^1 \rangle, \quad (\text{C.15})$$

where between each pair of the exponential the identity $\mathbb{1} = \sum_{\mathbf{n}} |\mathbf{n}\rangle\langle\mathbf{n}|$ was inserted and the sum runs over all possible configurations of $|\mathbf{n}\rangle$. The partition function is decomposed into a row of individual expectation values of the operators $e^{-\Delta\tau\hat{H}_s}$ with $s = 1, 2$, which have the same form as the time evolution operator $e^{-it\hat{H}_s}$. Therefore, the width of a Trotter slice $\Delta\tau = it$ can be associated with imaginary time. This leads to an intuitive picture of Equation (C.15): Starting in state $|\mathbf{n}^1\rangle$, which is the state at the first Trotter slice, the operator $e^{-\Delta\tau\hat{H}_1}$ evolves the system in imaginary time and ends in state $|\mathbf{n}^2\rangle$. Afterwards $e^{-\Delta\tau\hat{H}_2}$ evolves $|\mathbf{n}^2\rangle$ in imaginary time reaching state $|\mathbf{n}^3\rangle$. Now, after the action of $e^{-\Delta\tau\hat{H}_1}$ and $e^{-\Delta\tau\hat{H}_2}$ the system has evolved the first Trotter slice $\Delta\tau$. This process goes on until after L_τ steps the final Trotter slice $|\mathbf{n}^{2L_\tau}\rangle$ is reached. Therefore, the partition function can be written as a path integral over all allowed configurations $\{\mathbf{n}\}$ as they evolve during L_τ imaginary time steps. The index $l = 1, \dots, 2L_\tau$ in the particle number state $|\mathbf{n}^l\rangle$ represents the corresponding Trotter slice in imaginary time.

The concept of world lines [131] here serves as an intuitive geometric interpretation, which is illustrated in Figure C.1 for a system with 8 sites (along the x -axis) and 6 Trotter slices (along the y -axis). Please note that Equation (C.15) intrinsically demands periodic boundary conditions in imaginary time for the world lines via $\langle \mathbf{n}^1 | e^{-\Delta\tau\hat{H}_2} | \mathbf{n}^{2L_\tau} \rangle$, which means that the first and the last Trotter slices are identical. Periodic boundary conditions in position space are extrinsically introduced in many models as also in the Bose-Hubbard model, which connects the first and the last lattice site with each other. During the first step in imaginary time the operator $e^{-\Delta\tau\hat{H}_1}$ acts, which due to the definition of \hat{H}_1 connects site 1 with 2, 3 with 4, ... In Figure C.1 connected sites are emphasized by gray plaquettes between them. Operator $e^{-\Delta\tau\hat{H}_2}$ connects site 2 with 3, 4 with 5, ... leading to a checker board pattern in Figure C.1. Since only sites connected by gray plaquettes interact via the Hamiltonian (C.13), the jumps of world lines are restricted to the gray areas, as for example the blue world line in Figure C.1.

In Equation (C.15) the sum runs over all allowed world lines. Just as in the classical algorithm the task is to find configurations, which have a large contribution to the average value $\langle A \rangle$ in a way that detailed balance (C.10) is fulfilled. Therefore, starting with some allowed world line, as for example the black one in Figure C.1, one deformation is proposed leading to a new one, shown with dashed lines. For the Bose-Hubbard Hamiltonian (2.43) the affected matrix elements in the partition function (C.15), which change under this deformation, are those who are connected to the light gray plaquettes in the Figure C.1. The product Π_i of these affected matrix elements before and Π_f after the deformation are computed. In order to satisfy detailed balance (C.10) the move is accepted if this ratio Π_f/Π_i is larger than a random number drawn from a uniform distribution between zero and one and is rejected otherwise [131]. Analogously to the classical algorithm this

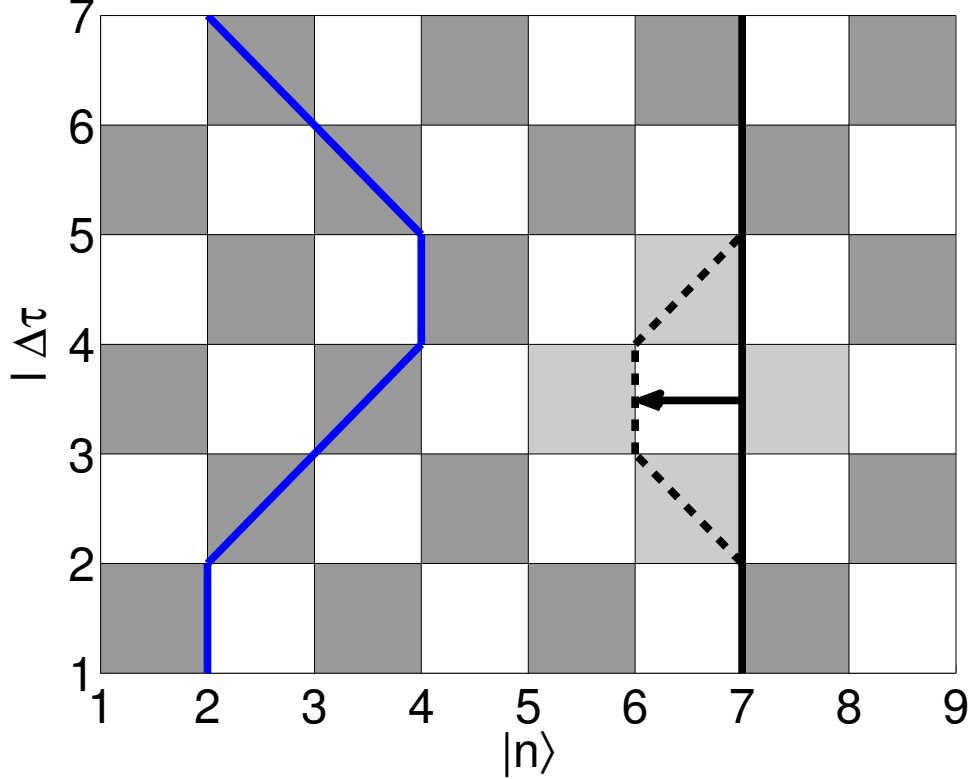


Figure C.1: Possible world line configurations in imaginary time $l\Delta\tau$ for six Trotter slices and eight sites. The arrow represents one possible deformation of the world line.

procedure mainly generates configurations with hight weights in the average value $\langle A \rangle$ and only occasionally ones with small weights.

Conclusion

The Monte Carlo algorithm in both, the classical and the quantum version is a powerful tool that can be used in various fields of physics [126–129]. Its biggest advantage is that it poses no restrictions on the system parameters, as the algorithm can be applied in the whole parameter space of the considered model. Finite size effects, which are present in every numerical simulation, are treated with finite size techniques, as for example discussed in Section (4.1), which allows for a systematic and accurate description of the transition from a finite to the limit of an infinite system. In the quantum Monte Carlo algorithm the Trotter-Suzuki approximation (C.14) is introduced, where contributions to the exponential $e^{-\Delta\tau\hat{H}}$ on the order of $\Delta\tau^2$ are neglected. Moreover, there exist sophisticated methods, which operate in continuous imaginary time and hence can eliminate this discretization error [83–87]. Therefore, advanced quantum Monte Carlo algorithms together with the systematic description of finite size effects are a powerful technique and are also widely used in connection with the Bose-Hubbard model [20, 28–36].

Bibliography

- [1] M. P. A. Fisher, P. B. Weichman, G. Grinstein, and D. S. Fisher, *Boson localization and the superfluid-insulator transition*, Phys. Rev. B **40** (1989) 546
- [2] A. E. Niederle and H. Rieger, *Superfluid clusters, percolation and phase transitions in the disordered, two dimensional Bose-Hubbard model*, New. J. Physics **15** (2013) 075029
- [3] L. Fallani, J. E. Ley, V. Guarrera, C. Fort, and M. Inguscio, *Ultracold Atoms in a Disordered Crystal of Light: Towards a Bose Glass*, Phys. Rev. Lett. **98** (2007) 130404
- [4] A. E. Niederle and H. Rieger, *Bosons in a two-dimensional bichromatic quasiperiodic potential: Analysis of the disorder in the Bose-Hubbard parameters and phase diagrams*, Phys. Rev. A **91** (2015) 043632
- [5] S Fernández-Vidal, G. De Chiara, J Larson, and G. Morigi, *Quantum ground state of self-organized atomic crystals in optical resonators*, Phys. Rev. A **81** (2010) 043407
- [6] H. Habibian, A. Winter, S. Paganelli, H. Rieger, and G. Morigi, *Quantum phases of incommensurate optical lattices due to cavity backaction*, Phys. Rev. A **88** (2013) 043618
- [7] R. Landig, L. Hruby, N. Dogra, M. Landini, R. Mottl, T. Donner, and T. Esslinger, *Quantum phases emerging from competing short- and long-range interactions in an optical lattice*, arxiv:1511.00007 (2015)
- [8] K. Baumann, C. Guerlin, F. Brennecke, and T. Esslinger, *The Dicke Quantum Phase Transition with a Superfluid Gas in an Optical Cavity*, Nature **464** (2010) 1301
- [9] A. E. Niederle, H. Rieger, and G. Morigi, *Quasi-periodic structures due to cavity backaction*,
- [10] D. Jaksch, C. Bruder, J. I. Cirac, C. W. Gardiner, and P. Zoller, *Cold Bosonic Atoms in Optical Lattices*, Phys. Rev. Lett. **81** (1998) 3108
- [11] P. B. Blakie and C. W. Clark, *Wannier states and Bose-Hubbard parameters for 2D optical lattices*, Journal of Physics B **37** (2004) 1391
- [12] I. Bloch, *Ultracold quantum gases in optical lattices*, Nature Physics **1** (2005) 23
- [13] D. Jaksch and P. Zoller, *The cold atom Hubbard toolbox*, Annals of Physics **315**(1) (2005)
- [14] D. Schrader, I. Dotsenko, M. Khudaverdyan, Y. Miroshnychenko, A. Rauschenbeutel, and D. Meschede, *Neutral Atom Quantum Register*, Phys. Rev. Lett. **93** (2004) 150501

- [15] I. Bloch, J. Dalibard, and W. Zwerger, *Many-body physics with ultracold gases*, Rev. Mod. Phys. **80** (2008)
- [16] R. Blatt and D. J. Wineland, *Entangled states of trapped atomic ions*, Nature **453** (2008) 1008–1014
- [17] W. S. Bakr, J. I. Gillen, A. Peng, S. Fölling, and M. Greiner, *A quantum gas microscope for detecting single atoms in a Hubbard-regime optical lattice*, Nature **462** (2009) 74–77
- [18] E. Urban, T. A. Johnson, T. Henage, L. Isenhower, D. D. Yavuz, T. G. Walker, and M. Saffman, *Observation of Rydberg blockade between two atoms*, Nature Physics **5** (2009) 110–114
- [19] V. Gurarie, L. Pollet, N. V. Prokof'ev, B. V. Svistunov, and M. Troyer, *Phase diagram of the disordered Bose-Hubbard model*, Phys. Rev. B **80** (2009) 214519
- [20] L. Pollet, N. V. Prokof'ev, B. V. Svistunov, and M. Troyer, *Absence of a Direct Superfluid to Mott Insulator Transition in Disordered Bose Systems*, Phys. Rev. Lett. **103** (2009) 140402
- [21] M. Greiner, O. Mandel, T. Esslinger, T. W. Hänsch, and I. Bloch, *Quantum phase transition from a superfluid to a Mott insulator in a gas of ultracold atoms*, Nature **415** (2002) 39
- [22] L. Pitaevskii and S. Stringari, *Bose-Einstein Condensation*, Oxford University Press, Oxford, 2003
- [23] T. Stöferle, H. Moritz, C. Schori, M. Köhl, and T. Esslinger, *Transition from a Strongly Interacting 1D Superfluid to a Mott Insulator*, PRL **92** (2004) 130403
- [24] P. T. Ernst, S. Götze, J. S. Krauser, K. Pyka, D. S. Lühmann, D. Pfannkuche, and K. Sengstock, *Probing superfluids in optical lattices by momentum-resolved Bragg spectroscopy*, Nature Physics **6** (2010)
- [25] D. Delande and J. Zakrzewski, *Compression as a Tool to Detect Bose Glass in a Cold Atomic Gas*, Phys. Rev. Lett. **102** (2009) 085301
- [26] J. E. Lye, L. Fallani, M. Modugno, D. S. Wiersma, C. Fort, and M. Inguscio, *Bose-Einstein Condensate in a Random Potential*, Phys. Rev. Lett. **95** (2005) 070401
- [27] M. White, M. Pasienski, D. McKay, S. Q. Zhou, D. Ceperley, and B. DeMarco, *Strongly Interacting Bosons in a Disordered Optical Lattice*, Phys. Rev. Lett. **102** (2009) 055301
- [28] W. Krauth, N. Trivedi, and D. Ceperley, *Superfluid-Insulator Transition in Disordered Boson System*, Phys. Rev. Lett. **67** (1991) 2307
- [29] J. Kisker and H. Rieger, *Bose-glass and Mott-insulator phase in the disordered boson Hubbard model*, Phys. Rev. B **55** (1997) R11981
- [30] J. Kisker and H. Rieger, *The two-dimensional disordered Boson Hubbard model: Evidence for a direct Mott insulator-to-superfluid transition and localization in the Bose glass phase*, Physica A **246** (1997) 348
- [31] N. Kawashima and K. Harada, *Recent Developments of World-Line Monte Carlo Methods*, Journal of the Physical Society of Japan **73**(6) (2004) 1379–1414

- [32] N. Prokof'ev and B. Svistunov, *Superfluid-Insulator Transition in Commensurate Disordered Bosonic Systems: Large-Scale Worm Algorithm Simulations*, Phys. Rev. Lett. **92** (2004) 015703–1
- [33] J.-W. Lee, M.-C. Cha, and D. Kim, *Phase Diagram of a Disordered Boson Hubbard Model in Two Dimensions*, Phys. Rev. Lett. **87** (2001) 247006
- [34] B. Capogrosso-Sansone, S. G. Söyler, N. Prokof'ev, and B. Svistunov, *Monte Carlo study of the two-dimensional Bose-Hubbard model*, Phys. Rev. A **77** (2008) 015602
- [35] S. G. Söyler, M. Kiselev, N. V. Prokof'ev, and B. V. Svistunov, *Phase Diagram of the Commensurate Two-Dimensional Disordered Bose-Hubbard Model*, Phys. Rev. Lett. **107** (2011) 185301
- [36] F. Lin, E. S. Sørensen, and D. M. Ceperley, *Superfluid-insulator transition in the disordered two-dimensional Bose-Hubbard model*, Phys. Rev. B **84** (2011) 094507
- [37] G. Roux, T. Barthel, I. P. McCulloch, C. Kollath, U. Schollwöck, and T. Giamarchi, *Quasiperiodic Bose-Hubbard model and localization in one-dimensional cold atomic gases*, Phys. Rev. A **78** (2008) 023628
- [38] X. Deng, R. Citro, A. Minguzzi, and E. Orignac, *Phase diagram and momentum distribution of an interacting Bose gas in a bichromatic lattice*, Phys. Rev. A **78** (2008) 013625
- [39] X. Deng, R. Citro, E. Orignac, and A. Minguzzi, *Superfluidity and Anderson localisation for a weakly interacting Bose gas in a quasiperiodic potential*, Eur. Phys. J. B **68** (2009) 435
- [40] J. Carrasquilla, F. Becca, A. Trombettoni, and M. Fabrizio, *Characterization of the Bose-glass phase in low-dimensional lattices*, Phys. Rev. B **81** (2010) 195129
- [41] S. Rapsch, U. Schollwöck, and W. Zwerger, *Density matrix renormalization group for disordered bosons in one dimension*, Europhys. Lett. **46** (1999) 559
- [42] K. Sheshadri, H. R. Krishnamurthy, R. Pandit, and T. V. Ramakrishnan, *Superfluid and insulating phases in an interacting-Boson model: Mean-field theory and the RPA*, Europhys. Lett. **22** (1993) 257
- [43] P. Buonsante, F. Massel, V. Penna, and A. Vezzani, *Gutzwiller approach to the Bose-Hubbard model with random local impurities*, Phys. Rev. A **79** (2009) 013623
- [44] P. Buonsante, V. Penna, A. Vezzani, and P. B. Blakie, *Mean-field phase diagram of cold lattice bosons in disordered potentials*, Phys. Rev. A **76** (2007) 011602
- [45] P. Buonsante and A. Vezzani, *Phase diagram for ultracold bosons in optical lattices and superlattices*, Phys. Rev. A **70** (2004) 033608
- [46] U. Bissbort and W. Hofstetter, *Stochastic mean-field theory for the disordered Bose-Hubbard model*, Europhys. Lett. **86** (2009) 50007
- [47] U. Bissbort, R. Thomale, and W. Hofstetter, *Stochastic mean-field theory: Method and application to the disordered Bose-Hubbard model at finite temperature and speckle disorder*, Phys. Rev. A **81** (2010) 063643
- [48] D. van Oosten, P. van der Straten, and H. T. C. Stoof, *Quantum phases in an optical lattice*, Phys. Rev. A **63** (2001) 053601

- [49] J. K. Freericks and H. Monien, *Strong-coupling expansion for the pure and disordered Bose-Hubbard model*, Phys. Rev. B **53** (1996) 2691
- [50] P. Sengupta and S. Haas, *Quantum Glass Phases in the Disordered Bose-Hubbard Model*, Phys. Rev. Lett. **99** (2007) 050403
- [51] K. G. Balabanyan, N. Prokof'ev, and B. Svistunov, *Superfluid-Insulator Transition in a Commensurate One-Dimensional Bosonic System with Off-Diagonal Disorder*, Phys. Rev. Lett. **95** (2005) 055701
- [52] H. Gimperlein, S. Wessel, J. Schmiedmayer, and L. Santos, *Ultracold Atoms in Optical Lattices with Random On-Site Interaction*, Phys. Rev. Lett. **95** (2005) 170401
- [53] S. Wildermuth, S. Hofferberth, I. Lesanovsky, E. Haller, L. M. Andersson, S. Groth, I. Bar-Joseph, P. Krüger, and J. Schmiedmayer, *Microscopic magnetic-field imaging*, Nature **435** (2005) 440
- [54] H. Gimperlein, S. Wessel, J. Schmiedmayer, and L. Santos, *Random on-site interactions versus random potential in ultra cold atoms in optical lattices*, Applied Physics B **82** (2006) 217
- [55] T Roscilde, *Bosons in one-dimensional incommensurate superlattices*, Phys. Rev. A **77** (2008) 063605
- [56] F. Schmitt, M. Hild, and R. Roth, *Phase diagram of bosons in two-color superlattices from experimental parameters*, Phys. Rev. A **80** (2009) 023621
- [57] F. Schmitt, M. Hild, and R. Roth, *Ab initio phase diagram of ultracold ^{87}Rb in a one-dimensional two-color superlattice*, J. Phys. B **43** (2010) 235301
- [58] A. Einstein, *Quantentheorie des einatomigen idealen Gases*, Sitzungsber. preuss. Akad. Wiss. **22** (1924) 261
- [59] S. N. Bose, *Plancks Gesetz und die Lichtquantenhypothese*, Z. Phys. **26** (1924) 178
- [60] M. H. Anderson, J. R. Ensher, M. R. Matthews, C. E. Wieman, and W. E. Cornell, *Observation of Bose-Einstein Condensation in a Dilute Atomic Vapor*, Science **269** (1995) 198
- [61] C. C. Bradley, C. A. Sackett, J. J. Tollett, and R. G. Hulet, *Evidence of Bose-Einstein Condensation in an Atomic Gas with Attractive Interactions*, Phys. Rev. Lett. **75** (1995) 1687
- [62] K. B. Davis, M. O. Mewes, M. R. Andrews, N. J. van Druten, D. S. Durfee, D. M. Kurn, and W. Ketterle, *Bose-Einstein Condensation in a Gas of Sodium Atoms*, Phys. Rev. Lett. **75** (1995) 3969
- [63] A. Einstein, *Quantentheorie des einatomigen idealen Gases. Zweite Abhandlung*, Sitzungsber. preuss. Akad. Wiss. **1** (1925) 3
- [64] C. J. Pethick and H. Smith, *Bose-Einstein Condensation in Dilute Gases*, Cambridge University Press, Cambridge, 2008
- [65] M. Ueda, *Fundamentals and new Frontiers of Bose-Einstein Condensation*, World Scientific, Singapore, 2010
- [66] S. Chu, *Nobel Lecture: The manipulation of neutral particles*, Rev. Mod. Phys. **70** (1998) 685

- [67] C. N. Cohen-Tannoudji, *Nobel Lecture: Manipulating atoms with photons*, Rev. Mod. Phys. **70** (1998) 707
- [68] W. D. Phillips, *Nobel Lecture: Laser cooling and trapping of neutral atoms*, Rev. Mod. Phys. **70** (1998) 721
- [69] N. Masuhara, J. M. Doyle, J. C. Sandberg, D. Kleppner, T. J. Greytak, H. F. Hess, and G. P. Kochanski, *Evaporative Cooling of Spin-Polarized Atomic Hydrogen*, Phys. Rev. Lett. **61** (1988) 935
- [70] W. Ketterle and N. J. van Druten, *Bose-Einstein condensation of a finite number of particles trapped in one or three dimensions*, Phys. Rev. A **54** (1996) 656
- [71] W. Ketterle, *Nobel lecture: When atoms behave as waves: Bose-Einstein condensateion and the atom laser*, Rev. Mod. Phys. **74** (2002) 1131
- [72] R. Grimm, M. Weidmüller, and Y. Ovchinnikov, *Optical Dipole Traps for Neutral Atoms*, Adv. At. Mol. Opt. Phys. **42** (2000) 95
- [73] M. R. Andrews, C. G. Townsend, H.-J. Miesner, D. S. Durfee, D. M. Kurn, and W. Ketterle, *Observation of Interference Between Two Bose Condensates*, Sience **273** (1997) 367–641
- [74] J. Stenger, S. Inouye, A. P. Chikkatur, D. M. Stamper-Kurn, D. E. Pritchard, and W. Ketterle, *Bragg Spectroscopy of a Bose-Einstein Condensate*, Phys. Rev. Lett. **82(23)** (1999)
- [75] T Roscilde, *Probing correlated phases of bosons in optical lattices via trap squeezing*, New J. of Phys. **11** (2009) 023019
- [76] G. Czycholl, *Theoretische Festkörperphysik*, Springer, Berlin Heidelberg, 2008
- [77] T. Bergman, M. G. Moore, and M. Olshanii, *Atom-Atom Scattering under Cylindrical Harmonic Confinement: Numerical and Analytic Studies of the Confinement Induced Resonance*, Phys. Rev. Lett. **91** (2003) 163201
- [78] Y. Ohashi, M. Kitaura, and H. Matsumoto, *Itinerant-localized dual character of a strongly correlated superfluid Bose gas in an optical lattice*, Phys. Rev. A **73** (2006) 033617
- [79] P. Krüger, Z. Hadzibabic, and J. Dalibard, *Critical Point of an Interacting Two-Dimensional Atomic Bose Gas*, PRL **99** (2007) 040402
- [80] J. M. Zhang and R. X. Dong, *Exact diagonalization: the Bose-Hubbard model as an example*, Eur. J. Phys. **31** (2010) 591
- [81] B. Capogrosso-Sansone, N. V. Prokof'ev, and B. V. Svistunov, *Phase diagram and thermodynamis of the three-dimensional Boson-Hubbard model*, Phys. Rev. B **75** (2007) 134302
- [82] P. Hitchcock and E. S. Sørensen, *Bose-glass to superfluid transition in the three-dimensional Bose-Hubbard model*, Phys. Rev. B **73** (2006) 174523
- [83] B. B. Beard and U.-J. Wiese, *Simulations of Discrete Quantum Systems in Continuous Euclidean Time*, Phys. Rev. Lett. **77(25)** (1996) 5130
- [84] N. V. Prokof'ev, B. V. Svistunov, and I. S. Tupitsyn, *Worm algorithm in quantum Monte Carlo simulations*, Physics Letters A **238** (1998) 253

- [85] H. Rieger and N. Kawashima, *Application of a continuous time cluster algorithm to the two-dimensional random quantum Ising ferromagnet*, Eur. Phys. J. B **9** (1998) 233–236
- [86] A. Winter, H. Rieger, M. Vojta, and R. Bulla, *The Quantum Phase Transition in the Sub-Ohmic Spin-Boson Model: Quantum Monte-Carlo Study with a Continuous Imaginary Time Cluster Algorithm*, PRL **102** (2009) 030601
- [87] A. Winter and H. Rieger, *Quantum phase transition and correlations in the multi-spin-boson model*, Phys. Rev. B **90** (2014) 224401
- [88] S. R. White, *Density Matrix Formulation for Quantum Renormalization Groups*, PRL **69** (1992) 19
- [89] U. Schollwöck, *The density-matrix renormalization group*, Rev. Mod. Phys. **77** (2005) 259
- [90] C.-H. Lin, R. Sensarma, K. Sengupta, and S. Das Sarma, *Quantum dynamics of disordered bosons in an optical lattice*, Phys. Rev. B **86** (2012) 214207
- [91] P. Buonsante and V. Penna, *Some remarks on the coherent-state variational approach to nonlinear boson models*, J. Phys. A **41** (2008) 17530
- [92] D. Jaksch, V. Venturi, J. I. Cirac, C. J. Williams, and P. Zoller, *Creation of a Molecular Condensate by Dynamically Melting a Mott Insulator*, PRL **89** (2002) 040402
- [93] J. Stasińska, M. Łkacki, O. Dutta, J. Zakrzewski, and M. Lewenstein, *Bose-Hubbard model with random impurities: Multiband and nonlinear hopping effects*, Phys. Rev. A **90** (2014) 063634
- [94] D. Stauffer and A. Aharony, *Introduction To Percolation Theory*, CRC Press, 1994
- [95] W. S. Bakr, A. Peng, M. E. Tai, R. Ma, J. Simon, J. I. Gillen, S. Fölling, L. Pollet, and M. Greiner, *Probing the Superfluid-to-Mott Insulator Transition at the Single-Atome Level*, Science **329** (2010) 547
- [96] J. F. Sherson, C. Weitenberg, M. Endres, M. Cheneau, I. Bloch, and S. Kuhr, *Single-atom-resolved fluorescence imaging of an atomic Mott insulator*, Nature **467** (2010) 68
- [97] J. Hoshen and R. Kopelman, *Percolation and cluster distribution I. Cluster multiple labeling technique and critical concentration algorithm*, Phys. Rev. B **14(8)** (1976) 3438–3445
- [98] R. Roth and K. Burnett, *Phase Diagram of bosonic atoms in two-color superlattices*, Phys. Rev. A **68** (2003) 023604
- [99] E. L. Pollock and D. M. Ceperley, *Path-integral computation of superfluid densities*, Phys. Rev. B **36** (1987) 8343
- [100] D. S. Fisher, *Critical behavior of random transverse-field Ising spin chains*, Phys. Rev. B **51** (1995) 6411
- [101] D. S. Fisher, *Phase transitions and singularities in random quantum systems*, Physica A **263** (1999) 222

- [102] C. Pich, A. P. Young, H. Rieger, and N. Kawashima, *Critical behavior and Griffiths-McCoy singularities in the two-dimensional random quantum Ising ferromagnet*, Phys. Rev. Lett. **81** (1998) 5916
- [103] I. A. Kovacs and F. Igloi, *Infinite disorder scaling of random quantum magnets in three and higher dimensions*, Phys. Rev. B **83** (2011) 174207
- [104] T. Vojta, *Rare region effects at classical, quantum, and non-equilibrium phase transitions*, J. Phys. A **39** (2006) R143
- [105] V. Gurarie, L. Pollet, N. V. Prokof'ev, B. V. Svistunov, and M. Troyer, *Phase Diagram of the disordered Bose-Hubbard model*, Phys. Rev. B **80** (2009) 214519
- [106] G. M. Falco, T. Nattermann, and V. L. Pokrovsky, *Weakly interacting Bose gas in a random environment*, Phys. Rev. B **80** (2009) 104515
- [107] P. Pisarski, R. M. Jones, and R. J. Gooding, *Application of multisite mean-field theory to the disordered Bose-Hubbard model*, Phys. Rev. A **83** (2011) 053608
- [108] H. Feshbach, *Unified Theory of Nuclear Reactions*, Annals of Physics **5** (1958) 357–390
- [109] V. Guarnera, L. Fallani, J. E. Lye, C. Fort, and M. Inguscio, *Inhomogeneous broadening of a Mott insulator spectrum*, New J. of Phys. **9** (2007) 107
- [110] C. Zhang, A. Safavi-Naini, and B. Capogrosso-Sansone, *Equilibrium phases of two-dimensional bosons in quasi-periodic lattices*, Phys. Rev. A **91** (2015) 031604
- [111] E. Frey and L. Balents, *Critical behaviour of the supersolid transition in Bose-Hubbard models*, Phys. Rev. B **55(2)** (1997) 10502
- [112] G. G. Batrouni, R. T. Scalettar, G. T. Zimanyi, and A. P. Kampf, *Supersolids in the Bose-Hubbard Hamiltonian*, PRL **74(13)** (1995) 2527
- [113] G. G. Batrouni and R. T. Scalettar, *Phase Separation in Supersolids*, PRL **84(7)** (2000) 1599
- [114] Private communication with Tobias Donner and Manuele Landini from ETH Zürich quantum optics group
- [115] E. Schrödinger, *Der stetige Übergang von der Mikro- zur Makromechanik*, Naturwissenschaften **14** (1926) 664
- [116] R. J. Glauber, *The Quantum Theory of Optical Coherence*, Phys. Rev. **130** (1963) 2529
- [117] R. J. Glauber, *Coherent and Incoherent States of the Radiation Field*, Phys. Rev. **131** (1963) 2766
- [118] R. J. Glauber, *Photon Correlations*, Phys. Rev. Lett. **10** (1963) 84
- [119] E. C. G. Sudarshan, *Equivalence of Semiclassical and Quantum Mechanical Descriptions of Statistical Light Beams*, Phys. Rev. Lett. **10** (1963) 277
- [120] A. M. Perelomov, *Coherent States for arbitrary Lie Groups*, Com. Math. Phys. **26** (1972) 222
- [121] R. Gilmore, *Geometry of symmetrized states*, Ann. Phys. (N.Y.) **74** (1972) 391
- [122] R. Gilmore, *Baker-Campbell-Hausdorff formulas*, J. Math. Phys. **15** (1974) 2090

- [123] W.-M. Zhang, D. H. Feng, and R. Gilmore, *Coherent states: Theory and some applications*, Rev. Mod. Phys. **62** (1990) 867
- [124] R. Gilmore, C. M. Bowden, and L. M. Narducci, *Classical-quantum correspondence for multilevel systems*, Phys. Rev. A **12** (1975) 1019
- [125] N. N. Bogoliubov, J. Phys. USSR **11** (1947) 23
- [126] P. J. Reynolds, R. N. Barnett, B. L. Hammond, and W. A. Lester, *Molecular Physics and Chemistry Applications of Quantum Monte Carlo*, Journal of Statistical Physics **43** (1986) 1017–1026
- [127] W. von der Linden, *A Quantum Monte Carlo approach to many-body physics*, Physics Reports **220** (1992) 53–162
- [128] L. Mitas, *Electronic structure by quantum Monte Carlo: atoms, molecules and solids*, Computer Physics Communication **96** (1996) 107–117
- [129] M. B. Giles, F. Y. Kuo, I. H. Sloan, and B. J. Waterhouse, *Quasi-Monte Carlo for finance application*, ANZIAM J **50** (2008) C308–C323
- [130] N. Metropolis, *The Beginning of the Monte Carlo Method*, Los Alamos Science (1987) 125
- [131] M. Le Bellac, F. Mortessagne, and G. G. Batrouni, *Equilibrium and Non-Equilibrium Statistical Thermodynamics*, Cambridge University Press, 2006
- [132] A. A. Markov, *Extension of the limit theorems of probability theory to a sum of variables connected in a chain*, in R. Howard, editor, *Dynamic Probabilistic Systems*, pages 552–577. John Wiley and Sons, 1971
- [133] J. C. Maxwell, *On the Dynamical Theory of Gases*, Phil. Trans. R. Soc. Lond. **157** (1867) 49–88
- [134] N. Metropolis, A. W. Rosenbluth, M. W. Rosenbluth, A. H. Teller, and E. Teller, *Equation of State Calculations by Fast Computing Machines*, J. Chem. Phys. **21(6)** (1953) 1087
- [135] H. Trotter, *Discrete approximations of continuous Markov processes*, in *Proceedings of the IBM Scientific Computing Symposium on Large Scale Problems*, pages 37–42, 1963

Figure Credit

Figures 2.2 and 2.3 are taken from reference [21].

Figures 3.1 to 3.6 and Figures 4.2 to 4.5 have already been published in reference [2], by courtesy of IOP.

Figure 2.7, Figures 5.1 to 5.3 as well as Figures 6.1 to 6.9 and Figure 6.11 have already been published in reference [4], by courtesy of APS.

Curriculum Vitae

Personal data

Name Astrid Elisa Niederle
Date of birth 27.04.1983

Education

11/2011	Member of the organizing committee of the 15. Deutschen Physikerrinnentagung (DPT) at the Saarland University
06/2009–05/2012	Scholarship of the “Exzellenzprogramm für Wissenschaftlerinnen” of the Saarland University
since 06/2008	PhD student in the group of Prof. Dr. H. Rieger
04/2008	Diploma in physics
01/2007–12/2007	Diploma thesis “Dissipative Qubits - Dynamik eines BEC mit Zerfall” in the group of apl. Prof. Dr. H. J. Korsch
11/2005	Intermediate Diploma in Physics
10/2002–04/2008	Studies in Physics with minor subjects Mechanical Engineering, Mathematics and Advanced Theoretical Physics at TU Kaiserslautern
06/2002	Abitur with advanced courses in Physics and Mathematics
1993–2002	Fürst-Johann-Ludwig-Schule, Hadamar

Publications

Articles in refereed journals

- [A6] A. E. Niederle, H. Rieger and G. Morigi, *Quasi-periodic structures due to cavity backaction*, in preparation
- [A5] A. E. Niederle and H. Rieger, *Bosons in a two-dimensional bichromatic quasiperiodic potential: Analysis of the disorder in the Bose-Hubbard parameters and phase diagrams*, Phys. Rev. A **91**, 043632 (2015)
- [A4] A. E. Niederle and H. Rieger, *Superfluid clusters, percolation and phase transitions in the disordered, two-dimensional Bose-Hubbard model*, New J. Phys. **15**, 075029 (2013)
- [A3] E. M. Graefe, H. J. Korsch and A. E. Niederle, *Quantum-classical correspondence for a non-Hermitian Bose-Hubbard dimer*, Phys. Rev. A **82**, 013629 (2010)
- [A2] E. M. Graefe, U. Günther, H. J. Korsch and A. E. Niederle, *A non-Hermitian PT-symmetric Bose-Hubbard model: eigenvalue rings from unfolding higher-order exceptional points*, J. Phys. A: Math. Theor. **41** 255206 (2008)
- [A1] E. M. Graefe, H. J. Korsch and A. E. Niederle, *Mean-Field Dynamics of a Non-Hermitian Bose-Hubbard Dimer*, Phys. Rev. Lett. **101**, 150408 (2008)

Conferences

- [C12] A. E. Niederle, H. Rieger, G. Morigi, *Phase diagram of bosons in optical lattices generated due to cavity backaction*, DACH project meeting, talk (Innsbruck, Austria, 09/2015)
- [C11] A. E. Niederle, H. Rieger, *The disordered Bose-Hubbard model and percolating superfluid clusters*, XXV IUPAP International Conference on Statistical Physics (STATPHYS), poster (Seoul, South Korea, 07/2013)
- [C10] Member of the organizing committee of the 15. Deutschen Physikerinnentagung (DPT) at the Saarland University (Saarbrücken, 11/2011)
- [C9] A. E. Niederle, H. Rieger, *Local mean field in optical lattices*, New Trends in Quantum Matter With Cold Atoms and Molecules, poster (São Carlos, Brasilien, 04/2011)
- [C8] A. E. Niederle, H. Rieger, *Local mean field in optical lattices*, DPG Frühjahrstagung, poster (Dresden, 03/2011)
- [C7] A. E. Niederle, H. Rieger, *Quantum phase transitions in disordered optical lattices - a local mean-field approach*, Deutschen Physikerinnentagung der DPG (DPT), poster (München, 11/2010)
- [C6] A. E. Niederle, H. Rieger, *Local mean-field theory for quantum phase transitions in disordered Bose-Hubbard systems*, 22nd International Conference on Atomic Physics (ICAP), poster (Cairns, Australia, 07/2010)
- [C5] A. E. Niederle, H. Rieger, *Local mean-field theory for quantum phase transitions in disordered Bose-Hubbard systems*, DPG Frühjahrstagung, poster (Regensburg, 03/2010)
- [C4] A. E. Niederle, E.-M. Graefe, H. J. Korsch, *Mean-field dynamics of a non-hermitian Bose-Hubbard dimer*, DPG Frühjahrstagung, poster (Dresden, 03/2009)
- [C3] A. E. Niederle, E.-M. Graefe, H. J. Korsch, *Mean-field description of a decaying BEC*, group seminar of Prof. Dr. Andreas Buchleitner, invited talk (Freiburg, 06/2008)
- [C2] A. E. Niederle, E.-M. Graefe, H. J. Korsch, F. Trimborn, D. Witthaut *Mean-field description of a decaying BEC*, DPG Frühjahrstagung, talk (Darmstadt, 03/2008)
- [C1] A. E. Niederle, E.-M. Graefe, F. Trimborn, H. J. Korsch *Dynamik eines Zweimoden-Bose-Hubbard-Modells mit Zerfall*, DPT, talk (Osnabrück, 11/2007)

Eidesstattliche Versicherung

Hiermit versichere ich an Eides statt, dass ich die vorliegende Arbeit selbstständig und ohne Benutzung anderer als der angegebenen Hilfsmittel angefertigt habe. Die aus anderen Quellen oder indirekt übernommenen Daten und Konzepte sind unter Angabe der Quelle gekennzeichnet. Die Arbeit wurde bisher weder im In- noch im Ausland in gleicher oder ähnlicher Form in einem Verfahren zur Erlangung eines akademischen Grades vorgelegt.

Ludwigshafen, den

Astrid Elisa Niederle

Acknowledgment

Many people have accompanied my personal journey through the last years lending support and advice in various situations. To some of them I would like to dedicate the next lines.

Let me first thank my supervisor Prof. Dr. Heiko Rieger for fruitful discussions and the opportunity to graduate in his group.

I would like to thank Prof. Dr. Giovanna Morigi for inspiring conversations and the successful cooperation on the field of “cavity backaction”.

Let me express my special gratitude to the former and present members of the statistical physics group at the Saarland university. Thanks for all physical discussions and all the relaxing chats around the coffee machine.

I thank the *Gleichstellungsbüro* of the Saarland University for the scholarship of the “*Exzellenzprogramm für Wissenschaftlerinnen*”. It gave me the great opportunity for collecting personal experiences especially in many of the excellent workshops.

I would like to thank all other members of the organizing committee of the *15. Deutschen Physikerinnentagung* (DPT) at the Saarland University. I am really glad to have been part of this exciting project.

Finally, I would like to express my gratitude to my family:

To my husband Martin for his understanding, honesty and his patience,

to my sister Ulrike for our wonderful friendship,

and finally to my parents for encouraging support and always lending a sympathetic ear.

Soll Denken überhaupt einen Sinn haben, so fordert es über sich die a priori bestehende Einheit einer ewigen Wahrheit, die die Menschheit vielleicht aus sich heraus allein nicht hat, deren Spuren sie aber in sich selbst und in ihrer Welt aufzufinden vermag und zu der sie sich in der Redlichkeit ihres Denkens immerdar auf dem Wege weiß, mögen auch in dieser Welt die Antagonismen aus menschlicher Kraft allein schlechthin unaufhebbar sein.

— Prof. Dr. Wilhelm Himmerich, Eudaimonia